Low-energy electron and ion induced surface processes: Studies of novel surface species on Cu(100) and Si(111)7×7 by electron-based materials analysis techniques

by

Hui Yu

A thesis presented to the University of Waterloo
in fulfillment of the
thesis requirement for the degree of
Doctor of Philosophy
in
Physics

Waterloo, Ontario, Canada, 1998

© Hui Yu 1998

Reproduced with permission of the copyright owner. Further reproduction prohibited without permission.

National Library of Canada
Bibliothèque nationale du Canada

Acquisitions and Bibliographic Services
Acquisitions et services bibliographiques

395 Wellington Street
Ottawa ON K1A 0N4
Canada

395, rue Wellington
Ottawa ON K1A 0N4
Canada

Your file Votre référence

Our file Notre référence

The author has granted a non-exclusive licence allowing the National Library of Canada to reproduce, loan, distribute or sell copies of this thesis in microform, paper or electronic formats.

L'auteur a accordé une licence non exclusive permettant à la Bibliothèque nationale du Canada de reproduire, prêter, distribuer ou vendre des copies de cette thèse sous la forme de microfiche/film, de reproduction sur papier ou sur format électronique.

The author retains ownership of the copyright in this thesis. Neither the thesis nor substantial extracts from it may be printed or otherwise reproduced without the author's permission.

L'auteur conserve la propriété du droit d'auteur qui protège cette thèse. Ni la thèse ni des extraits substantiels de celle-ci ne doivent être imprimés ou autrement reproduits sans son autorisation.

0-612-32868-6

Canada

Reproduced with permission of the copyright owner. Further reproduction prohibited without permission.

I hereby declare that I am the sole author of this thesis.

I authorize the University of Waterloo to lend this thesis to other institutions or individuals for the purpose of scholarly research.

I further authorize the University of Waterloo to reproduce this thesis by photocopying or by other means, in total or in part, at the request of other institutions or individuals for the purpose of scholarly research.

Reproduced with permission of the copyright owner. Further reproduction prohibited without permission.

The University of Waterloo requires the signatures of all persons using or photocopying this thesis. Please sign below, and give address and date.

Reproduced with permission of the copyright owner. Further reproduction prohibited without permission.

ABSTRACT

A multi-technique portable spectrometer for electron energy loss spectroscopy (EELS) has been developed to study surface reactions and adsorption properties induced by low-energy electron and ion irradiation on two popular model surfaces in surface science: Cu(100) and Si(111)7×7. Both vibrational EELS spectra at high resolution and electronic EELS spectra over an extended energy range have been obtained. Together with other surface analysis techniques, including temperature-programmed desorption mass spectrometry, low-energy electron diffraction and Auger electron spectrometry, the present work examined some of the intriguing aspects of surface processes induced by low energy electron and ion irradiation.

The surface interactions of CO with clean, oxygen-precovered and carbon-pre-covered surfaces of Cu(100) were investigated. In particular, we observed anomalous adsorption of "stabilized" CO species on Cu(100) above room temperature, which was produced in-situ by low-energy electron irradiation of CO/Cu(100) at 120 K or by low-energy ion irradiation of Cu(100) in CO or with pre-exposure of O_2 in ethylene at room temperature. The stretching frequency of the "stabilized" CO was found to be either red- or blue- shifted from its nominal (low-temperature adsorption) position, depending on the nearby-coadsorbed species. We proposed a direct-interaction bonding model involving a "tilted" CO molecule on an atop site semi-bridge-bonded to an O or C atom in a four-fold hollow site. On a c(2×2)N/Cu(100) surface produced by low-energy ion irradiation in N_2, we demonstrated the co-existence of embedded nitrogen and surface-bonded nitrogen. Furthermore, we also studied the reactions of ethylene ions with oxygen pre-covered and nitrogen pre-covered Cu(100) surfaces. Along with various hydrocarbon species, CO and CN species were found to adsorb on these surfaces, respectively, at room temperature.

On the Si(111)7×7 surface, we studied the effects of surface contamination by ambient gas and carbon on the adsorption of oxygen and water. It was found that the presence of a high level of surface carbon could poison the 7×7 surface, reducing further adsorption by water and hydrocarbons but not by oxygen, whereby in the latter case the

Reproduced with permission of the copyright owner. Further reproduction prohibited without permission.

nature of oxygen adsorption appeared not to be sensitive to the coadsorbed species. We also investigated the formation of silicon dioxide and silicon carbide layers on Si(111)7×7 generated by both thermal deposition and ion-assisted deposition by electronic EELS and Auger electron spectroscopy. This study showed that a higher efficiency in producing surface carbon could be obtained by using ion-assisted deposition than by the thermal deposition method. However, a high concentration of carbon deposited on the surface by ion irradiation led to the formation of graphite, which in turn prevented carbon diffusion into the bulk. In both the Cu(100) and Si(111)7×7 studies, coadsorbates (contaminants) were found to play an important role on the adsorption and subsequent chemical processes of other common adsorbates. These studies further demonstrate the enormous potential of using low-energy electron or ion irradiation for surface reaction activation and the effectiveness of the electron energy loss techniques for probing these fascinating phenomena.

Reproduced with permission of the copyright owner. Further reproduction prohibited without permission.

ACKNOWLEDGEMENTS

Thanks should go to the entire staff of the Science Shops, particularly, Chris Gendron, Reg Graf, and Jacek Szubra for their dedication in providing technical support that made this work possible. I would also like to acknowledge the former coworkers in this lab, Deqing Hu, Charlie MacPherson, Lin Mei, Xiang He and Chris Mathers for their helps in the experiments and insightful discussions on the research problems. My sincere thanks also go to Professor Dan Thomas for his helpful advice and information during my studies. Finally, special thanks should go to my supervisor, Professor Tong Leung, for his patient and tireless guidance and support during my work.

Reproduced with permission of the copyright owner. Further reproduction prohibited without permission.

To my wife Qian and daughter Sandy

Reproduced with permission of the copyright owner. Further reproduction prohibited without permission.

TABLE OF CONTENTS

ABSTRACT iv

ACKNOWLEDGEMENTS vi

LIST OF TABLES xi

LIST OF FIGURES xii

Chapter 1 INTRODUCTION 1

1.1 General surface processes 1

1.1.1 Surface adsorption, coadsorption and surface reactions 1

1.1.2 Electron and ion induced surface processes 3

1.2 Surface analysis techniques 5

1.2.1 High resolution electron energy loss spectroscopy 6

1.2.2 Extended-range electron energy loss spectroscopy 7

1.2.3 Temperature programmed desorption 8

1.2.4 Low energy electron diffraction 8

1.2.5 Auger electron spectroscopy 9

1.3 Structure of this thesis 10

1.4 References 10

Chapter 2 EXPERIMENTAL DETAILS 13

2.1 Experimental setup and sample preparation 13

2.2 Irradiation by low-energy electron and ion beams 14

2.3 Electron energy loss experiments 15

2.4 Temperature programmed desorption experiments 21

2.5 LEED and AES experiments 21

2.6 References 23

Chapter 3 "ANOMALOUS" STABILIZATION OF CO ON Cu(100) AT ROOM TEMPERATURE INDUCED BY LOW-ENERGY ELECTRON AND ION IRRADIATION 24

Reproduced with permission of the copyright owner. Further reproduction prohibited without permission.

3.1 Introduction....24
3.2 Stabilization of CO/Cu(100) induced by low-energy electron irradiation 26
3.3 Ion irradiation of Cu(100) in CO at RT.... 29
3.4 Ion irradiation of Cu(100) in C_2H_4 with pre- and post-exposure of O_2 at RT.... 34
3.5 CO stabilization by C-containing species on Cu(100) at RT....39
3.6 Bonding model for the "stabilized" CO adsorption....45
3.7 Summary....49
3.8 References.... 50

Chapter 4 INTERACTIONS OF LOW-ENERGY (20-800 eV) NITROGEN IONS WITH Cu(100).... 52
4.1 Introduction....52
4.2 Results and Discussion.... 53
4.3 Summary 61
4.4 References.... 63

Chapter 5 **FORMATION OF SURFACE RADICALS ON N-PRECOVERED Cu(100) INDUCED BY LOW-ENERGY ION IRRADIATION IN ETHYLENE** 65
5.1 Introduction 65
5.2 Hydrocarbon species created on clean Cu(100)....67
5.3 Low-energy ethylene ion interactions with N-pre-covered Cu(100)....75
5.4 Summary 80
5.5 References 82

Chapter 6 HREELS STUDY OF CARBON AND AMBIENT-GAS CONTAMINATION ON Si(111)7×7.... 84
6.1 Introduction....84
6.2 Common contamination on Si(111)7×7 86
6.2.1 Carbon contamination 86

Reproduced with permission of the copyright owner. Further reproduction prohibited without permission.

6.2.2 Contamination due to ambient gas.....90
6.3 Coadsorption of water and oxygen on clean and C-pre-covered Si(111)7×7.....93
6.4 Summary 99
6.5 References.....100

Chapter 7 ELS STUDIES OF THE FORMATION OF SiO_2 AND SiC THIN FILMS ON Si(111)7×7 102
7.1 Introduction.....102
7.2 Characterization of SiO_2 film formation on Si(111)7×7..... 103
7.3 Characterization of the formation of carbonaceous thin film on Si(111)7×7..... 109
7.4 Summary.....118
7.5 References..... 120

Chapter 8 OUTLOOK.....122

Reproduced with permission of the copyright owner. Further reproduction prohibited without permission.

LIST OF TABLES

Table 5.1 Comparison of vibrational frequencies of the observed species on Cu(100) at room temperature obtained by ion irradiation in C_2H_4 at 200 eV with those obtained by molecular adsorption at 80 K and those for C_2H_4 and CH_2 groups in the gas phase..... 72

Table 5.2 Comparison of vibrational frequencies of the observed species obtained on N-precovered Cu(100) by ion irradiation in C_2H_4 at 200 eV with those for gaseous HCN, gaseous HNC, HCN/Cu(111), and HCNH/W(100)..... 78

Table 7.1 Energy positions of the plasmon features for common carbon-containing films..... 110

Reproduced with permission of the copyright owner. Further reproduction prohibited without permission.

LIST OF FIGURES

Figure 2.1 Experimental setup of low-energy ion irradiation..... 15

Figure 2.2 Schematic diagram of the electron energy loss spectrometer at the University of Waterloo.....16

Figure 2.3 Typical electron energy loss spectra for (a) a clean Cu(100) surface with (ii) and without (i) a 30 L exposure of CO at 130 K collected at 4 eV impact energy, and for (b) a clean Cu(100) surface recorded at 100 eV impact energy over an extended energy loss range illustrating the on-set of the electronic band structure..... 18

Figure 2.4 Thermal desorption profile of mass 40 (Ar^+) for Si(111)7×7 sputtered by 500 eV Ar^+ for 30 minutes at 3×10^{-5} Torr and its corresponding PID controlled temperature ramping curve.....22

Figure 3.1 Bonding modal for CO chemisorbed on a metal surface..... 25

Figure 3.2 Vibrational electron energy loss spectra for (a) 100 L of CO adsorbed on Cu(100) at 120 K, and (b) sample (a) irradiated with electrons at 100 eV and 2.7 $\mu A/mm^2$ for 10 minutes at 120 K, followed by annealing to (c) 160 K, (d) 200 K, (e) 370 K, and (f) 420 K.....27

Figure 3.3 Vibrational electron energy loss spectra for (a) Cu(100) sputtered in 1×10^{-6} Torr of CO at 200 eV and 10 nA/mm^2 for 10 minutes at 300 K, followed by annealing to (b) 370 K, (c) 400 K, and (d) 430 K.....30

Figure 3.4 Temperature programmed desorption profiles of (a) mass 28 and (b) mass 44 for Cu(100) sputtered in 1×10^{-6} Torr of CO at 200 eV and 10 nA/mm^2 for 10 minutes at 300 K..... 31

Figure 3.5 Auger electron spectra of clean Cu(100) (a) at 730 K, (b) at room temperature, (c) after sputtered in CO at 200 eV impact energy, and (d) after subsequent annealing to 530 K, and (e) CO/Cu(100) at 100 K..... 33

Reproduced with permission of the copyright owner. Further reproduction prohibited without permission.

Figure 3.6 Vibrational electron energy loss spectra for (a) Cu(100) exposed with 500 L of O_2 at 300 K, and (b) sample (a) sputtered in 1×10^{-6} Torr of ethylene at 50 eV and 10 nA/mm^2 for 10 minutes, followed by annealing to (c) 370 K, and (d) 430 K..... 35

Figure 3.7 Vibrational electron energy loss spectra for (a) Cu(100) sputtered in 1×10^{-6} Torr of ethylene at 50 eV and 10 nA/mm^2 for 10 minutes at 300 K, and (b) sample (a) exposed with 100 L of O_2, followed by annealing to (c) 370 K, and (d) 430 K..... 37

Figure 3.8 Auger electron spectra for (a) clean Cu(100), (b) after dosing 200 L oxygen at room temperature, followed by (c) sputtering in 600 L of ethylene at 50 eV, and (d) annealed to 420 K..... 38

Figure 3.9 Electron energy loss spectra for an oxygen-precovered Cu(100) surface ion-irradiated at 200 eV impact energy in (a) 2 kL, (b) 4 kL, (c) 8 kL, and (d) 16 kL of C_2H_4..... 40

Figure 3.10 Electron energy loss spectra for an oxygen-precovered Cu(100) surface ion-irradiated at 200 eV impact energy in 2 kL of C_2D_4 (a) without and with annealing to (b) 380 K, and (c) 480 K..... 42

Figure 3.11 Electron energy loss spectra for an oxygen-precovered Cu(100) surface ion-irradiated at 200 eV impact energy in 16 kL of C_2H_4 (a) without and with annealing to (b) 330 K, (c) 430 K, and (d) 530 K..... 43

Figure 3.12 Temperature programmed desorption profiles of, (a) mass 4, (b) mass 14, and (c) mass 28 for 500 L O_2 pre-deposited on Cu(100) followed by sputtering in 8 kL of C_2D_4 at 200 eV 44

Figure 3.13 Perspective (a) and side-view (b) diagrams of a proposed bonding structure for CO coadsorbed with O on Cu(100)..... 48

Figure 4.1 Temperature programmed desorption profiles of the parent ion (mass 28) of N_2 for Cu(100) ion-irradiated

Reproduced with permission of the copyright owner. Further reproduction prohibited without permission.

with 12 kL of N_2 at an impact energy of (a) 20, (b) 40, (c) 60, (d) 100, (e) 200, (f) 300, (g) 500, and (h) 800 eV 54

Figure 4.2 Vibrational electron energy loss spectra for Cu(100) ion-irradiated with 12 kL of N_2 at an impact energy of 200 eV followed by annealing to (a) 370 K and (b) 600 K 57

Figure 4.3 Temperature programmed desorption profiles of the parent ion (mass 28) of N_2 for Cu(100) ion-irradiated at an impact energy of 200 eV with N_2 dosages of (a) 3 kL, (b) 12 kL, and (c) 36 kL 59

Figure 4.4 Temperature programmed desorption profiles of the parent ion (mass 28) of N_2 for Cu(100) ion-irradiated with 72 kL of N_2 at an impact energy of (a) 50 eV, (b) 75 eV, and (c) 100 eV 60

Figure 4.5 Temperature programmed desorption profiles of the parent ion (mass 28) of N_2 for a clean Cu(100) surface ion-irradiated with 36 kL of N_2 at an impact energy of (a) 50 eV and (b) 200 eV, with and without Ar^+ pre-sputtering at 500 eV 62

Figure 5.1 Vibrational electron energy loss spectra for (a) a clean Cu(100) surface ion-irradiated in 9 kL of C_2H_4 at 200 eV impact energy at room temperature, and for sample (a) annealed to (b) 370 K, (c) 470 K, (d) 570 K, and (e) 670 K 68

Figure 5.2 Vibrational electron energy loss spectra for (a) a clean Cu(100) surface ion-irradiated in 9 kL of C_2D_4 at 200 eV impact energy at room temperature, and for sample (a) annealed to (b) 370 K, (c) 470 K, (d) 570 K, and (e) 670 K 69

Figure 5.3 Plausible hydrocarbon species adsorbed on Cu(100) after low-energy ion irradiation in ethylene at room temperature 71

Figure 5.4 Temperature programmed desorption profile of the parent ion (mass 4) of deuterium for Cu(100) ion-irradiated in 9 kL of C_2D_4 at 200 eV impact energy 74

Reproduced with permission of the copyright owner. Further reproduction prohibited without permission.

Figure 5.5 Vibrational electron energy loss spectra for a nitrogen-precovered Cu(100) surface ion-irradiated at 200 eV impact energy in 5 kL of C_2H_4 and annealed to (a) 350 K, (b) 400 K, (c) 550 K, and (d) 680 K 76

Figure 5.6 Vibrational electron energy loss spectra for a nitrogen-precovered Cu(100) surface ion-irradiated at 200 eV impact energy in 9 kL of C_2D_4 and annealed to (a) 350 K, (b) 400 K, (c) 550 K, and (d) 680 K 77

Figure 5.7 Temperature programmed desorption profiles of the parent ions of (a) D_2 (mass 4), (c) CN (mass 26) and (d) N_2 (mass 28), and of mass 14 (corresponding to the N atoms dissociated from N_2 in the ionizer) for a nitrogen-precovered Cu(100) surface ion-irradiated in 9 kL of C_2D_4 at 200 eV impact energy 81

Figure 6.1 (A) Top view of the dimer-adatom-stacking fault (DAS) model of Si(111)7×7. Atoms in the (111) layer at increasing depth are indicated by circles of decreasing size. (B) Side view along the diagonal of the unit cell. (C) The structure and bonding at the rest-atom and adatom sites 85

Figure 6.2 AES spectra of common contaminants on Si(111) surface (a) without cleaning, and with (b) two and (c) four cleaning cycles (each cleaning cycle consisted of 30 minutes of Ar^+ sputtering and annealing to 1200 K) 88

Figure 6.3 Vibrational electron energy loss spectra for residual carbon contamination on Si(111)7×7, after (a) 4, (b) 6, (c) 8 cleaning cycles (each consisting of 30 minutes Ar^+ of sputtering and annealing to 1200 K) 89

Figure 6.4 A typical mass spectrum of ambient gas at $2x10^{-10}$ Torr 91

Figure 6.5 Vibrational electron energy loss spectra for (a) clean Si(111)7×7, and after (b) 10, and (c) 24 hours in an ambient

Reproduced with permission of the copyright owner. Further reproduction prohibited without permission.

pressure of $2x10^{-10}$ Torr..... 92

Figure 6.6 Vibrational electron energy loss spectra for a 200 L O_2 exposure on (a) a clean Si(111)7×7 surface, and sample (a) exposed to $2x10^{-10}$ Torr ambient gas for (b) 10 hours, and (c) 24 hours..... 94

Figure 6.7 Vibrational electron energy loss spectra for carbon deposition on Si(111)7×7 by annealing (a) a clean Si(111)7×7 surface in ethylene for (b) 50 L, and (c) 2000 L at 800 K..... 96

Figure 6.8 Vibrational electron energy loss spectra for (a) clean Si(111)7×7, (b) sample (a) exposed to an equivalence of 10 L of ambient gas commonly found in an ultrahigh vacuum chamber, (c) sample (a) dosed with 1000 L of ethylene at 800 K, and (d) sample (c) exposed to an equivalence of 70 L of ambient gas..... 97

Figure 6.9 Vibrational electron energy loss spectra for 200 L of oxygen adsorption on (a) a clean Si(111)7×7, (b) C-covered Si(111), prepared by dosing sample (a) with 1 kL of ethylene at 800 K..... 98

Figure 7.1 Electronic electron energy loss spectra for (a) clean Si(111)7×7 and after exposure of 1 kL of oxygen with sample (a) held at (b) 300 K, (c) 550 K, and (d) 700 K..... 104

Figure 7.2 Electronic electron energy loss spectra for Si(111)7×7 with (a) 1 kL oxygen exposure at 300 K and sample (a) annealed to (b) 700 K and (c) 1270 K..... 106

Figure 7.3 Vibrational electron energy loss spectra for 2 kL oxygen exposed to Si(111)7×7 surface at (a) 300 K and (b) 700 K..... 107

Figure 7.4 Electronic electron energy loss spectra for Si(111)7×7 (a) ion-irradiated at 300 K with 1 kL of O_2 at 200 eV, and sample (a) annealed to (b) 700 K and (c) 1270 K..... 108

Figure 7.5 Relative intensity of a carbon-related feature for Si(111)7×7

Reproduced with permission of the copyright owner. Further reproduction prohibited without permission.

annealed at 800 K as a function of ethylene dose in (a) HREELS (at 826 cm^{-1} energy loss) and (b) AES spectra (at 274 eV kinetic energy)..... 110

Figure 7.6 Electronic electron energy loss spectra for a clean Si(111)7×7 surface (a) held at 800 K during exposure of 1 kL (b) and 10 kL of ethylene (c)..... 112

Figure 7.7 Vibrational electron energy loss spectra for Si(111)7×7 (a) exposed with 1 kL of C_2H_4, (b) ion-irradiated with 1 kL C_2H_4 at 200 eV impact energy, (c) sample (a) annealed to 1000 K, and (d) sample (b) annealed to 1000 K..... 114

Figure 7.8 Electronic electron energy loss spectra for Si(111)7×7 (a) with ion-irradiated in 10 kL ethylene at 50 eV impact energy, followed by annealing to (b) 800 K, and (c) 1270 K..... 115

Figure 7.9 AES spectra for Si(111)7×7 (a) ion-irradiated in 10 kL ethylene at 50 eV impact energy and annealing to 1270 K, (b) followed by further ion irradiation with 5 kL, and with (c) additional 5 kL, and (d) sample (c) annealed to 1270 K..... 116

Figure 7.10 Typical carbon KLL Auger lines of graphite (sp^2), natural diamond (sp^3), and SiC 117

Figure 7.11 Electronic electron energy loss spectra for (a) clean Si(111)7×7, (b) sputtered in 100 kL of ethylene at 50 eV impact energy, followed by annealing to (c) 800 K and (d) 1270 K..... 119

Reproduced with permission of the copyright owner. Further reproduction prohibited without permission.

Chapter 1
INTRODUCTION

1.1 General surface processes

With the advent of new surface characterization techniques, macroscopic surface phenomena (adsorption, desorption, surface chemical reactions, ion and electron scattering, surface diffusion and migration, and nucleation, etc.) are being reexamined on the molecular scale [1]. These studies not only provide critical information to improve our understanding of the nature of surfaces, but also are the driving force for a variety of technologies, including surface catalysis, thin films deposition, and novel material synthesis. A typical surface science example for heterogeneous catalysis is the famous CO oxidation problem, which has been widely studied on a variety of metal surfaces (in particular, platinum-group metals) because of its application to automobile exhaust decontamination [2]. The role of the metal surface is to provide an easier path for oxygen dissociation and a platform to support a higher reactant concentration for enhancing the reaction probability. The goals in these catalysis-related surface science studies are to identify the active sites where bond breaking and rearrangement take place and to detect any relevant surface intermediates [1]. In the area of thin films deposition, the initial processes for film growth also involve many primary surface steps such as bond breaking, surface adsorption, surface reaction, desorption, surface migration, and nucleation [3]. All of these surface processes control, to various extents, the properties of the resulting films. Understanding how the initial processes occur at the molecular level will therefore be crucial for achieving better film properties and for developing novel materials.

1.1.1 Surface adsorption, coadsorption, and surface reactions

There are three general types of interaction forces between an adsorbed particle and the surface, depending on the individual system involved: van der Waals, ionic and covalent forces. The van der Waals force produced by mutually induced dipole moments is most evident in the adsorption of noble gases or other closed shell species. This kind of adsorption with a typically low heat of adsorption of 10-20 kJ/mol is called physisorption. The other two types of forces lead to chemisorption involving larger bonding strengths comparable to normal chemical bonds (with the heats of adsorption in the range of 80-500

Reproduced with permission of the copyright owner. Further reproduction prohibited without permission.

kJ/mol) [4]. All the adsorption processes reported in the present work may be considered as chemisorption. The adsorption can also be divided into activated adsorption and non-activated adsorption depending on the shape of the Lennard-Jones potential. In the case of activated adsorption, the incoming molecule must possess a minimal energy in order to overcome the activation barrier for adsorption. From the point of view of the reactant gas, adsorption can also be classified as atomic (dissociative) adsorption and molecular (associative) adsorption depending on the bonding strengths of the gaseous particle and of the adsorbate-surface bonds. In the present work, we find examples for both kinds of adsorption, O/Cu(100) for the atomic adsorption and CO/Cu(100) for the molecular adsorption.

When different particles simultaneously adsorb on a surface, the particles could, under the appropriate conditions, coexist on the surface and interact with both the surface and with one another. There are two kinds of coadsorption [4]: competitive coadsorption whereby different particles compete for the same type of adsorption sites, and cooperative coadsorption when it is more energetically favorable for different particles to become neighbors. In the present work, we see examples of both types of coadsorption at work. In particular, the coadsorption of CO with surface oxygen and carbon on Cu(100) and that of oxygen with ambient gas on Si(111)7×7 will be investigated.

A typical surface reaction generally involves at least five discrete steps: (1) trapping, (2) adsorption (chemisorption), (3) surface migration (diffusion), (4) chemical reorganization of reactants (chemical reaction), and (5) desorption of product(s) [4]. Surface reactions may be divided into three general categories: corrosion reactions, crystal growth reactions, and catalytic reactions [5]. In our experiments, the formation of oxide layers on Cu(100) and on Si(111)7×7 can be considered as the results of corrosion reactions. The formation of a carbon layer on Si(111) can be regarded as an initial stage of a crystal growth reaction. Furthermore, when a reaction involves interactions between two reactants both in the adsorbed state, the reaction is said to follow the Langmuir-Hinshelwood (LH) model [6]. When the reaction involves a reactant from the gas phase and one in an adsorbed state, it follows the Eley-Rideal model [7]. Most of the surface reactions encountered in our experiments can be classified as LH reactions.

Reproduced with permission of the copyright owner. Further reproduction prohibited without permission.

Surface adsorption and reactions have been studied extensively with a variety of surface science techniques during the past thirty years [8]. Most of these studies tended to focus on simple adsorbates with well defined single crystal substrates under ultra-high vacuum (UHV) conditions. Although this "simplified" approach can be used to identify the well-defined reaction model and to provide further understanding on surface reactions microscopically, the results so obtained do not realistically represent what goes on in the case of practical surfaces [4]. In particular, industrial reactions are conducted under quite different conditions, namely, at atmospheric (or even higher) pressures and often with much less well-defined surfaces such as powders, pellets, thin films, or polycrystalline sheets. Today, more surface science experiments are increasingly focussing on systems involving more complicated molecules with less well defined surfaces by using modern surface analysis techniques and are trying to overcome this "pressure gap" problem by incorporating high pressure reaction cells in their UHV apparatus [4]. In the present work, in addition to investigating the adsorption on clean surfaces, we extend our study to less well-defined surfaces modified by artificial contamination and reactive ion bombardment. The nature of these surfaces is closer to those encountered in industrial applications, such as chemical vapor deposition (CVD) and device fabrication.

1.1.2. Electron and ion induced surface processes

Electron and ion-induced chemical reactions have been studied and used for industrial applications for many years [9], because they offer different mechanisms and new reaction pathways from the thermally induced processes. In recent years, new technologies involving ion or plasma assisted surface reactions have been widely used for the development of novel materials [3,10]. When an electron or ion beam impinges onto a surface, the charged particles can produce chemically-activated species near the surface region, which could undergo chemical reactions with the substrate or other adsorbates that may not be achievable by normal thermal gas-surface reactions. For example, electron dissociation of H_2 can be used to produce atomic hydrogen for passivating a silicon surface [11]. Electron or ion irradiation can also be used to produce ordered overlayers such as c(2×2)N on a Cu(100) surface [12]. Plasma-activated silane decomposition reaction can lead to deposition of amorphous silicon [13].

Reproduced with permission of the copyright owner. Further reproduction prohibited without permission.

When low-energy electrons interact with a gaseous molecule, the resulting excited molecule can undergo one of the following processes [10], in the order of increasing impact energy: (1) electronic relaxation back to the ground state, (2) dissociation, or (3) ionization. When electrons interact with species adsorbed on the surface, additional processes such as desorption, migration, and chemical reaction can also occur. Because of the relatively small mass of the electron, no significant defects to the surface itself are expected to be introduced if the electron energy is less than several hundred electron volts [10].

On the other hand, when a low-energy ion (<500 eV) collides with a surface, much more complicated processes can occur [3,14]. In particular, the following processes can be induced: (1) adsorbate removal or chemical activation, (2) lateral displacement, (3) surface vacancy creation by sputtering, (4) surface vacancy creation by displacement to an adatom position, (5) knock-on implantation, (6) crevice filling by ion-enhanced surface mobility, (7) crevice filling by forward sputtering, and (8) breakup of three-dimensional nucleus [14]. Between a few electron volts and a few tens of electron volts, impinging particles have sufficient energy to cause rearrangement of the surface but not of the bulk. Bombardment within this energy window is especially useful for epitaxial growth, because it can modify growth behavior without causing subsurface damage. Ion impact within this energy range can also cause chemical activation of molecules in the reactant gas or of adsorbates on the surface. After the molecular ions collide with the surface, they could be neutralized by surface electrons. The energy released due to neutralization and the translational kinetic energy will cause further dissociation of the molecular ions [15]. If the dissociated fragments (free radicals) are reactive to other surface species, new species will be produced. Ion bombardment can also be used to dissociate adsorbed molecules and thereby activate them chemically. Ion activation of adsorbed CVD precursors is therefore an important mechanism in film deposition. Furthermore, within this energy regime, small ions such as H^+ and N^+ can penetrate the surface and become implanted in the substrate lattice, transferring energy to the substrate atoms along their trajectory until they come to rest. At a higher impact energy (~100 eV), larger ions can also be implanted causing defects to the bulk. At a still higher impact energy (several hundreds of eVs), some of the displaced substrate atoms escape from the surface as sputtered-off particles. High-energy sputtering

Reproduced with permission of the copyright owner. Further reproduction prohibited without permission.

(> 400 eV) could indeed cause serious damage to the surface. Of interest in the experiments of the present work, a recent scanning tunneling microscopy (STM) image showed that 400 eV Ar^+ bombardment on Cu(100) could cause rectangularly shaped vacancy islands about 5 atomic layers deep and 20 nm wide [16]. The STM image for a Si(111)7×7 surface bombarded by 3-keV Ar^+ ions also showed the formation of craters with an average depth of a monatomic step height [17]. Annealing both the sputtered Cu(100) and Si(111)7×7 surfaces can restore their original surface crystallographic structures.

Although electron- and ion-assisted surface reactions have been used in thin films deposition and other material processing procedures for many years, the fundamental research on these kinds of reaction from the point of view of surface science is considerably less extensive. Recently more and more studies have concentrated on applying advanced surface analysis techniques to examining the mechanisms and initial stages of these reactions, in an attempt to gain further understanding of these processes at the molecular level [18]. It is also the goal of our present work to investigate some of the novel aspects in electron- or ion-induced adsorption and surface reactions on typical metal and semiconductor surfaces by using standard surface analysis techniques in a UHV environment.

1.2 Surface analysis techniques

During the past two decades, a great number of new surface analysis techniques have been developed [4,19]. In the present work, we use several of these techniques, which include: (1) high resolution electron energy loss spectroscopy (HREELS), (2) extended-range electron energy loss spectroscopy (ELS*), (3) temperature programmed desorption (TPD) mass spectroscopy, (4) low energy electron diffraction (LEED), and (5) Auger

---

* In the literature, the acronyms ELS and EELS are commonly used for extended-range electron energy loss spectroscopy for studying electronic transitions and plasmon excitations, while HREELS and EELS are used to represent high resolution electron energy loss spectroscopy for detecting the vibrational excitations. In this thesis, we treat HREELS and ELS as two separate techniques because of the different information that they provide.

Reproduced with permission of the copyright owner. Further reproduction prohibited without permission.

electron spectroscopy (AES). Since details of these techniques can be found in many general reviews [4,19], only brief descriptions are given below.

1.2.1 High resolution electron energy loss spectroscopy

In a typical HREELS experiment, a beam of monoenergetic (1-10 eV) electrons is used to excite the vibrational motions of the species adsorbed on a surface. The electron beam is usually produced by a thermionic electron source coupled to an electron monochromator that selects a small portion of the "thermal" Maxwellian distribution of the emitted electrons. An electron energy analyzer is used to analyze the kinetic energy of the scattered electrons. The energy loss suffered by the inelastically scattered electrons corresponds to the excitation energy of the vibrational mode of interest in the adsorbed species. The theoretical and instrumental aspects of HREELS have been discussed in great details by Ibach and Mills [20]. Briefly, there are two kinds of inelastic interactions for an electron with a surface: dipole scattering (long-range interaction) [21] and impact scattering (short-range interaction) [22]. In dipole scattering, an electron interacts with the dipole potential of an adsorbate and the corresponding scattering cross section is strongly peaked in the forward direction of the specular reflection. Any dipole (from the adsorbate) on the surface induces an image dipole within the surface. If the dipole orientation is normal to the surface, the effect is enhanced by the image dipole. However, if the orientation is parallel to the surface, the effect is annihilated by the image dipole. This kind of scattering therefore follows the normal dipole selection rule [23]. On the other hand, impact scattering occurs only at a very small distance (impact parameter) from the adsorbate and it greatly depends on the shape of the electron-adsorbate interaction potential. In general, all vibrational modes, including the dipole-forbidden ones, are active to impact scattering and can be detected in the off-specular direction. The cross section for impact scattering can be calculated by using quantum-mechanical scattering theories [20]. Since the cross section for impact scattering in the specular direction is generally much smaller than that for dipole scattering, impact scattering is usually investigated in the off-specular direction.

HREELS technologies have been improved dramatically over the past twenty years. Nowadays, a state-of-the-art HREELS instrument can deliver sub-meV energy resolution [24,25]. It has become a standard surface analysis tool for obtaining valuable information

Reproduced with permission of the copyright owner. Further reproduction prohibited without permission.

about chemical bonding of the adsorbates, the nature of the adsorption site, and structural specificity of the adsorbate and the substrate.

1.2.2 Extended-range electron energy loss spectroscopy

Extended-range electron energy loss spectroscopy, or ELS for short, is similar to HREELS; it also employs monoenergetic electrons to probe the surface and to determine the distribution of the scattered electrons as a function of the energy loss and scattering geometry. Instead of detecting the information about vibrational excitations, ELS is used to obtain information about electronic excitations of the adsorbates and the surface [26,27,28]. The energy range of the incident beam is usually much higher (typically 30-1000 eV) than that used in HREELS (<30 eV). The energy range of the scattered electron is also correspondingly higher. The incident electrons in this energy range can stimulate electronic transitions within the valence band of the solid (a few eV) and collective oscillations of the electron sea of the solid (plasmons). The electron scattering process follows the general conservation of energy and momentum:

$$E^S(\mathbf{K}^S) = E_0(\mathbf{K}) - \hbar\omega \quad \text{(energy conservation)} \tag{1}$$

$$K^S_{\parallel} = K_{\parallel} - q_{\parallel} \pm G_{\parallel} \quad \text{(momentum conservation)} \tag{2}$$

where E_0 and E^S ($\mathbf{K}$ and $\mathbf{K}^S$) are the energies (momenta) of the incident and scattered electron respectively. $\hbar\omega$ is the energy loss suffered by the incident electron. $q_{\parallel}$ is the momentum transfer parallel to the surface and $G_{\parallel}$ is the reciprocal surface lattice vector. The subscript $\parallel$ is used to indicate the surface parallel component. According to these equations, there are three different ways to perform measurements: (1) differential cross section measurements by scanning the incident energy, (2) angular dependent measurements by performing the experiments as a function of the scattering angle, and (3) energy loss measurements by analyzing the energy distribution of the scattered electrons at a preselected scattering geometry. The last method is commonly used in modern ELS experiments and is also the method of choice in the present work. Detailed calculations of the scattering cross sections involve dielectric theories and are discussed in great detail in Ref. 20. Because an ELS spectrum contains information about bulk plasmon, surface plasmon, and both interband and intraband transitions, it has been found to be extremely useful in characterizing thin film properties [29,30].

Reproduced with permission of the copyright owner. Further reproduction prohibited without permission.

1.2.3 Temperature programmed desorption

Temperature programmed desorption TPD [also known as Thermal Desorption Spectrometry (TDS)] is one of the earliest techniques used for investigating the nature of adsorbates on surfaces [4,31]. In a typical TPD experiment, an adsorbate is thermally excited, and the desorbed species are detected by a mass spectrometer [19]. The desorption process can be described by the Wigner-Polanyi equation [4]:

$$-\frac{d\sigma}{dt} = \nu_{(x)}\sigma^{x}\exp(-\frac{\Delta E^{*}_{des}}{RT}) \tag{3}$$

where σ is the number of adsorbed particles on the surface, ν is the frequency factor, x denotes the desorption order, ΔE^{*}_{des} is the activation energy, t is the time, and T is the temperature. With the assumption of constant ΔE^{*}_{des} and ν (e.g., no adsorbate-adsorbate interaction), it is possible to work out a relationship between ΔE^{*}_{des} and the temperature of maximum desorption, as well as the shape of the desorption profile according to the order of desorption [4,31]. However, these results are only valid at very low coverage and the desorption behavior at high coverage may be quite different from the results predicted by the above theory [32]. Although there are some difficulties in determining the desorption energy quantitatively due to the potential coverage-dependent problem, TPD can provide valuable qualitative information about the nature of the adsorption states and has continued to be widely used for studying chemisorption in surface science.

1.2.4 Low energy electron diffraction

Low energy electron diffraction (LEED) is a very useful tool for determining the long-range order of the surface structure. In a typical LEED experiment, monoenergetic low-energy electrons (<500 eV) elastically scattered off the surface are collected by a phosphorus screen positively biased at a high potential [33]. There are several improved LEED instruments, such as the one based on a reverse-view system coupled with a TV (or CCD) camera and computer-controlled data acquisition software (Video-LEED) [34], and an instrument with a high resolving power for analyzing the profiles of the diffraction spots [SPA (spot profile analysis) LEED] [35]. A LEED pattern is produced by diffraction of an electron plane wave (with wavelength of the order of 1 Å) at an appropriate kinetic energy. LEED is similar to X-ray diffraction, but is more surface-sensitive because of the smaller

Reproduced with permission of the copyright owner. Further reproduction prohibited without permission.

penetration depth of the low-energy electrons. A LEED pattern with intense well-defined spots and low background intensity is indicative of a highly ordered surface overlayer, while that with diffuse or streaky diffraction spots indicates a disordered surface. Although a LEED pattern carries the symmetry information of the overlayer region, any lateral displacement of the adsorbate lattice (parallel to the substrate lattice) results in identical diffraction patterns. To determine surface structure quantitatively, kinetic diffraction theories used in X-ray diffraction are usually not appropriate because of the multiple scattering problem. There is a need for dynamical LEED theories that deal with the complex problems of intralayer and interlayer scattering [33,36].

1.2.5 Auger electron spectroscopy

In Auger electron spectroscopy (AES), a high-energy incident electron beam (1000-10000 eV) is used to probe the surface, producing ionization of the adsorbates and/or substrate atoms. The secondary electrons are energy-analyzed by an electron energy analyzer [37]. Following ionization, the excited state relaxes by the ejection of either an X-ray photon (X-ray fluorescence) or an Auger electron (Auger decay). The kinetic energy of the Auger electron is given by [4]:

$$E_{kin} = E_1 - E_2 - E_3 \tag{4}$$

where E_1 denotes the binding energy of the initial core electron prior to ionization, E_2 is that of the electron that fills the core hole, and E_3 is the binding energy of the ejected Auger electron. Because the kinetic energy of the Auger electron is characteristic of the energy levels of the core hole and the upper state that fills the core hole, it is a very useful element-specific analytical tool for determining elemental surface concentrations. However, the high energy of the incident electron beam could introduce local destructive effects, which could induce desorption, decomposition, or even melting of the adsorbates and substrate. In addition to the elemental composition analysis, the line shape of an Auger transition also contains useful information about the bonding type [38,39] and has recently been used to characterize carbon nucleation on a silicon surface [40,41].

Reproduced with permission of the copyright owner. Further reproduction prohibited without permission.

1.3 Structure of this thesis

Further details about individual experiments in the present work will be presented in Chapter 2. The research work reported in the remainder of this thesis focus on the effect of low-energy electron and ion irradiation on typical surfaces and can be divided into two parts. In the first part, Chapters 3, 4, and 5, we investigated the basic adsorptions and surface reactions induced by low energy electron and ion irradiation on Cu(100). As a structurally simple and unreactive surface, Cu(100) is an ideal surface for us to study the complicated electron or ion induced surface processes and to detect new surface species generated by electron or ion irradiation. Moreover, Cu(100) surface is also a good platform for testing the performance of our custom-built EELS spectrometer because of its highly conductive nature. In this part, the generation of "stabilized" CO at room temperature by low-energy electron and ion irradiation on clean, C-precovered, and O-precovered Cu(100) surfaces is reported in Chapter 3. The coexistence of atomic nitrogen adsorption and embedded nitrogen on Cu(100) produced by ion irradiation is discussed in Chapter 4. The formation of novel C and N-containing species on Cu(100) induced by ion irradiation is investigated in Chapter 5. In the second part, Chapters 6 and 7, the surface contamination and the formation of oxygen and carbon layers on Si(111)7×7 are investigated. In particular, contamination of common surface contaminants including ambient gas, oxygen, and carbon, and the nature of their coadsorption on Si(111)7×7 are examined by HREELS, AES and LEED in Chapter 6. Chapter 7 reports an ELS characterization of the formation of SiO_2 and SiC overlayers on Si(111)7×7. These topics are of great practical interests in the area of thin film deposition and device fabrication. Finally, in Chapter 8, some general observations about the electron- or ion-induced adsorption and surface reactions in the present work are made and an outlook on future experiments is presented.

1.4 References

[1] Gabor A. Somorjai, "Introduction to Surface Chemistry and Catalysis", Wiley, Toronto (1994).

[2] K. C. Taylor, "Catalysis – Science and Technology", J. R. Anderson and M. Boudart (eds.), Plenum, New York (1984), p120.

Reproduced with permission of the copyright owner. Further reproduction prohibited without permission.

[3] D. L. Smith, "Thin Film Deposition Principles and Practice", McGraw-Hill, New York (1995).

[4] K. Christmann, "Surface Physical Chemistry", edited by H. Baumgartel, E.U. Franck, and W. Grunbein (eds.), Springer-Verlag, New York (1991).

[5] J. B. Hudson, "Surface Science: An Introduction", Butterworth-Heinemann, Toronto (1992).

[6] H. P. Bonzel and R. Ku, Surf. Sci. **39**, 91 (1972).

[7] D. D. Eley, Chem. Ind. **1**, 12 (1976).

[8] G. A. Sormorjai, "Chemistry in Two Dimensions", Cornell University Press, Ithaca, New York (1981).

[9] "Chemical Reactions in Electrical Discharges", R. F. Gould (ed.), Advances in Chemistry Series **80**, American Chemical Society, Washington, D.C. (1967).

[10] M. Ohring, "The Materials Science of Thin Films", Academic, Toronto (1992).

[11] H. Froitzheim, U. Kohler and H. Lammering, Surf. Sci. **149**, 537 (1985).

[12] M. H. Mohamed and L. L. Kesmodel, Surf. Sci. Lett. **185**, L467 (1987).

[13] M. J. Kushner, J. Appl. Phys. **63**, 2532 (1988).

[14] "Low Energy Ion-Surface Interaction", J. W. Rabalais (ed.), Wiley (1994).

[15] J. S. Martin, J. N. Greeley, J. R. Morris, B. T. Feranchak, and D. C. Jacobs, J. Chem. Phys. **100**, 6791 (1994).

[16] M. Ritter, M. Stindtmann, M. Farle, and K. Baberschke, Surf. Sci. **348**, 243 (1996).

[17] H. J. W. Zandvliet, H. B. Elswijk, E. J. van Loenen, and I. S. T. Tsong, Phys. Rev. B **46**, 7581 (1992).

[18] I. Kusunoki, T. Takaoka, Y. Igan, and K. Ohtsuka, J. Chem. Phys. **101**, 8238 (1994).

[19] J. C. Riviere, "Surface Analytical Techniques", Clarendon, Oxford (1990).

[20] H. Ibach and D. L. Mills, "Electron Energy Loss Spectroscopy and Surface Vibrations", Academic, New York (1982).

[21] F. M. Propst and T. C. Piper, J. Vac. Sci. Technol. **4**, 53 (1967).

[22] W. Ho, R. F. Willis and E. W. Plummer, Phys. Rev. B **21**, 4202 (1980).

[23] D. M. Newns, "Vibrational Spectroscopy of Adsorbates", R. F. Willis (ed.), Springer, New York (1980).

Reproduced with permission of the copyright owner. Further reproduction prohibited without permission.

[24] H. Ibach, "Electron Energy Loss Spectrometers", Springer Ser. Opt. Sci., vol. **63**, Springer, New York (1991).

[25] H. Ibach, J. Electron Spectrosc. and Relat. Phenom. **64/65**, 819 (1993).

[26] D. P. Woodruff and T. A. Delchar, "Modern Techniques of Surface Science", Cambridge Solid State Science Series, Cambridge University Press, New York (1986).

[27] "Electron Spectroscopy for Surface Analysis", H. Ibach (ed.), Springer, New York (1977).

[28] H. Froitzheim and H. Ibach, Z. Phys. **269**, 17 (1974).

[29] P. Kovarik, E. B. D. Bourdon, and R. H. Prince, Phys. Rev. B **48**, 12123 (1993).

[30] F. Bozso, J. T. Yates, Jr., W. J. Choyke, and L. Muehlhoff, J. Appl. Phys. **57**, 2771 (1984).

[31] D. A. King, Surf. Sci. **47**, 384 (1975).

[32] H. Froitzheim, P. Schenk, and G. Wedler, J. Vac. Sci. Technol. A **11**, 345 (1993).

[33] M. A. Van Hove, W. H. Weinberg, and C. M. Chan, "Low-Energy Electron Diffraction", Springer, New York (1986).

[34] "The Structure of Surface", S. Y. Tong and M. A. van Hove (eds.), Springer, New York, (1982).

[35] U. Scheithauer, G. Meyer, and M. Henzler, Surf. Sci. **178**, 441 (1986).

[36] J. B. Pendry, "Low Energy Electron Diffraction", Academic, New York (1974).

[37] J. T. Grant, Appl. Surf. Sci. **13**, 35 (1982).

[38] T. W. Hass, J. T. Grant, and D. J. Dooley, J. Appl. Phys. **43**, 1853 (1972).

[39] P. G. Lurie and J. M. Wilson, Surf. Sci. **65**, 476 (1977).

[40] Y. W. Ko and S. I Kim, J. Vac. Sci. Technol. A **15**, 2750 (1997).

[41] E. Grossman, G. D. Lempert, J. Kulik, D. Matron, J. W. Rabalasis, and Y. Lifshitz, Appl. Phys. Lett. **68**, 1214 (1996).

Reproduced with permission of the copyright owner. Further reproduction prohibited without permission.

Chapter 2
EXPERIMENTAL DETAILS

2.1 Experimental setup and sample preparation

Details of the experimental apparatus used in the present work have been described previously [1]. Briefly, all the experiments were performed in a home-built ultra-high vacuum chamber with a base pressure of better than 1×10^{-10} Torr, achieved by a 170 *l*/s turbomolecular pump (Balzers), a 230 *l*/s ion pump (Varian), and a 2000 *l*/s titanium sublimation pump (Varian). The chamber was equipped with an ion (-sputtering) gun (Physical Electronics), a 4-grid retarding-field optics (Omicron) for both reverse-view LEED and AES analyses, a 1-300-a.m.u. quadrupole mass spectrometer (QMS, Hiden Analytical) for TPD studies, and a home-built multi-technique electron energy loss spectrometer [1,2] for both HREELS and ELS measurements. The QMS was housed in a separate chamber that was differentially pumped by a 60 l/s ion pump.

For the experiments on the Cu(100) surface (Chapters 3-5), the Cu(100) sample (9.5 mm diameter × 2 mm thick) with a stated purity of 99.999% was purchased from Monocrystals Company. The sample was mechanically fastened to a grounded Ta sample plate with 0.25-mm-diameter Ta wires. Heating was provided by a boron nitride heater in contact with the backside of the substrate, with a 0.5-mm-thick Ta foil placed between the boron nitride heater and the sample. The sample was cleaned by repeated cycles of Ar^+ sputtering [at 500 eV (impact energy) and 10 mA (electron emission current) under an ambient Ar pressure of 2×10^{-5} Torr for 30 minutes] and annealing to 800 K, until a sharp 1×1 LEED pattern and no detectable Auger peaks attributable to such impurities as C, O and S were obtained.

For the Si(111) experiments (Chapters 6 and 7), the Si(111) sample (p-type boron doped, 50 Ω·cm, 8 × 6 mm^2 × 0.5 mm thick) with a stated purity of 99.999% was purchased from Virginia Semiconductor Inc. The sample was mechanically fastened to a grounded Ta sample plate with 0.25-mm-diameter Ta wires. The heating of the Si sample was achieved by electron bombardment from a heated tungsten filament at the backside of the sample. The Si(111) sample was cleaned by repeated cycles of Ar^+ sputtering [using the same

Reproduced with permission of the copyright owner. Further reproduction prohibited without permission.

conditions as those for Cu(100)] and annealing to 1200 K, until a sharp 7×7 LEED pattern and no detectable Auger peaks attributable to C, O and S were obtained. The cleanliness of the sample was further confirmed by the lack of detectable HREELS features attributable to unwanted contaminants. To avoid a hazy surface and carbon contamination during the annealing process, the sample was first outgassed at a lower temperature (900 K) for about 10 minutes, followed by flash annealing to 1200 K. During the flash sample annealing, the ambient pressure never exceeded 2×10^{-9} Torr. For both Cu(100) and Si(111), the surface temperature of the sample was monitored by a type K thermocouple (mechanically fastened to the front face of the sample) to an absolute accuracy of ± 20 K. The gaseous samples carbon monoxide, ethylene, oxygen (all at 99.99% purity), and nitrogen (at 99.9% purity) were purchased from Matheson, while ethylene-d_4 (at 98% purity) was obtained from Cambridge Isotope Laboratories, Inc. All the gaseous samples were used without further purification. All the exposures were performed by using variable leak valves, with the pressure monitored by an uncalibrated ionization gauge.

2.2 Irradiation by low-energy ion and electron beams

Ion irradiation (without mass selection) was performed by operating the ion gun with the chamber back-filled with the gas of interest at an ambient pressure of $\sim1\times10^{-6}$ Torr. The ion flux delivered to the sample was estimated to be 10 nA/mm^2. The setup for the ion irradiation is shown in Figure 2.1. The sample was positioned 5 cm from the front face of the ion gun during the ion irradiation experiments. The impact energy (IE) of the ion beam could be controlled by adjusting a floating voltage applied on the sample with respect to a preselected beam energy of the ion gun. The ion dose can be calculated from the product of the ion flux and the exposure time [obtained from the exposure in units of L (Langmuir) and the pressure employed (1×10^{-6} Torr)]. For example, the ion dose obtained from ion irradiation with 1 L of ethylene is $\sim10^{11}$ ions/mm^2. In the present experimental setup, the reactant gases were ionized by electrons with 200 eV kinetic energy inside the ion gun and only positive ions from the ion gun could reach the sample without mass selection. The concentration of each ion can be estimated from its cracking pattern [3]. For example, in the case of ethylene, $C_2H_4^+$ is the majority ion, with other smaller ions such as $C_2H_3^+$, $C_2H_2^+$,

Reproduced with permission of the copyright owner. Further reproduction prohibited without permission.

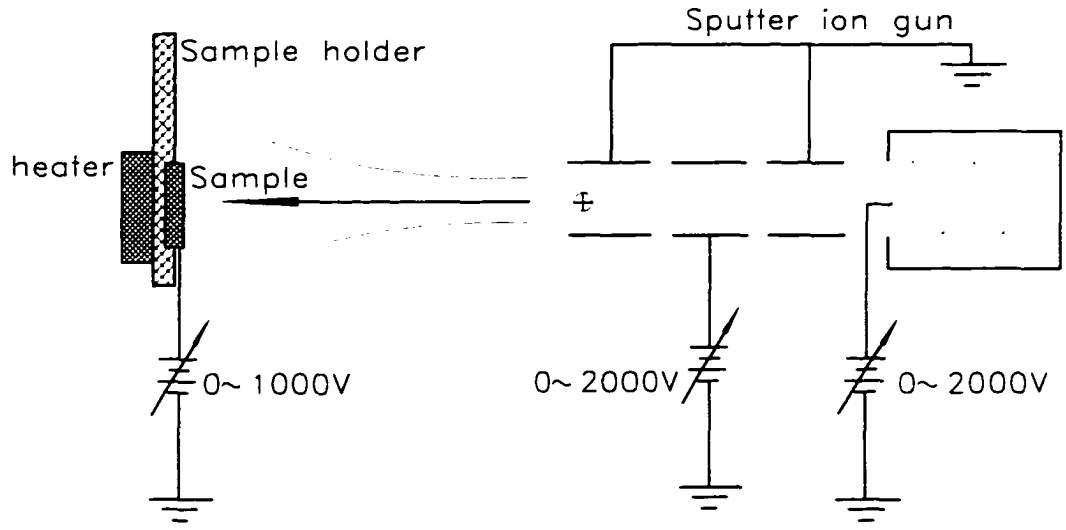

Figure 2.1 Experimental setup of low-energy ion irradiation.

C_2H^+, CH_2^+, and CH^+ present with decreasing concentrations. When the ions collide with the surface, they may become neutralized and may further dissociate into other smaller fragments including carbon and hydrogen atoms. The resulting radicals may in turn undergo reactions with the substrate atoms or pre-deposited adsorbates.

The electrons for our electron irradiation experiments were thermionically generated from a heated tungsten filament positioned 40 mm away from the sample at a typical flux of 2.7 $\mu A/mm^2$. The impact energy of electrons can be controlled by floating either the sample or the filament. The electron beam was not focused and it exhibited a broad flux distribution on the sample, which facilitated reasonably uniform exposure.

2.3 Electron energy loss experiments

In the past two decades, HREELS has become an increasingly important tool for surface analysis, with the energy resolution of the state-of-the-art spectrometer reaching the sub-meV level, i.e., below 4 cm^{-1} (or 0.5 meV) full-width-at-half-maximum (FWHM) [4,5]. Most of these spectrometers are, however, specially designed to probe surface vibrations using a low impact energy, which limits their applications for other types of experiments. We have developed a multi-technique portable analyzer for both low-impact-energy

Reproduced with permission of the copyright owner. Further reproduction prohibited without permission.

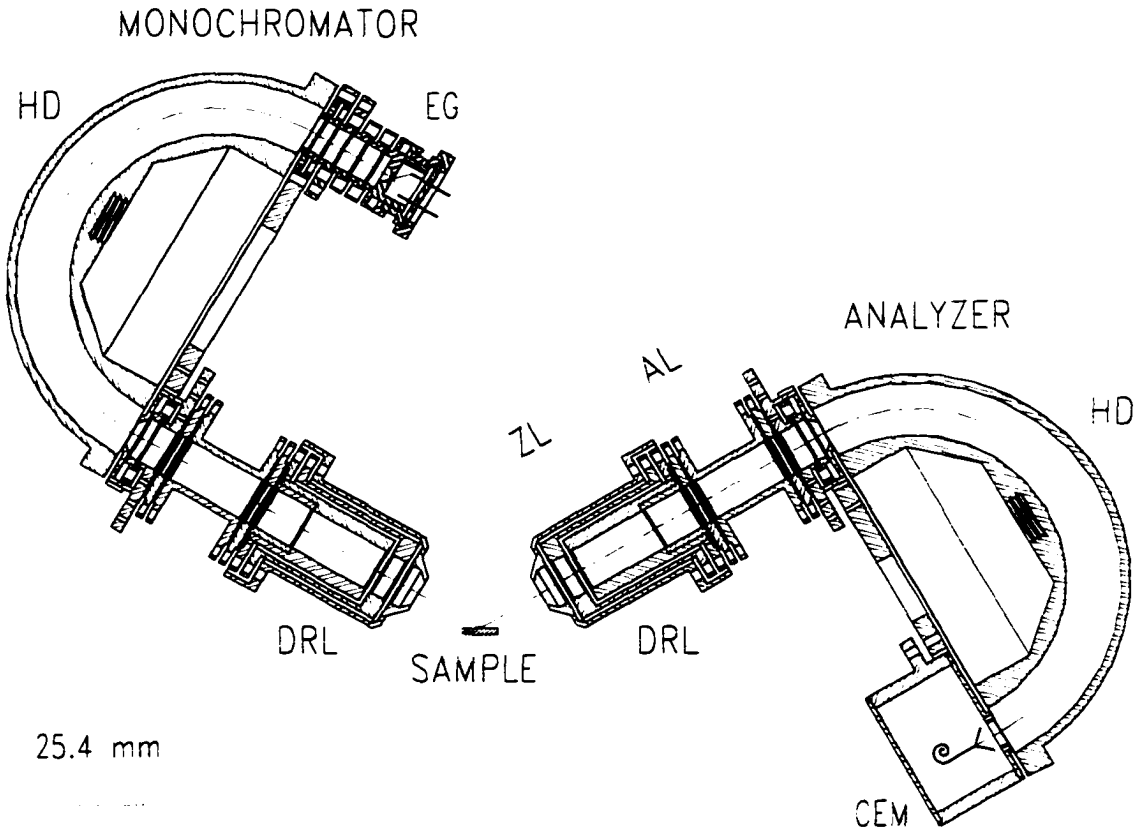

Figure 2.2 Schematic diagram of the electron energy loss spectrometer at the University of Waterloo. Legend: EG: Electron Gun, HD: Hemispherical Deflector, DRL: Double Retardation Lens, ZL: Zoom Lens, AL: Afocal Lens, CEM: Channel Electron Multiplier.

applications (as in surface vibrational spectroscopy) and high-impact-energy work (including investigations of electronic transitions and other phenomena). Details of this instrument have been given in Ref. 1. A schematic diagram of the current version of our EELS spectrometer is shown in Figure 2.2. Briefly, the analyser and the monochromator are separately mountable on 8-inch conflat flanges, which make them portable from one chamber to another. Both the monochromator and the analyzer are based on an identical electron optical design, which consists of a 51-mm-mean-radius hemispherical deflector (HD) coupled with a cylindrical double retardation lens (DRL) system [1]. The analyzer system is mounted on a single-axis goniometer and is rotatable around an axis perpendicular

Reproduced with permission of the copyright owner. Further reproduction prohibited without permission.

to the energy dispersion plane of the analyzer, hence making it suitable for angle-resolved experiments.

The general principle for designing an electrostatic lens can be found in Refs. 6 and 7. In our EELS instrument, the DRL system is capable of decelerating (and accelerating) electrons over a wide dynamic range of kinetic energy (up to a ratio of 1000), which enables the spectrometer to be used for different types of experiments requiring analysis of electrons over a wide energy range. This compound lens system can be divided into two elemental lenses: a 3-element zoom lens (ZL) and a 5-element afocal lens (AL), with a common electrode acting as a dividing aperture between the two elemental lenses [8]. When the analyzer is operated in the constant-absolute-resolution mode (i.e., with a fixed pass energy), the DRL is operated in a double focusing mode. As a first step in the initial optics optimization procedure, the 5-element AL is used to provide a high retardation ratio while the 3-element ZL serves as an einzel lens. The desired kinetic energy range can then be scanned by keeping the retardation ratio of the AL fixed while varying that of the 3-element ZL with respect to the scanning voltage, which results in an appropriate change in the overall retardation ratio of the entire 7-element DRL. In order to minimize the variation in the overall transmission function of the DRL while scanning over a wide dynamic range of electron energy, only the voltage of the second element in the 3-element ZL needs to be adjusted simultaneously to maintain an intermediate image at the centre of the dividing aperture. The DRL system can also be operated in a single focusing mode, which facilitates an acceptance half-angle smaller than 1.0°. This mode is particularly useful in angle-resolved experiments that require an angular resolution better than the nominal resolution of 1.5° half-angle.

To illustrate the typical performance attainable by our spectrometer, we show both the high-resolution and extended-range EELS spectra for a Cu(100) sample in Figure 2.3. The HREELS spectrum of CO/Cu(100) in Figure 2.3a clearly shows two prominent peaks at 338 cm^{-1} and 2084 cm^{-1}, which are in good accord with, respectively, the Cu–CO and C–O stretching frequencies reported previously [9,10,11]. In Figure 2.3b, the energy loss features of Cu(100) at 2.5 eV, 4 eV, and 10 eV can be assigned to interband transitions originating from the Cu d band while the feature at 7 eV corresponds to a bulk plasmon excitation [12].

Reproduced with permission of the copyright owner. Further reproduction prohibited without permission.

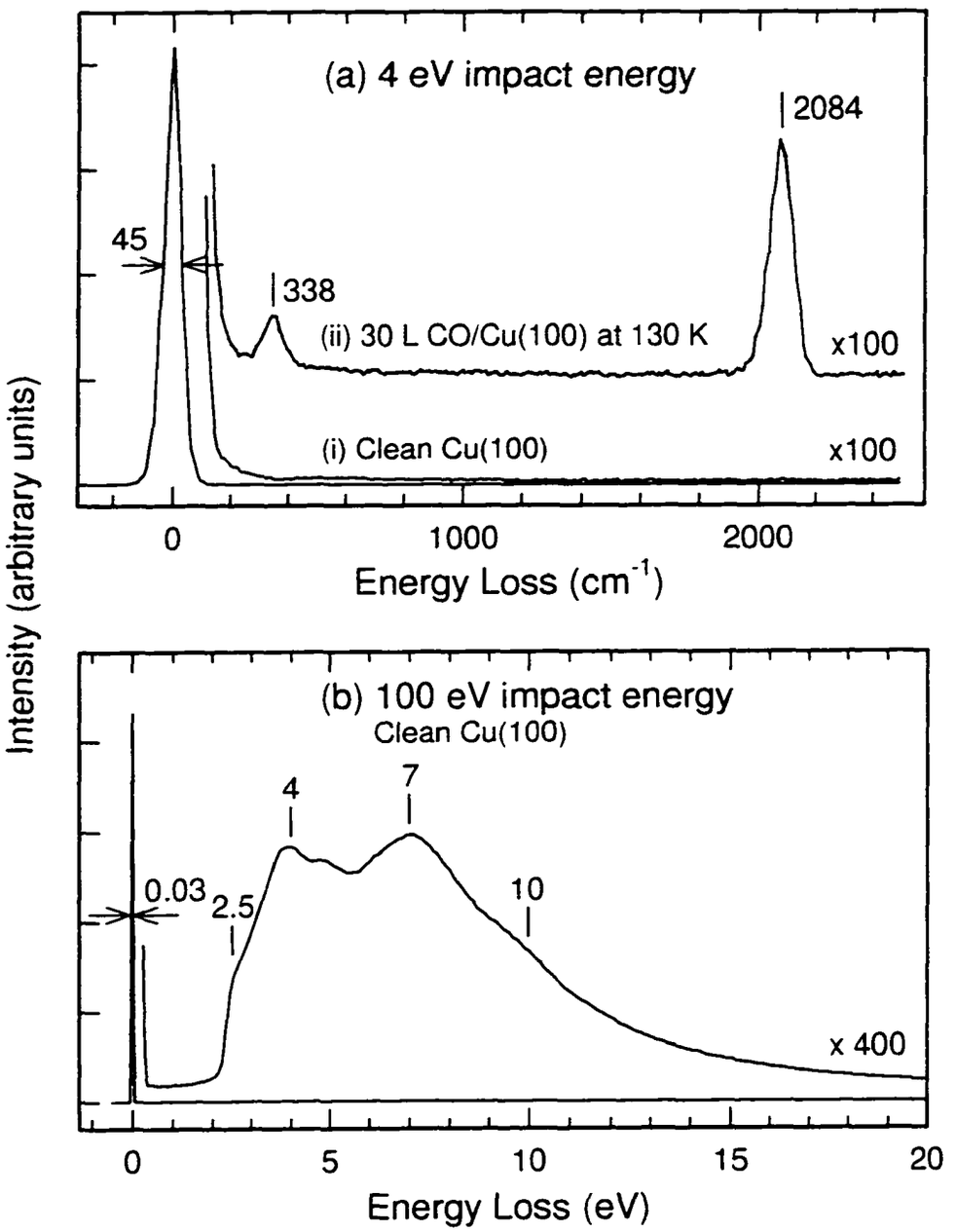

Figure 2.3 Typical electron energy loss spectra for (a) a clean Cu(100) surface with (ii) and without (i) a 30 L exposure of CO at 130 K collected at 4 eV impact energy, and for (b) a clean Cu(100) surface recorded at 100 eV impact energy over an extended energy loss range illustrating the onset of the electronic band structure.

Reproduced with permission of the copyright owner. Further reproduction prohibited without permission.

In the high resolution mode, our spectrometer is capable of an optimal energy resolution of 6.5 meV (45 cm^{-1}) FWHM, with a count-rate of 100,000 count-per-second (C/s) for the elastic peak, at a typical (low) impact energy of 4 eV (Figure 2.3a). In the high impact energy mode (e.g., 100 eV), the energy resolution becomes 30 meV FWHM (Figure 2.3b), which is considerably better than the performance of commercially available spectrometers. Our spectrometer therefore offers adequate performance for most of our applications, covering both the high-resolution vibrational studies and the extended-range electronic structural investigations.

In all our HREELS and ELS experiments the measurements were performed at RT except for the low temperature experiments presented in Chapter 3. The HREELS spectra were obtained at an impact energy of 4-10 eV in a specular reflection geometry (45°-60°) from the surface normal. Changing the impact energy and reflection geometry in these ranges was found to have no significant effects on the performance of the machine. The spectrometer was operated in the constant-resolution mode, in which the potential difference between the two hemispheres was fixed, hence giving a constant pass energy and a constant absolute resolution. The typical pass energy used was ~2.5 eV for both the analyzer and the monochromator. The use of a smaller pass energy was found to significantly decrease the signal intensity due to the residual magnetic field effect. On the other hand, use of higher pass energy was found to degrade the energy resolution. Due to the surface roughening effects created by ion irradiation in the experiments, the effective energy resolution was degraded from 64 cm^{-1} FWHM for a typical clean Cu(100) surface to 80-120 cm^{-1} FWHM after ion irradiation depending on the extent of sputtering. In the latter case, the absolute peak positions could be determined to an accuracy of ±16 cm^{-1} (or 2 meV) due to the broadened peaks. For a clean Si(111)7×7 surface, the typical resolution in HREELS experiment was degraded to 96-128 cm^{-1} with a higher tail from the elastic peak. The large tail was caused by the less conductive nature of a semiconductor and the presence of abundant sub-surface states in Si(111)7×7 [4]. The typical intensity of the elastic peak was also found to be reduced from 100 kC/s for a clean surface to 30-50 kC/s for sputtered surfaces with a typical noise count of less than 10 C/s.

Reproduced with permission of the copyright owner. Further reproduction prohibited without permission.

The tuning of an energy loss spectrometer can be a challenging process. The following procedures was found to be fairly effective: (1) find the electron beam by tracing the current at each aperture in both the monochromator and the analyzer; (2) optimize the signal by tuning the focusing voltages, deflector voltages, and magnetic field compensation (by adjusting the currents passing through the Helmhotz coils*); (3) optimize the energy resolution by slowly decreasing the pass energy and by varying the focus in the electron gun in order to improve the initial energy distribution; and (4) vary the deflector voltages to steer the electron beam through the monochromator and the analyzer and finally to the channel electron multiplier. It was found that the energy distribution at the electron source is one of the most important variables for achieving good resolution and it might change each time when the filament was turned on.

In the extended-range ELS experiments, the typical energy resolution varied between 20-50 meV depending on the tuning and the surface conditions. This resolution was adequate for detecting most electronic transitions and plasmon excitations, because the peaks corresponding to these excitations are normally very broad. The typical count rate was about 300 kC/s for the elastic peak, with a background noise level at ~10 C/s. The problem of working in the constant-resolution mode in the extended-range ELS experiment was the change in the transmission function during scanning. In order to maintain a constant pass energy, an input lens is required to vary the acceleration/deceleration ratio correspondingly, which affects the transmission function of the input lens and hence the transmission function of the overall spectrometer. This problem is especially severe when scanning the incident beam energy over a large dynamic range. This problem could, however, be worked around by: (1) using a higher pass energy to reduce the relative changes in the retardation ratio, (2) using a higher potential for the input lens so that the voltage change of the floating elements during scanning with respect to that of the input lens is less severe, and (3) calibrating the spectrum by comparing it with the well-known spectrum of a standard surface to affirm that the variation in the transmission function is smooth and monotonic.

---

* It should be noted that an external mu metal shielding and a Helmhotz cage were used to reduce the Earth's magnetic field to less than 20 mGauss at the sample region (Ref. 1).

Reproduced with permission of the copyright owner. Further reproduction prohibited without permission.

2.4 Temperature programmed desorption experiments

TPD was used to obtain desorption profiles of chemisorbed and entrapped species resulting from surface reactions and ion irradiation. Since entrapped species usually were buried underneath the surface, they could not be detected in a HREELS experiment, but could be identified by TPD. During the TPD experiments, the front face of the crystal was positioned less than 0.5 mm from an orifice that provided the only entrance to a differentially pumped chamber that housed the QMS. Such an arrangement was found to be effective in lowering the background and preventing desorbed species in the surroundings from entering the ionizer region. The temperature was varied at a linear heating rate of 1-2 K/s with a precision better than ±2 K. The temperature control was realized by a custom-built proportional-integral-differential (PID) temperature controller based on the TMS320c50 microprocessor, which was used to provide control for different PID cycles and communication with a personal computer-based data acquisition program designed for the TPD experiment. Figure 2.4 shows a typical thermal desorption profile and demonstrates the linearity of the temperature ramping curve obtained with the setup for an Ar^+-sputtered Si(111)7×7 surface (at 1 K/s).

2.5 LEED and AES Experiments

In the present work, LEED was used to assure the long-range order of the surface while AES was mainly used to determine the contamination level of the surface region. The electron beam energy used in the LEED experiments was typically 30-100 eV with 0.05 mA emission current. The sample was positioned about 4 cm away from the LEED optics. Within this energy range and emission current, surface damage due to the electron beam was usually not detectable, though the electron beam could induce desorption and surface reactions of the adsorbates [13]. The AES was performed by using the 4-grid retarding-field LEED optics as a retarding field analyzer [14,15]. The LEED optics served as a high-pass energy filter, and together with a lock-in amplifier operating in second derivative mode a differential energy distribution dN(E)/dE could be obtained. The sensitivity of this kind of AES setup is somewhat limited and can only be used to determine a relatively high concentration of contamination. A typical impact energy used for our AES analysis was 2.5

Reproduced with permission of the copyright owner. Further reproduction prohibited without permission.

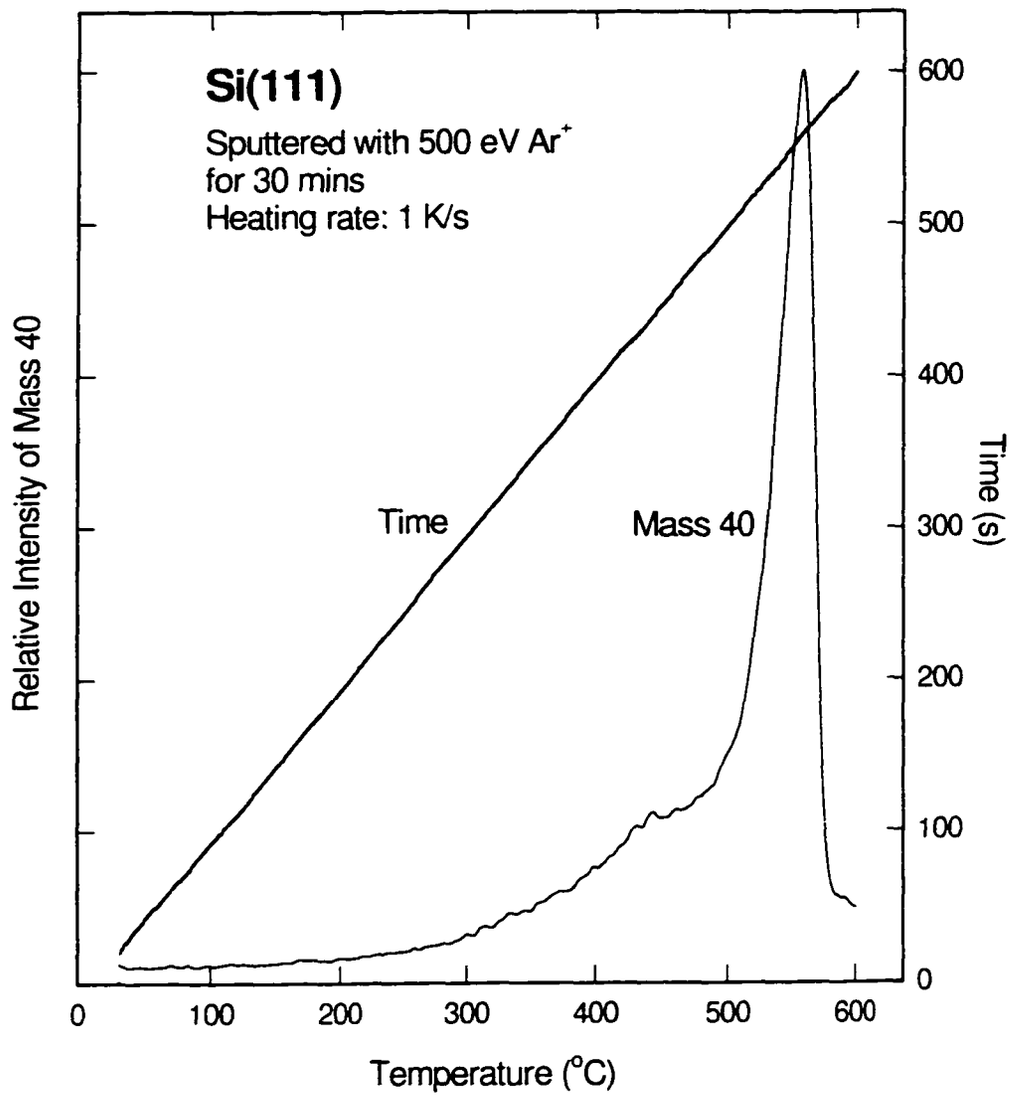

Figure 2.4 Thermal desorption profile of mass 40 (Ar^+) for Si(111)7×7 sputtered by 500 eV Ar^+ for 30 minutes at 3×10^{-5} Torr and its corresponding PID controlled temperature ramping curve.

Reproduced with permission of the copyright owner. Further reproduction prohibited without permission.

- 3 keV at 0.05 mA emission current. At this impact energy, the electron beam could cause significant changes to the adsorbates and the surface, and could lead to other impurity deposition [16]. AES was therefore not used regularly for the composition analysis of the surface in our experiments and was only used when necessary to confirm the cleanliness of the sample during sample preparation.

2.6 References

[1] D. Q. Hu, Ph.D. Thesis, University of Waterloo, Waterloo (1993).

[2] H. Yu, D. Q. Hu, and K. T. Leung, J. Vac. Sci. Technol. A **15**, 2653 (1997).

[3] "Eight Peak Index of Mass Spectra", Vol. **1**, Mass Spectrometry Data Center, Aldermaston (1974).

[4] H. Ibach, "Electron Energy Loss Spectrometers", Springer Ser. Opt. Sci.,Vol. **63**, Springer-Verlag, New York (1991). Also: H. Ibach and D. L. Mills, "Electron Energy Loss Spectroscopy and Surface Vibrations", Academic, New York (1982).

[5] H. Ibach, J. Electron Spectrosc. and Relat. Phenom. **64/65**, 819 (1993).

[6] E. Harting and F. H. Read, "Electrostatic Lens", Elsevier, New York (1976).

[7] Y. Ballu, "Applied Charged Particle Optics – Advances in Electronics and Physics Suppl. 13B", A. Septier (ed.), Academic, New York (1980).

[8] S.D. Kevan, Rev. Sci. Instrum. **54**, 1441 (1983).

[9] S. Andersson, Surf. Sci. **89**, 477 (1979).

[10] S. Andersson and B. N. J. Persson, Phys. Rev. Lett. **45**, 1421 (1980); Phys. Rev. B **24**, 3659 (1981).

[11] B. A. Sexton, Chem. Phys. Lett. **63**, 451 (1979).

[12] A. Spitzer and H. Luth, Surf. Sci. **102**, 29 (1981).

[13] G. Ertl and J. Kuppers, "Low Energy Electron and Surface Chemistr", VCH, Weinheim (1985).

[14] P. W. Palmberg and T. N. Rhodin, J. Appl. Phys. **39**, 2425 (1969).

[15] J. C. Riviere, "Surface Analytical Techniques", Clarendon, Oxford (1990).

[16] H. Ibach, N. D. Bruchmann, and H. Wagner, Appl. Phys. A **29**, 113 (1982).

Reproduced with permission of the copyright owner. Further reproduction prohibited without permission.

Chapter 3

"ANOMALOUS" STABILIZATION OF CO ON Cu(100) AT ROOM TEMPERATURE INDUCED BY LOW-ENERGY ELECTRON AND ION IRRADIATION

3.1 Introduction

CO adsorption on a transition metal surface (e.g., Ni, Pd, and Pt) has been studied extensively in the past three decades [1] and has served as a popular model system in surface science. Compared with the transition metal surfaces, Cu(100) is less reactive stable and the corresponding chemisorption on Cu(100) is considerably weaker (15-20 kcal/mole) [2]. Previous studies [2,3,4] showed that CO adsorbs on the atop site of the Cu(100) surface with a c(2×2) LEED structure [5] at low temperature (<200 K). Furthermore, the literature frequencies for both Cu–CO stretch [or ν(Cu–CO)] at 342 cm^{-1} and C–O stretch [or ν(C–O)] at 2089 cm^{-1} were found to be nearly independent of the coverage. The commonly accepted bonding model is obtained from metal-carbonyl chemistry and it involves the interplay between the dative σ donation from CO to a substrate metal atom and back-donation from the d orbitals of the metal atom to the 2π* orbital of CO [6,7,8]. This model is illustrated in Figure 3.1. To date, no CO has ever been found to adsorb on a clean or oxidized Cu(100) surface at room temperature (RT), although the adsorption of molecules containing the CO functional group, such as alkoxides, on Cu(100) above RT has been reported by Sexton [9]. Below we report adsorption of CO on Cu(100) surface at RT induced by low energy electron or ion irradiation for first time.

The use a of low-energy electron or ion beam has become an increasingly powerful tool for the development of new materials [10]. In particular, electron or ion irradiation has been used to produce reactive ions and free radicals on surfaces and to provide new synthetic routes involving gas-surface reactions instead of thermal chemistry. For example, atomic nitrogen could be obtained by using electron dissociation of N_2 and was found to adsorb on Cu(100) at RT [11]. Since many important aspects about reactions induced by low-energy electron or ion irradiation remain unknown, it would therefore be of practical

Reproduced with permission of the copyright owner. Further reproduction prohibited without permission.

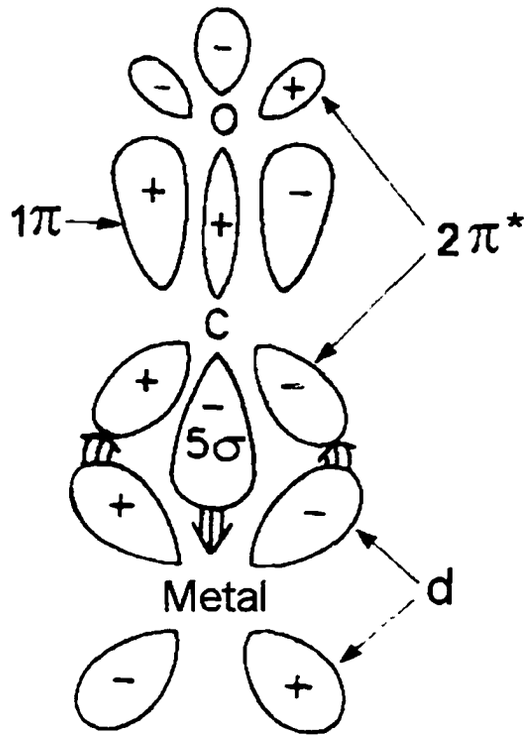

Figure 3.1 Bonding model for CO chemisorbed on a metal surface.

interest to investigate the fundamental mechanisms that control the initial adsorption and subsequent surface reactions induced by electron or ion irradiation.

In the present work, we study these electron or ion-irradiation induced effects for the aforementioned model chemisorption system, CO/Cu(100). In particular, we investigate the adsorption properties induced by low-energy electron or ion irradiation for CO on clean, oxygen-precovered, and carbon-precovered surfaces of Cu(100) by using HREELS, TPD, and AES. We show that "stabilized" CO adsorption can be obtained at RT by using low-energy electron or ion irradiation of CO on clean Cu(100) or of ethylene (C_2H_4) on Cu(100) with pre- or post-exposure of O_2. The "stabilized" CO adsorption is characterized by an "anomalous" red shift of 73 cm^{-1} in the ν(C–O) stretching frequency obtained at low temperature, and is found to be stable to as high as 420 K. By examining the effects generated by different conditions of electron or ion irradiation and the plausible mechanisms

Reproduced with permission of the copyright owner. Further reproduction prohibited without permission.

of coadsorption, we propose a direct-interaction model involving an O–CO complex, in order to explain the observed red shift in ν(C–O) and the unusual stabilization effects of CO/Cu(100) at RT.

3.2 Stabilization of CO/Cu(100) induced by low-energy electron irradiation

In Figure 3.2, we show the effects of low-energy electron irradiation on CO/Cu(100). In particular, a typical vibrational EELS spectrum for 100 L of CO on Cu(100) at 120 K is shown in Figure 3.2a. The characteristic peaks for ν(Cu–CO) at 338 cm^{-1} and ν(C–O) at 2084 cm^{-1} were found to be in good accord with the previously published data [2,3,4]. The c(2×2)CO/Cu(100) sample was then irradiated with electrons (thermionically emitted from a heated tungsten filament positioned 40 mm away at a typical flux of 2.7 $\mu A/mm^2$) at 100 eV impact energy (IE) for 10 minutes. After the electron irradiation, the c(2×2) LEED pattern was found to become less sharp, and the corresponding AES analysis revealed no discernible change in the small intensities of the C and O KLL Auger peaks at 272 eV and 503 eV, respectively. The ν(C–O) peak for the electron-irradiated sample remained at the same energy loss position (Figure 3.2b) but with a reduction in intensity, which was likely the result of electron-induced desorption and dissociation [12]. On the other hand, the corresponding ν(Cu–CO) peak at 338 cm^{-1} became a broad shoulder, which could be attributed to additional contribution from the well-known Cu–O stretch at 305 cm^{-1} as previously observed for c(2×2)O/Cu(100) [13]. When the sample temperature was slowly increased from 120 K, the peak at 2084 cm^{-1} was found to gradually diminish (Figure 3.2c) and disappear at 200 K (Figure 3.2d), revealing the peak at 2011 cm^{-1}. At this point, the LEED pattern became a diffused 1×1. The observed intensity reduction of the ν(C–O) peak at 2084 cm^{-1} with increasing temperature was consistent with the previous work [3]. The new feature at 2011 cm^{-1} was clearly the result of low-energy electron irradiation and could be tentatively attributed to a "perturbed" C–O stretch [i.e., a red-shifted ν(C–O)]. After the electron-irradiated sample was annealed to 160 K, the broad shoulder at ~338 cm^{-1} became a single peak at 310 cm^{-1}, which could be assigned to the Cu–O stretch [13], indicating the presence of atomic oxygen on the surface. The intensity of the peak at 2011 cm^{-1} remained essentially unchanged upon annealing to 370 K (Figure 3.2e) and then decreased almost

Reproduced with permission of the copyright owner. Further reproduction prohibited without permission.

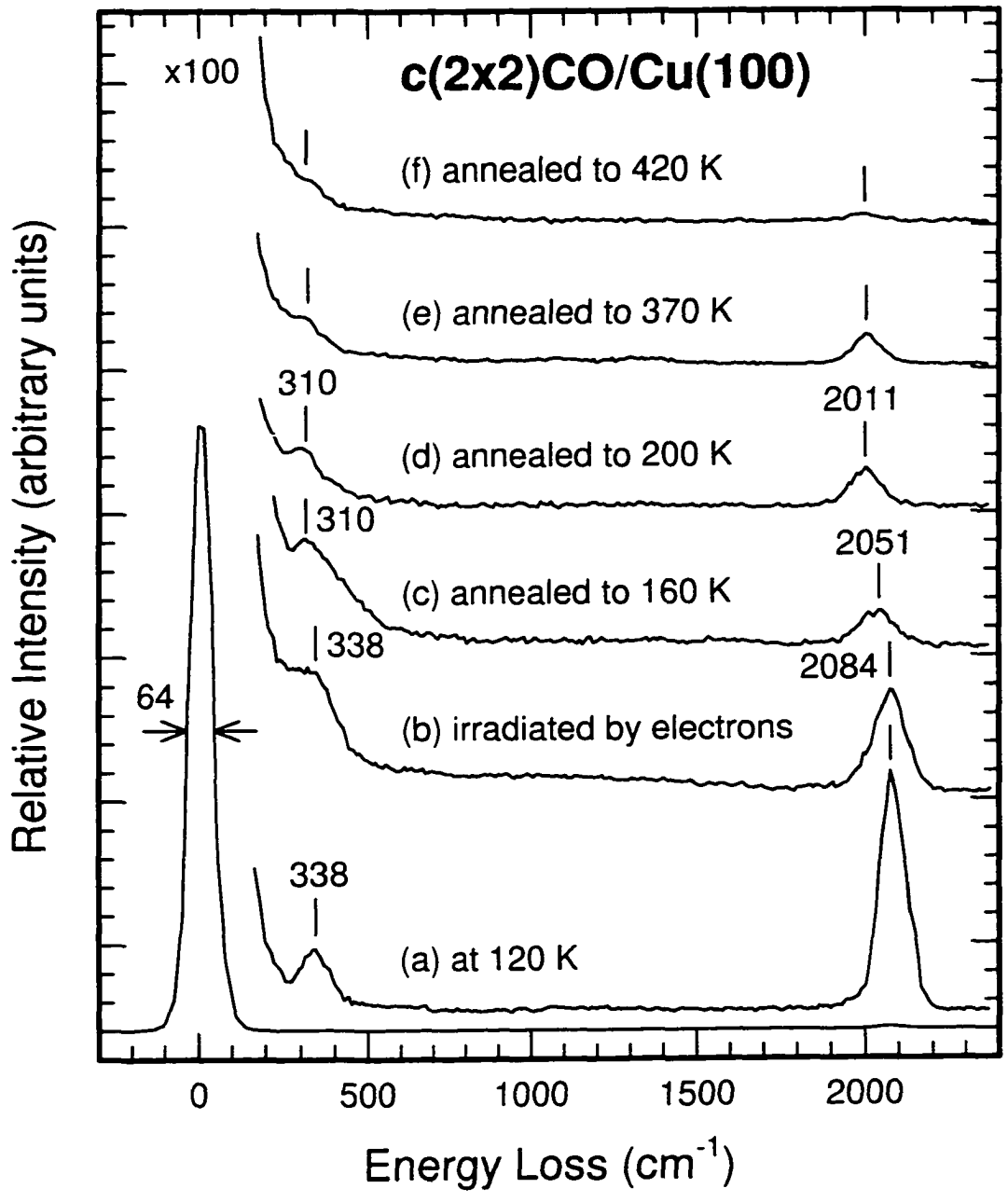

Figure 3.2 Vibrational electron energy loss spectra for (a) 100 L of CO adsorbed on Cu(100) at 120 K, and (b) sample (a) irradiated with electrons at 100 eV and 2.7 $\mu A/mm^2$ for 10 minutes at 120 K, followed by annealing to (c) 160 K, (d) 200 K, (e) 370 K, and (f) 420 K.

Reproduced with permission of the copyright owner. Further reproduction prohibited without permission.

completely upon further annealing to 420 K (Figure 3.2f). In contrast, the peak at 310 cm^{-1} diminished in intensity gradually upon annealing from 160 K (Figure 3.2c) to 420 K (Figure 3.2f).

Additional experiments to further elucidate the nature of this red-shifted ν(C–O) peak give the following results: (1) Reducing the electron IE from 100 to 40 eV appeared to have no significant effect on the corresponding HREELS spectra, which indicates that an electron IE of 40 eV was sufficient to activate the surface reactions that generated the "stabilized" CO. (2) Exposing a high dose (1200 L) of CO to an amorphous Cu surface (obtained by sputtering Cu(100) in 2×10^{-5} Torr of Ar for 20 minutes at 500 eV IE) at 120 K and then annealing it to RT without electron irradiation did not produce the red-shifted CO peak (at 2011 cm^{-1}). Since Ar^+ sputtering is believed to introduce defect sites on Cu(100), this observation indicates that the presence of "stabilized" CO was not due to adsorption on defect sites. (3) Exposing CO to an oxygen-covered Cu(100) surface (which was prepared by exposing a clean Cu(100) surface at RT with different dosages of O_2 ranging from 0.5 to 300 L) at 120 K without electron irradiation and then annealing the resulting sample to RT did not generate the red-shifted CO peak. This result indicates that without electron irradiation CO could neither adsorb on an "oxidized" Cu(100) surface nor coadsorb with surface oxygen atoms to produce the "stabilized" CO. Finally, (4) exposing CO to a carbon-covered Cu(100) surface (obtained by sputtering Cu(100) in C_2H_4 at RT and then annealing to 600 K) at 120 K without electron irradiation and then annealing the resulting sample to RT also did not produce the red-shifted CO peak. This observation suggests that the red-shifted CO peak was not caused by coadsorption of CO with the surface carbon.

All these experiments suggest that the observed red-shifted peak at RT was due to "stabilized" CO species that were generated in-situ during CO exposure by electron irradiation. We believe that irradiation by low-energy electrons alone has only minor effects on the surface itself. Indeed, no change in the (1×1) LEED pattern of a clean Cu(100) surface was observed for an extended period of irradiation with electrons below 100 eV. With electron irradiation at a higher IE (500 eV), the change in the sharpness of the LEED pattern of the resulting sample was also not readily discernible, which suggests that electron irradiation even at this high energy did not significantly roughen the surface. The presence

Reproduced with permission of the copyright owner. Further reproduction prohibited without permission.

of "stabilized" CO generated at the lower electron IE was therefore not due to adsorption on defect sites. Furthermore, despite the red shift of 73 cm^{-1} from its nominal low-temperature position at 2084 cm^{-1}, the vibrational peak at 2011 cm^{-1} could only be assigned to the stretch frequency of a triply bonded C–O on an atop site, because adsorption of a doubly bonded CO at a bridge site [14] (or a four-fold hollow site) would give rise to a vibration at a considerably lower frequency.

3.3 Ion irradiation of Cu(100) in CO at RT

The RT adsorption of CO on Cu(100) could also be obtained by low-energy ion irradiation of Cu(100) in CO at RT. The un-mass-selected ions were produced by turning on the ion gun in 1×10^{-6} Torr of ambient CO atmosphere. The ion composition consists mostly of CO^+ with a small amount of C^+ and O^+ according to its cracking pattern [15]. When CO^+ impacted on the surface, it could undergo further dissociation into atomic C and O. Figure 3.3a shows the presence of the ν(C–O) peak at 2011 cm^{-1} for a Cu(100) surface sputtered at RT in 1×10^{-6} Torr of CO for 10 minutes at an ion IE of 200 eV. A diffuse (1×1) LEED pattern was observed for the resulting sample. Furthermore, the red-shifted CO peak became more intense as the sample was annealed from RT (Figure 3.3a) to 370 K (Figure 3.3b). It became weaker upon further annealing to 400 K (Figure 3.3c) and finally disappeared at 430 K (Figure 3.3d).

The corresponding TPD profiles show that the desorption maxima for mass 28 (corresponding to CO, in Figure 3.4) and mass 44 (corresponding to CO_2, in Figure 3.4b) occurred near 400 K. The temperature of the desorption maximum observed in the TPD experiment (Figure 3.4a) is therefore consistent with the HREELS results (Figure 3.3). In addition to the presence of CO, the presence of CO_2 can be explained by the CO oxidation reaction with surface oxygen [i.e., CO (ad.) + O (ad.) $\rightarrow$ CO_2 (gas)]. In comparison with the results of the electron irradiation experiment (Section 3.2), the adsorption feature obtained by ion irradiation in CO was found to have the same vibrational frequency (2011 cm^{-1}) and desorption maximum (400 K). These similarities strongly suggest that both electron irradiation and ion irradiation in CO generated the same kind of "stabilized" CO adsorption.

Reproduced with permission of the copyright owner. Further reproduction prohibited without permission.

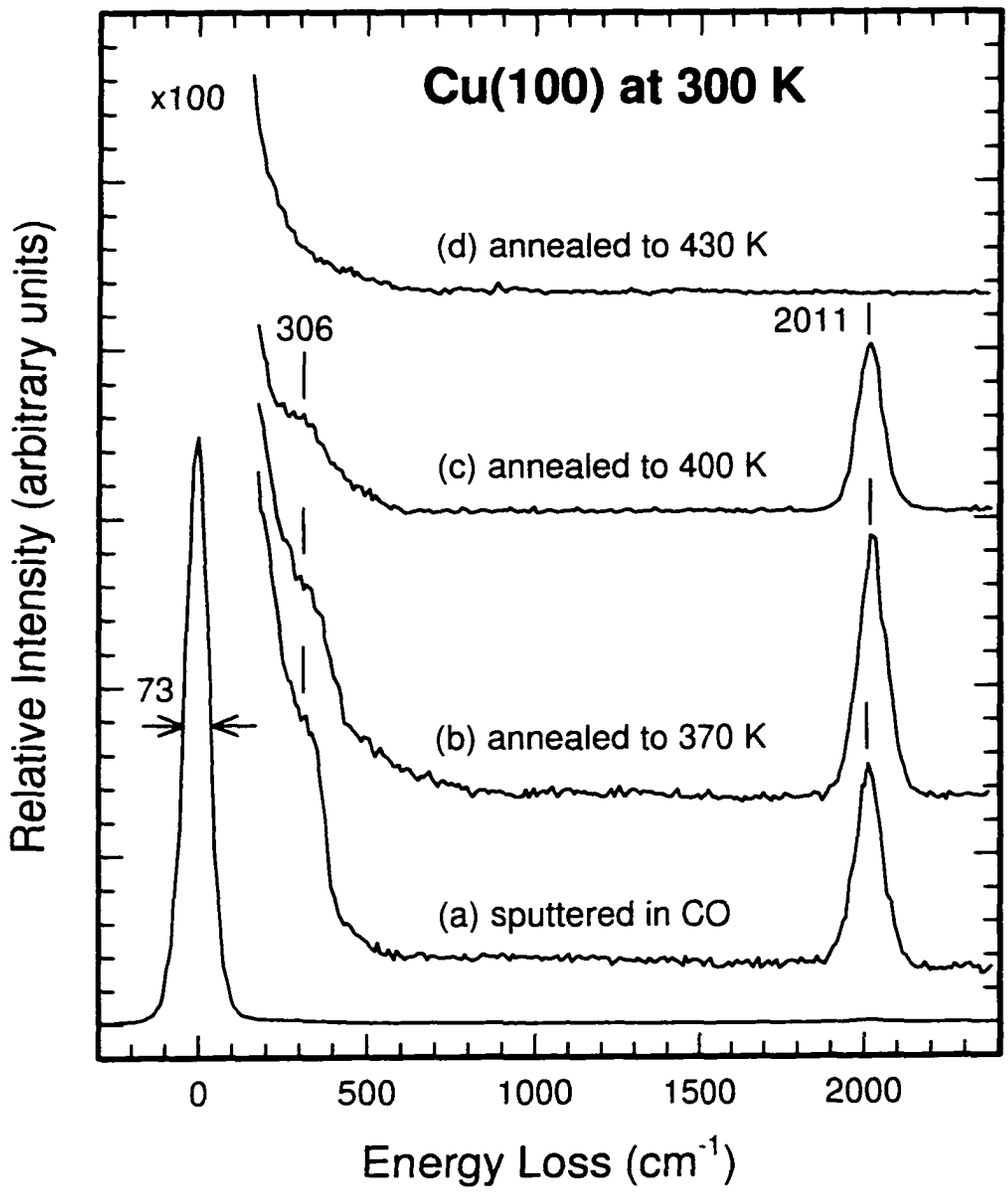

Figure 3.3 Vibrational electron energy loss spectra for (a) Cu(100) sputtered in 1×10^{-6} Torr of CO at 200 eV and 10 nA/mm^2 for 10 minutes at 300 K, followed by annealing to (b) 370 K, (c) 400 K, and (d) 430 K.

Reproduced with permission of the copyright owner. Further reproduction prohibited without permission.

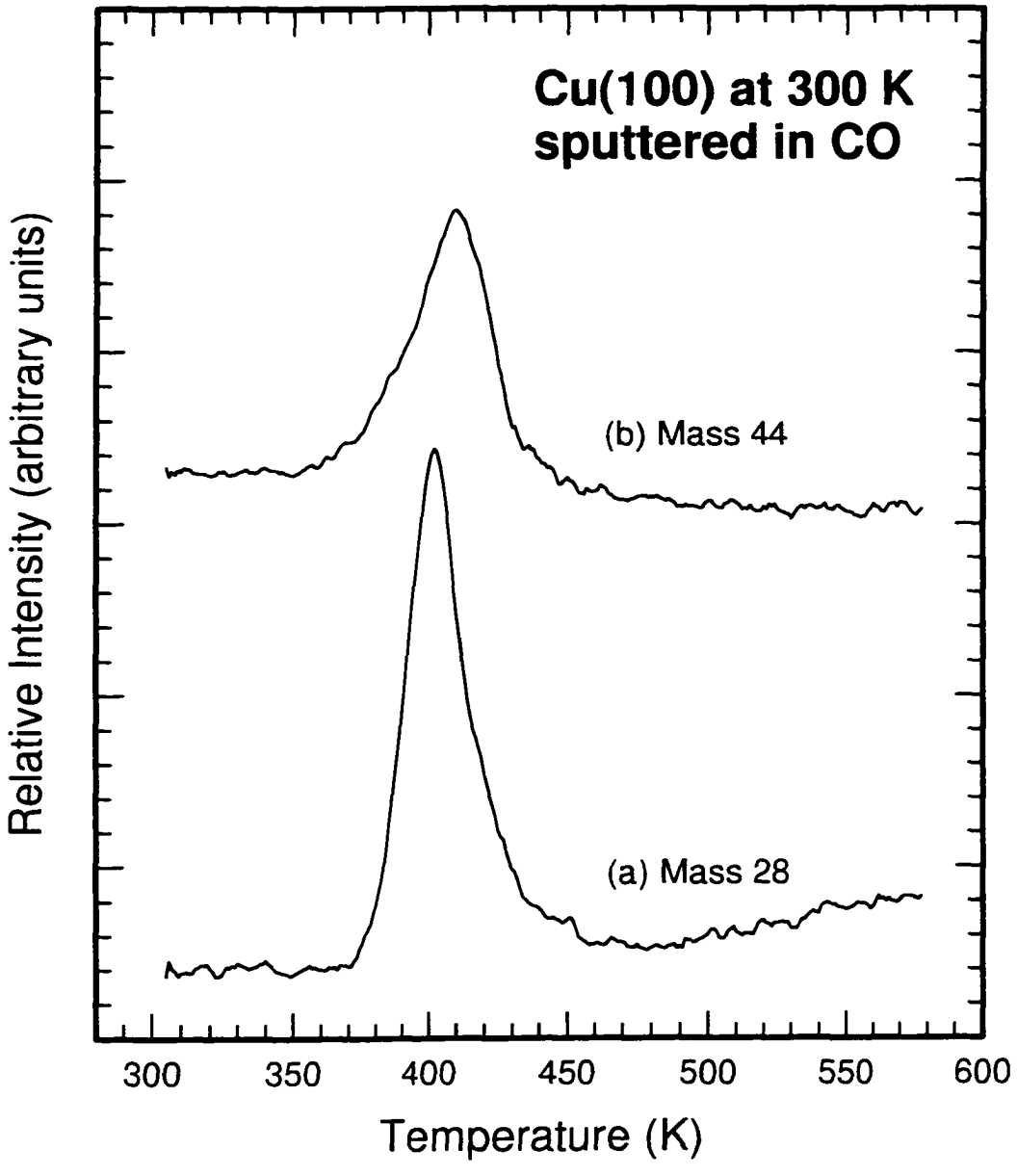

Figure 3.4 Temperature programmed desorption profiles of (a) mass 28 and (b) mass 44 for Cu(100) sputtered in 1×10^{-6} Torr of CO at 200 eV and 10 nA/mm^2 for 10 minutes at 300 K. The linear heating rate was 1 K/s.

Reproduced with permission of the copyright owner. Further reproduction prohibited without permission.

Figure 3.5 compares the AES spectra for Cu(100) irradiated by CO ions at RT (Figure 3.5c) followed by annealing to 530 K (Figure 3.5d) with those for a clean surface at RT (Figure 3.5b) and at 730 K (Figure 3.5a) as well as for CO adsorbed on Cu(100) at 100 K (Figure 3.5e). It should be noted that the features between 95 and 200 eV are caused by surface diffraction and are not real Auger features [16]. These features become less intense when the surface is roughened (Figure 3.5c) or when the temperature is high (Figure 3.5a). The AES spectrum in Figure 3.5c also reveals the presence of C and O on the surface after ion irradiation and the corresponding intensities are stronger than those in the low-temperature CO adsorption case (Figure 3.5e). It should be noted that during the Auger experiment for the low-temperature CO adsorption, CO could be dissociated or desorbed by the 2.5 keV electron beam (as discussed in the previous section), which could in turn lead to "stabilized" CO adsorption on the surface. Furthermore, the c(2×2) LEED pattern disappeared after the Auger experiment, consistent with the destructive effects of the high-energy incident electron beam. After annealing the sample in Figure 3.5c to 530 K (Figure 3.5d), the O peak disappeared and only a residual C feature remained, which suggests that oxygen reacted with the surrounding C atoms and desorbed from the surface in the form of CO or CO_2. This observation is also consistent with our previous HREELS and TPD results.

Along with the reaction activation process, additional effects due to sputtering and defect-site creation could also be introduced during the ion irradiation process. In general, the rate of radiation damage on the sample depends on many factors, including the kinetic energy and mass of the ion, the substrate temperature, and the nature of the material [17]. Unlike electron irradiation, irradiation with ions at 50 eV was found to be sufficient to cause a diffuse LEED pattern and the intensity of the elastic peak in the HREELS spectrum to decrease significantly, both of which are indicative of radiation damage on the sample. In order to isolate the reaction activation effect from the substrate damage effect, we have repeated the experiments using different ion IEs from 50 to 500 eV. These studies showed that the intensity of the CO peak at 2011 cm^{-1} increased slowly with increasing ion IE. However, when CO was directly exposed to an amorphous surface (obtained by sputtering in 2×10^{-5} Torr of Ar for 10 minutes at 500 eV ion IE) without simultaneous ion irradiation during dosing, the red-shifted CO peak was not observed. Furthermore, exposing

Reproduced with permission of the copyright owner. Further reproduction prohibited without permission.

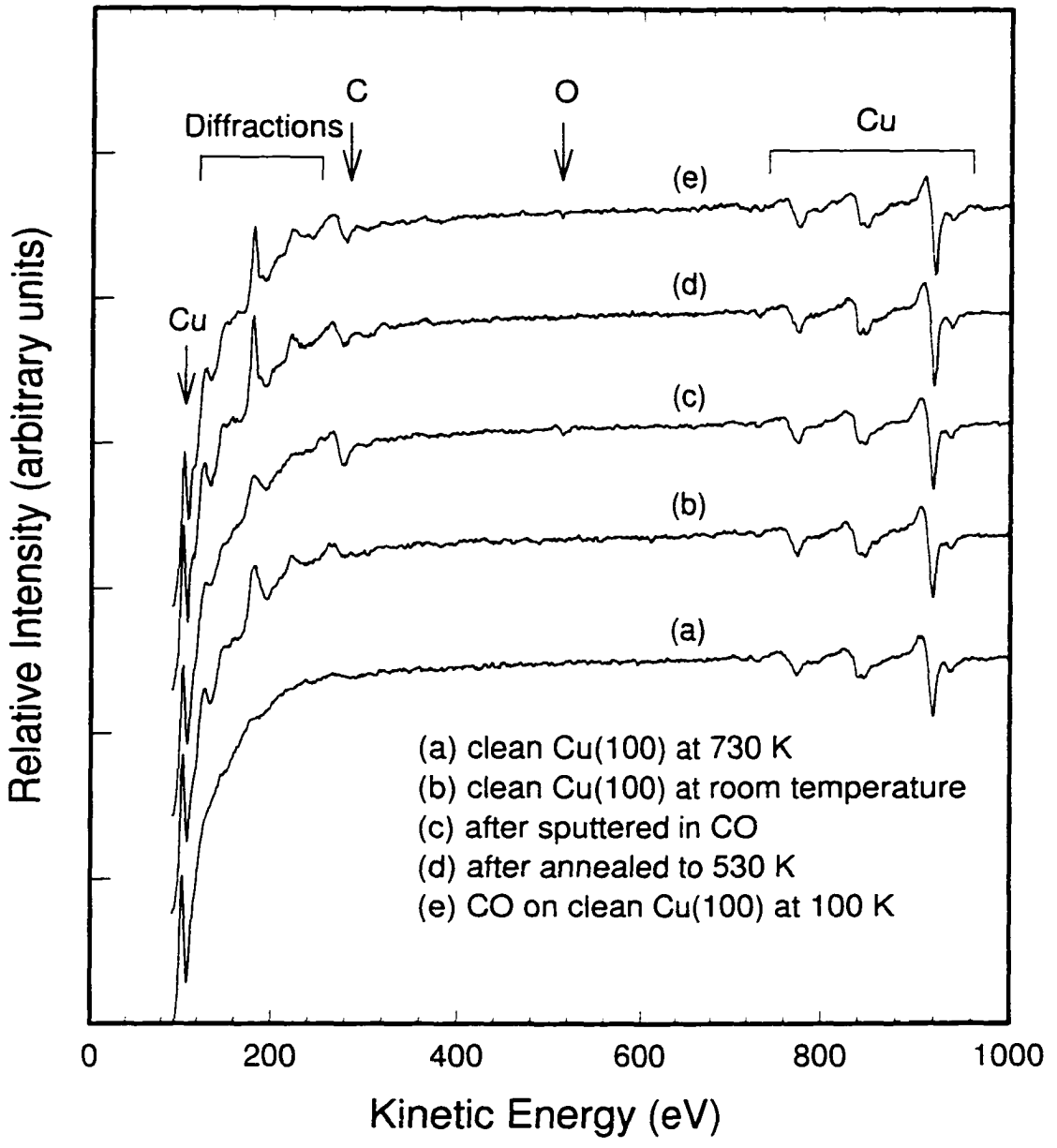

Figure 3.5 Auger electron spectra of clean Cu(100) (a) at 730 K, (b) at room temperature, (c) after sputtered in CO at 200 eV impact energy, and (d) after subsequent annealing to 530 K, and (e) CO/Cu(100) at 100 K. Spectra were taken at 2.5 keV impact energy and 0.05 mA emission current.

Reproduced with permission of the copyright owner. Further reproduction prohibited without permission.

CO at 50 eV ion IE on the amorphous surface did not produce a stronger red-shifted CO peak than that on a clean Cu(100) surface. The red-shifted CO peak could not therefore be attributed to adsorption on defect sites. The slow increase in the intensity of the red-shifted CO peak with increasing ion IE was related to variation in the ion flux caused by changes in the focusing conditions of the ion beam when the IE was varied. On the other hand, increasing the irradiation time from 1 to 10 minutes caused the peak intensity at 2011 cm^{-1} to increase correspondingly. The increase in the peak intensity leveled off upon further increase in the irradiation time from 10 to 30 minutes, indicating the on-set of an equilibrium condition between the reaction rate and the rate of adsorbate removal.

3.4 Ion irradiation of Cu(100) in C_2H_4 with pre- and post-exposure of O_2 at RT

Like CO, C_2H_4 was found to adsorb on Cu(100) only at low temperature [18]. However, our AES results (not shown) indicated the presence of surface carbon after the clean Cu(100) surface was exposed to 600 L of C_2H_4 at RT with ion irradiation at a low ion IE of 50 eV. At a higher dose (5000 L) of C_2H_4 with ion irradiation, our HREELS results, to be presented later in Chapter 5, indicated the adsorption of CH fragments. Based on these exposure studies, we used a relatively low dose (600 L) of C_2H_4 with ion irradiation in order to generate surface carbon to investigate its reaction with atomic oxygen pre-deposited on the surface. It should be noted that an oxygen-covered Cu(100) surface can be obtained by directly dosing O_2 to Cu(100) at RT [13]. Figure 3.6 shows the HREELS spectrum for an O-precovered Cu(100) sample ion-irradiated in 1×10^{-6} Torr of C_2H_4 at 50 eV for 10 minutes at RT. For a 500 L pre-exposure of O_2 to Cu(100) at RT, we found the characteristic ν(Cu–O) peak at 300 cm^{-1} and a c(2×2) LEED pattern, which are consistent with the dissociative adsorption of O_2 observed in the previous work [13]. Evidently, the energy loss peak at 2011 cm^{-1}, characteristic of the previously observed "stabilized" CO adsorption, could again be obtained by ion irradiation of the oxidized sample in C_2H_4 at RT (Figure 3.6b). This peak became more intense as the sample was annealed from RT to 370 K (Figure 3.6c) and then almost completely diminished upon further annealing to 430 K (Figure 3.6d).

Reproduced with permission of the copyright owner. Further reproduction prohibited without permission.

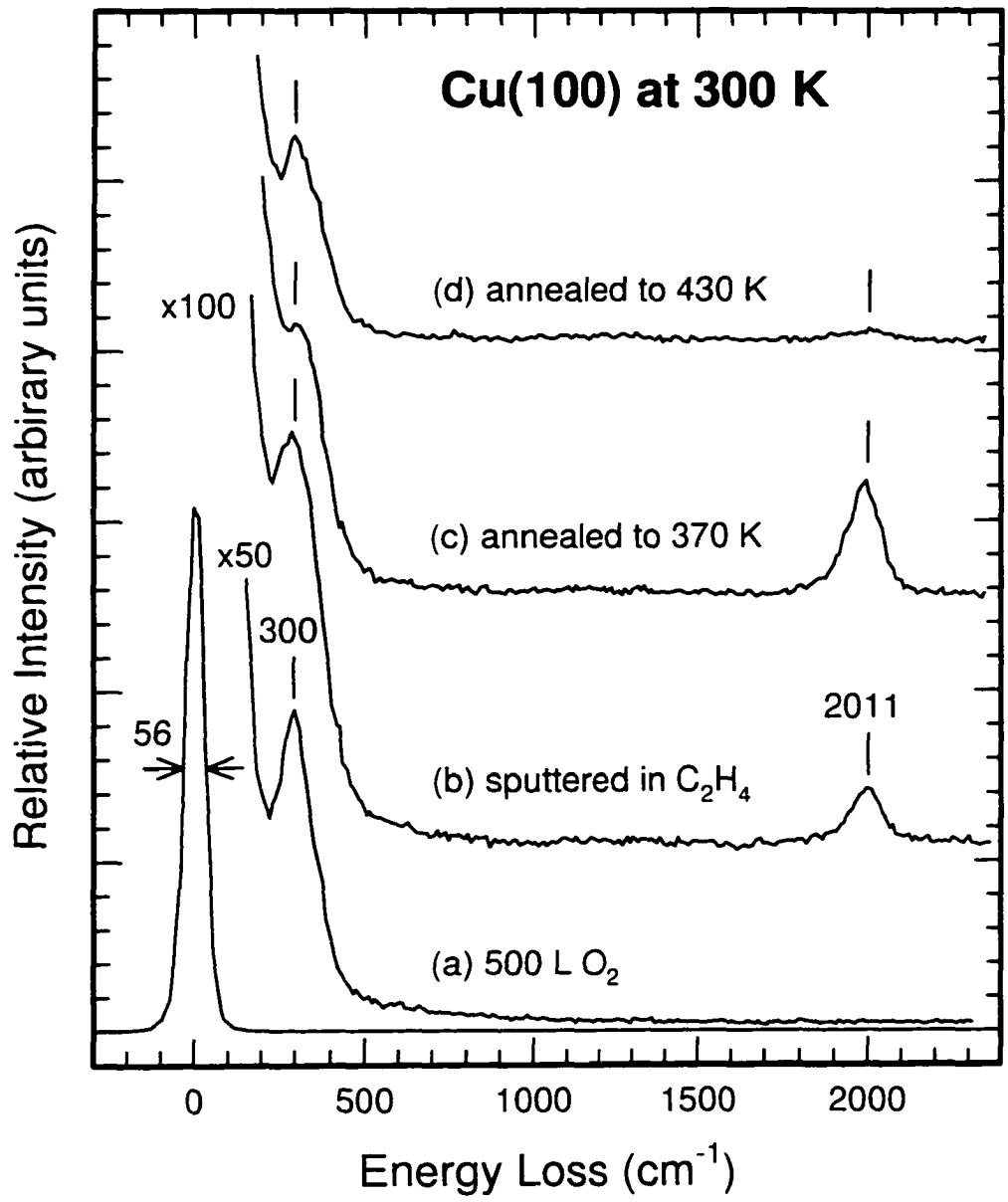

Figure 3.6 Vibrational electron energy loss spectra for (a) Cu(100) exposed with 500 L of O_2 at 300 K, and (b) sample (a) sputtered in 1×10^{-6} Torr of ethylene at 50 eV and 10 nA/mm^2 for 10 minutes, followed by annealing to (c) 370 K, and (d) 430 K.

Reproduced with permission of the copyright owner. Further reproduction prohibited without permission.

In Figure 3.7, we demonstrate that the presence of the red-shifted CO peak did not appear to depend on the order of dosing O_2 and ion irradiation in C_2H_4 (Figure 3.6). Despite the lack of any discernible feature in the HREELS spectrum for a clean Cu(100) surface after ion irradiation in C_2H_4 at 50 eV IE (Figure 3.7a), the corresponding AES result clearly indicated an increase in the surface carbon concentration (see below). After 100 L of O_2 was subsequently exposed to the surface (Figure 3.7b), a prominent ν(Cu–O) peak at 300 cm^{-1} was observed. When the sample was annealed to 370 K (Figure 3.7c), the CO peak at 2011 cm^{-1} reappeared and could again be removed by annealing to 430 K. In keeping with the HREELS results shown in Figure 3.6 and Figure 3.7, the corresponding TPD data (not shown) revealed that maximum desorption of both CO and CO_2 from the surface occurred near 400 K, which is similar to the results shown in Figure 3.4. Apparently, the peak at 2011 cm^{-1} in Figure 3.6 and 3.7 can be attributed to the same "stabilized" CO adsorption observed earlier. On the other hand, if the C-covered surface (Figure 3.7a) was annealed to 500 K first and then followed by O_2 exposure at RT, no red-shifted CO peak was observed even upon annealing the sample to 370 K. This indicates that the presence of surface atomic carbon (and/or C-containing fragments) produced by ion irradiation in C_2H_4 was essential to the formation of the red-shifted CO peak. As the C-covered sample was annealed to 500 K, the carbon atoms either combined with one another to form graphite or diffused into the bulk, preventing the formation of the "stabilized" CO species on Cu(100). Since the deposition of surface carbon was achieved by ion irradiation in the present experiment, the effect of defect sites cannot be ruled out. However, the results of the experiments shown in Sections 3.2 and 3.3 argue against the formation of "stabilized" CO caused by these defect sites.

The corresponding AES spectra for the above experiment (Figure 3.6) are shown in Figure 3.8. Figure 3.8b clearly shows the O Auger peak at 507 eV after a clean Cu(100) (Figure 3.8a) was dosed with 200 L of O_2 at RT. After sputtering the O-pre-deposited sample (Figure 3.8b) in 600 L of ethylene at 50 eV IE (Figure 3.8c), the C Auger peak at 274 eV appeared and the intensity of the O Auger peak was reduced, which might be caused by the partial removal of oxygen due to sputtering and concurrent activated surface reactions. It should be noted that a longer exposure time or higher energy used for

Reproduced with permission of the copyright owner. Further reproduction prohibited without permission.

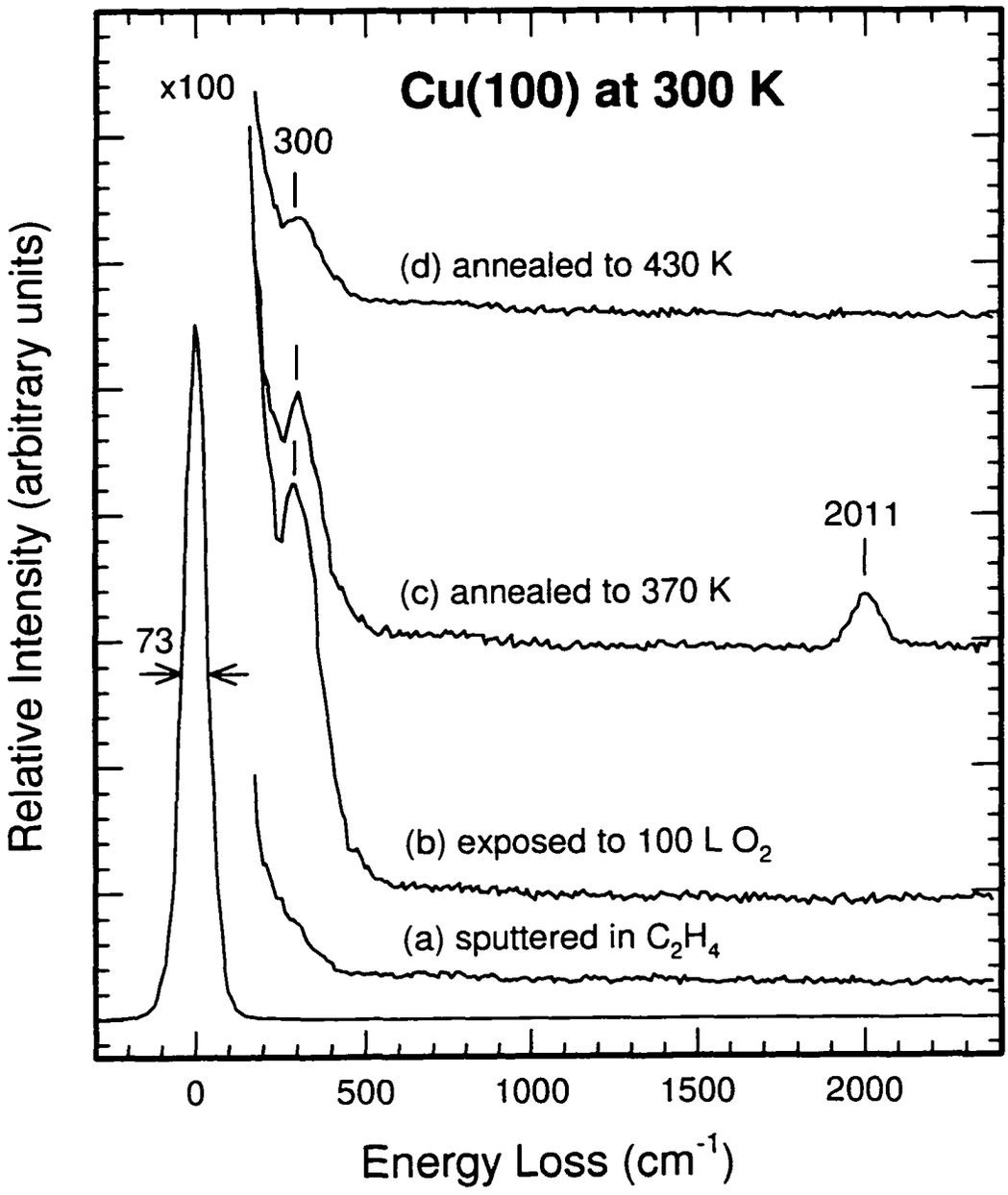

Figure 3.7 Vibrational electron energy loss spectra for (a) Cu(100) sputtered in 1×10^{-6} Torr of ethylene at 50 eV and 10 nA/mm^2 for 10 minutes at 300 K, and (b) sample (a) exposed with 100 L of O_2, followed by annealing to (c) 370 K, and (d) 430 K.

Reproduced with permission of the copyright owner. Further reproduction prohibited without permission.

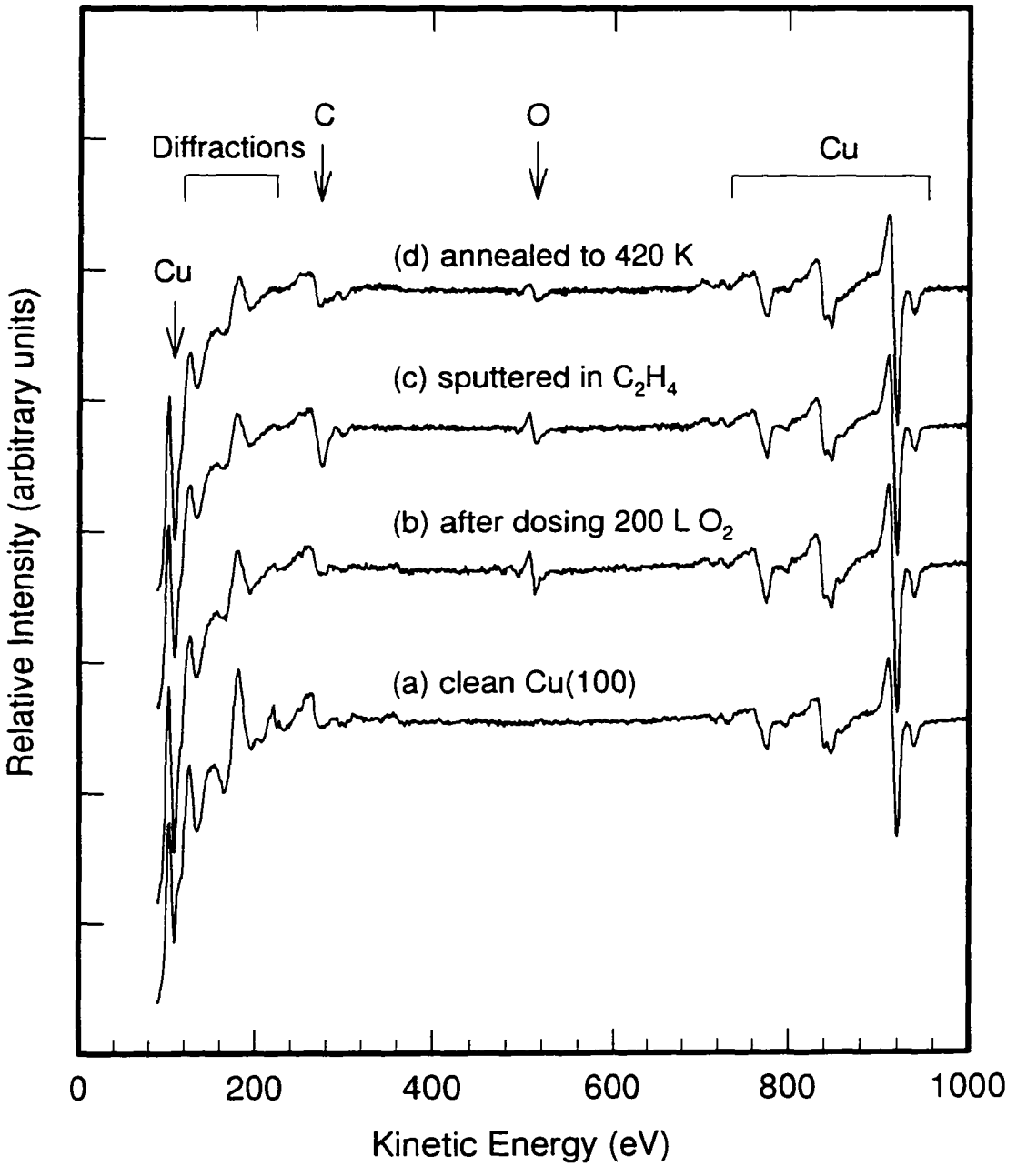

Figure 3.8 Auger electron spectra for (a) clean Cu(100), (b) after dosing 200 L of oxygen at room temperature, followed by (c) sputtering in 600 L of ethylene at 50 eV, and then (d) annealed to 420 K. Spectra were taken at 2.5 keV impact energy and 0.05 mA current.

Reproduced with permission of the copyright owner. Further reproduction prohibited without permission.

sputtering could completely remove the oxygen from the surface. After the sample was further annealed to 420 K, the intensity of the observed carbon peak was significantly reduced (Figure 3.8d), which indicates that reactions involving C and/or C diffusion into the bulk might have occurred during the sample annealing process. The remaining oxygen surface concentration appeared to be larger than that of C, which is consistent with the HREELS result (Figure 3.7d).

3.5 CO stabilization by C-containing species on Cu(100) at RT

In the previous experiments, the ion dosage in ethylene was relatively small (600 L) and the IE of the ethylene ion was also low (50 eV). As a result, the corresponding HREELS features characteristic of the CH fragments were almost undetectable (Figure 3.7a). However, when higher ethylene dosages and IE were used, HREELS features for CH fragments began to appear (see later in Chapter 5 for more detailed discussions of these features), which clearly indicated an increased concentration of C-containing species on the surface. The corresponding stabilized CO, generated in a similar fashion as in Section 3.4, was found to have different stretching frequencies. Figure 3.9 shows the HREELS spectra for a c(2×2)O/Cu(100) sample as a function of ethylene ion dosage. At an ethylene ion dose of 2 kL (where 1 kL is 1000 L), the dominant features are the Cu–O stretch at 306 cm^{-1} and the red-shifted C–O stretch at 2019 cm^{-1} (Figure 3.9a). (It should be noted that in spite of the multiple bond order in CO, we have followed the earlier convention when writing C–O stretch [18], in which CO should not be interpreted as "single-bonded".) The observed red shift in the C–O stretch is the same as what we found in the previous Sections. At a higher ethylene ion dose, the HREELS spectra (Figure 3.9b-d) reveal new hydrocarbon features at 764, 1384 and 2952 cm^{-1} (Chapter 5). Furthermore, in addition to the red-shifted C–O stretch at 2019 cm^{-1}, the peak at 2163 cm^{-1}, which first appeared only as a small shoulder in Figure 3.9a, became more intense with increasing ion dosage.

In order to identify the nature of these peaks, we conducted an isotope substitution experiment using a 2 kL ion dose of C_2D_4. In addition to the features attributed to deuterated hydrocarbon species found in the corresponding Cu(100) case (Chapter 5) and

Reproduced with permission of the copyright owner. Further reproduction prohibited without permission.

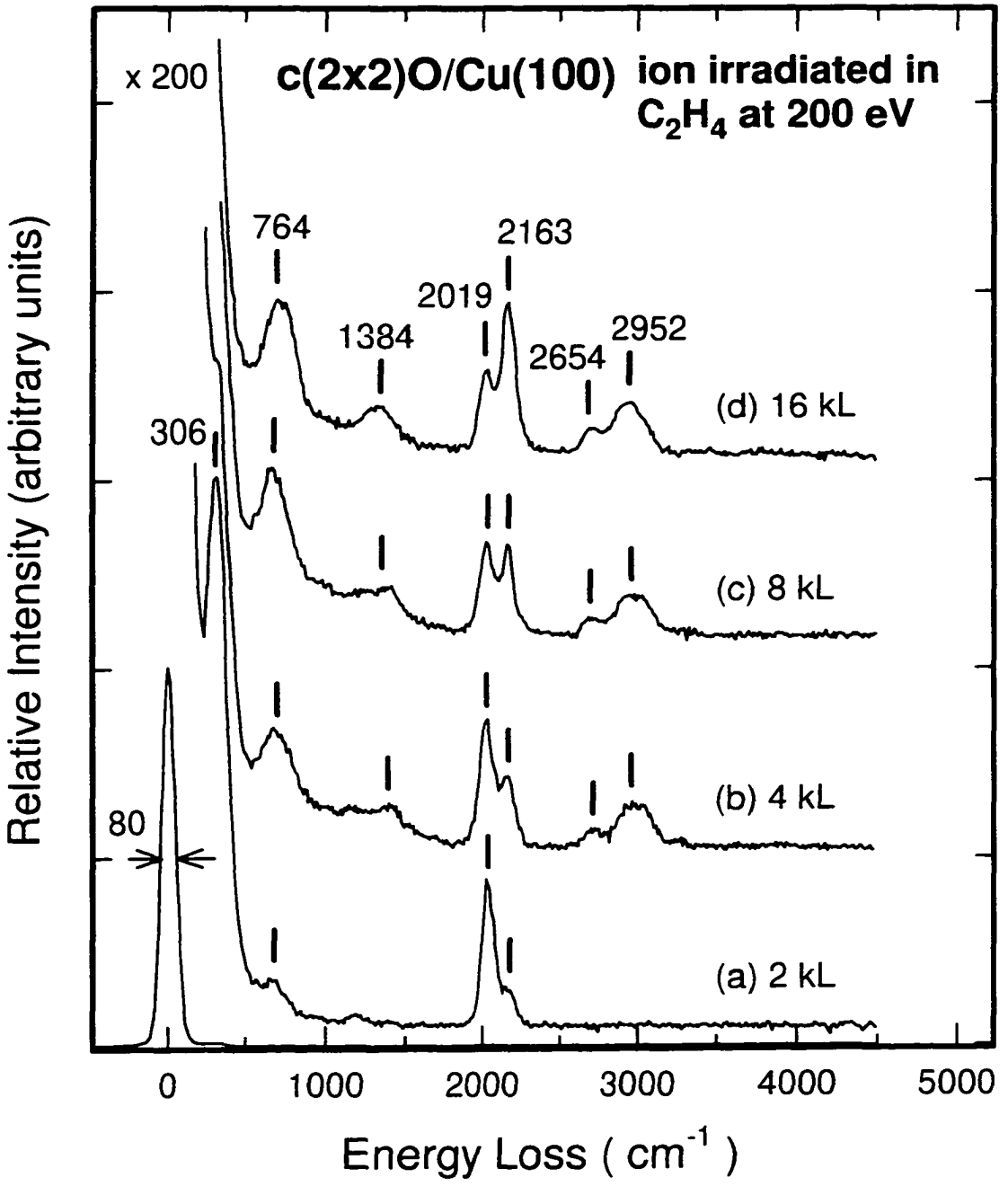

Figure 3.9 Electron energy loss spectra for an oxygen-precovered Cu(100) surface ion-irradiated at 200 eV impact energy in (a) 2 kL, (b) 4 kL, (c) 8 kL, and (d) 16 kL of C_2H_4.

Reproduced with permission of the copyright owner. Further reproduction prohibited without permission.

the red-shifted CO stretch at 2019 cm^{-1}, the corresponding HREELS spectrum shown in Figure 3.10a also indicates the presence of a shoulder at 2163 cm^{-1}. The identical position of this peak to that found in the spectrum for the normal ethylene case (Figure 3.9a) confirms that this peak is not related to vibrations involving H. The feature at 2163 cm^{-1} became more evident after annealing to 380 K (Figure 3.10b). The data obtained with a higher dose of deuterated ethylene ions are not presented here because the peak at 2163 cm^{-1} would be masked by a much stronger peak corresponding to the C–D stretch, which happened to occur at almost the same frequency (see Chapter 5). The feature at 2163 cm^{-1} can therefore only be assigned to the C–O stretch. Further increase in the ethylene ion dosage to 32 kL (not shown) caused a reduction in the intensities of the CO peaks while the peaks corresponding to the hydrocarbon fragments became stronger, which indicates that oxygen and CO were removed from the surface due to sputtering effects in the ion irradiation process.

Figure 3.11 shows the EELS spectra for a c(2×2)O/Cu(100) sample ion-irradiated with 16 kL of ethylene at RT (Figure 3.9d) as a function of annealing temperature. The corresponding coadsorbed hydrocarbon species apparently exhibit energy loss features at 764, 1384 and 2968 cm^{-1} (Figure 3.11a), nearly identical to those found for the Cu(100) case shown in Figure 3.9. The stabilized CO peaks at 2019 cm^{-1} and 2163 cm^{-1} became more intense when the sample was annealed to 330 K (Figure 3.11b) but weakened upon further annealing to a higher temperature (Figure 3.11c-d). The observed temperature dependence is therefore similar to that of the oxygen-stabilized CO peak shown in Figure 3.6. The corresponding TPD result (Figure 3.12) for a sample prepared similarly using a lower dose (8 kL) of deuterated ethylene ions indicates desorption of D_2 (mass 4) and that of CO (mass 28) occurred at 370-650 K and ~420 K, respectively, (similar to Figure 3.4). No other ions (of different masses) were found during the TPD process. These results indicate that different initial surface conditions of a c(2×2)O overlayer did not significantly affect the adsorption structure of the hydrocarbon species deposited subsequently using the ion irradiation technique. Since no direct evidence for the formation of any surface species containing the C=O or C–O functional group was obtained, it appears that surface oxygen only reacted with atomic carbon produced during ion irradiation to form C≡O.

Reproduced with permission of the copyright owner. Further reproduction prohibited without permission.

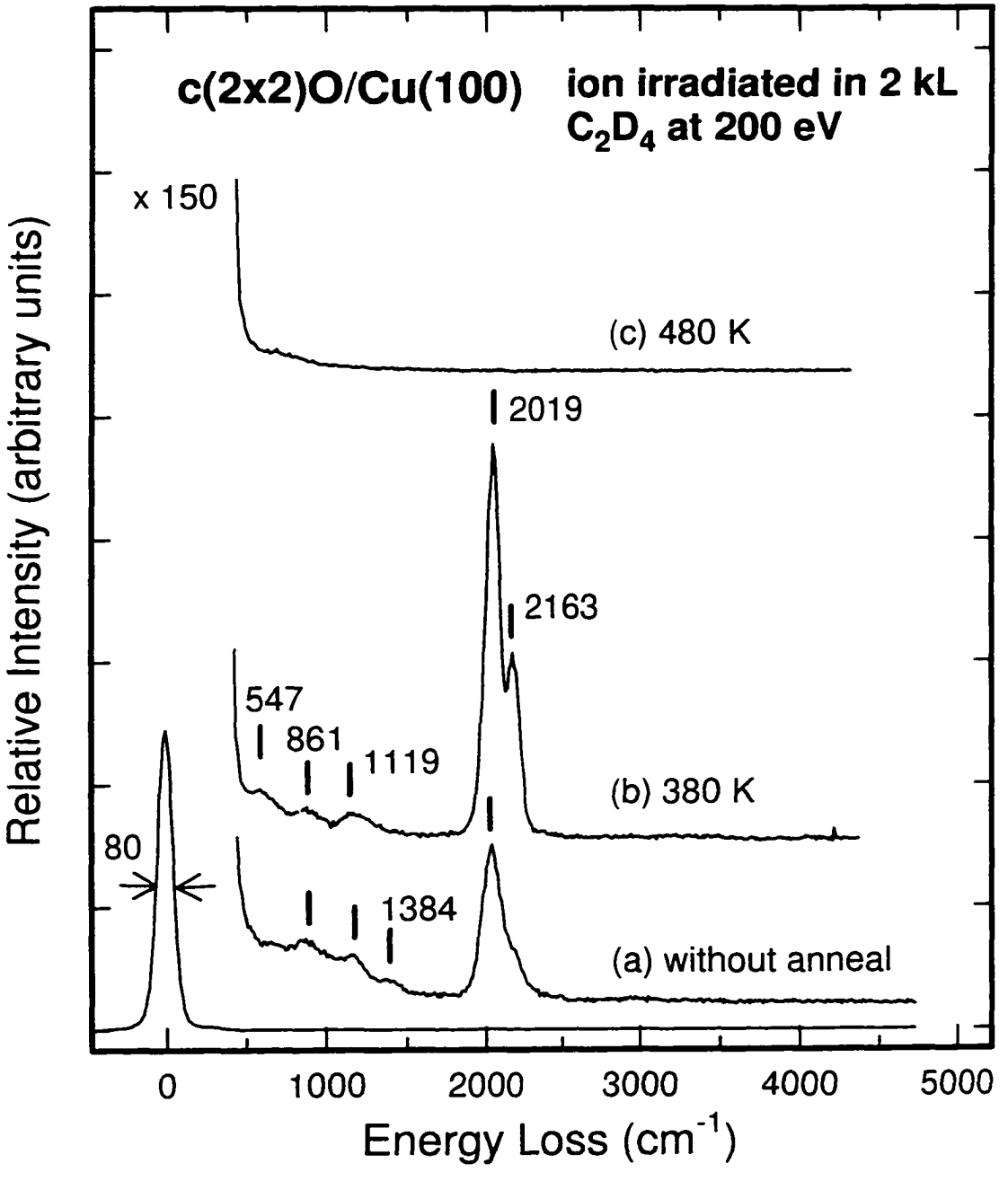

Figure 3.10 Electron energy loss spectra for an oxygen-precovered Cu(100) surface ion-irradiated at 200 eV impact energy in 2 kL of C_2D_4 (a) without and with annealing to (b) 380 K, and (c) 480 K.

Reproduced with permission of the copyright owner. Further reproduction prohibited without permission.

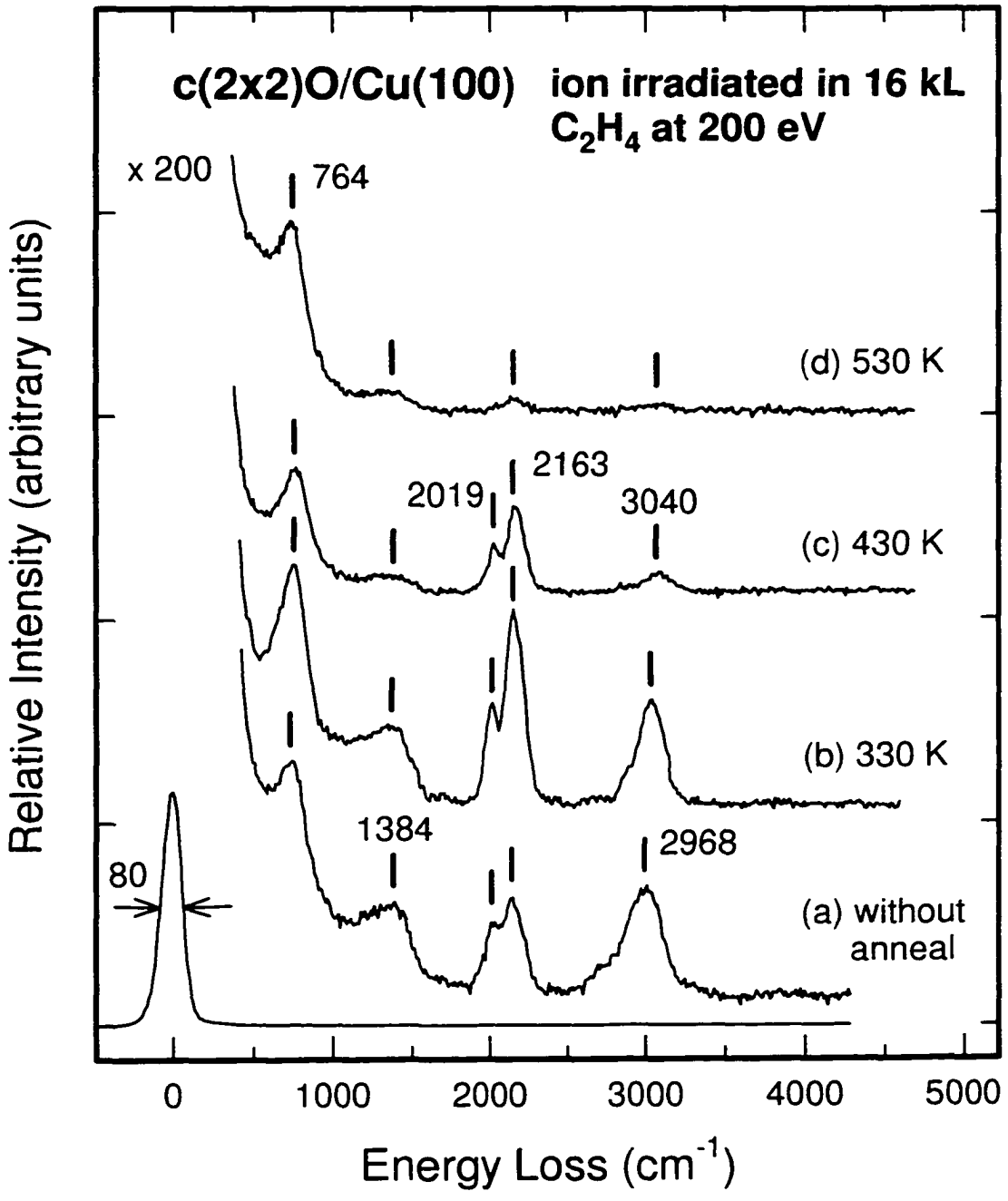

Figure 3.11 Electron energy loss spectra for an oxygen-precovered Cu(100) surface ion-irradiated at 200 eV impact energy in 16 kL of C_2H_4 (a) without and with annealing to (b) 330 K, (c) 430 K, and (d) 530 K.

Reproduced with permission of the copyright owner. Further reproduction prohibited without permission.

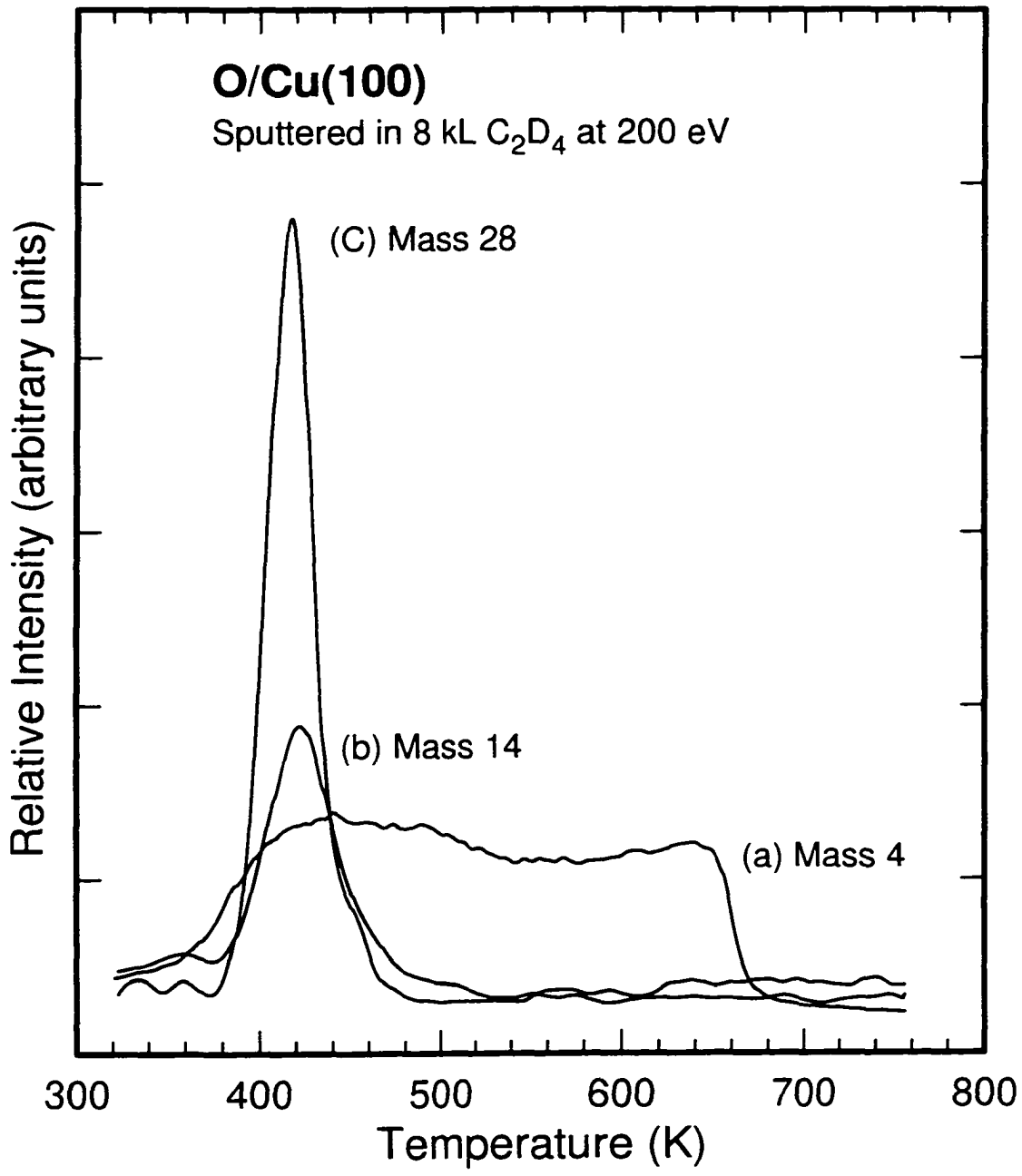

Figure 3.12 Temperature programmed desorption profiles of, (a) mass 4, (b) mass 14, and (c) mass 28 for 500 L O_2 predeposited on Cu(100) followed by sputtering in 8 kL of C_2D_4 at 200 eV.

Reproduced with permission of the copyright owner. Further reproduction prohibited without permission.

3.6 Bonding model for the "stabilized" CO adsorption

It is well known that chemisorption of CO on Cu(100) is extremely weak. To the best of our knowledge, the present work reports the first observation of CO adsorption on Cu(100) at RT. Furthermore, the apparent stabilization of CO at RT is characterized by a red shift of 73 cm^{-1} in the ν(C–O) peak, observed for the adsorption of CO on Cu(100) at low temperature. Although we cannot rule out the defect-site effects, the experiments involving electron irradiation and amorphous surface provide no supporting evidence for the conjecture that the "stabilized" CO adsorption was caused by defect sites. Since CO has not been previously observed on other types of adsorption sites except for the atop site on Cu(100), an adsorption geometry based on terminally bonded CO remains as our favourite choice to account for the observed "stabilized" structure at RT. In particular, the ν(C–O) value for the bridge sites is expected to be considerably lower than 2011 cm^{-1}. For example, a frequency of 1882 cm^{-1} has been attributed to the vibrational feature of a proposed Cu_2CO species that involves a CO molecule bridge-bonded to two Cu atoms [14]. No report for CO adsorbed on a four-fold hollow site of Cu(100) is available in the literature. On the other hand, a red shift of 73 cm^{-1} is too large to be caused by adsorption on different low Miller index planes of Cu, because previous studies have shown that the ν(C–O) frequencies for Cu(111) and Cu(110) could at most differ from that for Cu(100) by 15-24 cm^{-1} [14]. Since a new or additional bonding structure is needed to stabilize CO on the Cu(100) surface, the most likely mechanism is coadsorption. Although no direct evidence is found to support the presence of C (and hence its coadsorption with CO) in the case of low ethylene ion dose (Section 3.4), the coadsorption of CO with O is plausible due to the presence of O on the surface, as indicated by the ν(Cu–O) peak in the HREELS spectrum and by the corresponding TPD profiles (of CO and CO_2).

There have been many studies on the coadsorption of promoters and inhibitors with CO on fcc metal surfaces. In particular, it has been shown that the ν(C–O) frequency can be reduced (red-shifted) by the coadsorption of such promoters as Na [19] and K [20]. On the other hand, the coadsorption of CO with inhibitors, such as O, was found to induce both red and blue shifts in the ν(C–O) frequency [21,22]. There are at least five mechanisms that have been proposed to explain the ν(C–O) frequency shifts induced by coadsorption [23],

Reproduced with permission of the copyright owner. Further reproduction prohibited without permission.

which involve: (1) the indirect surface-mediated interaction, (2) the direct coadsorbate-to-CO interaction, (3) adsorption geometry and related effects, (4) sp^2 rehybridization, and (5) the surface image charge effect. The most popular models involve the indirect and direct interactions. The indirect interaction model is based on electron transfer between the coadsorbate and the $2\pi^*$ antibonding orbital of a neighboring CO molecule through the d orbitals of the metal substrate. In this model, a promoter donates electrons to the metal surface usually through a dative σ bond, which results in an upward shift of the Fermi level and hence increases the electron back-donation from the metal to the $2\pi^*$ orbital of CO. Since the antibonding between the CO molecule and the metal is enhanced, the C–O triple bond is concomitantly weakened, which gives rise to a red shift in the ν(C–O) frequency. However, when CO coadsorbs with an inhibitor that withdraws electrons from the metal surface, the back-donation to the $2\pi^*$ orbital is reduced and the C–O triple bond is strengthened, resulting in a blue shift. In our case, if CO were to coadsorb with O, a blue-shifted ν(C–O) feature would be expected. In the case of the low ethylene ion dose (Section 3.4), the lack of any discernible blue-shifted feature therefore suggests that the surface-mediated interaction does not play a significant role. On the other hand, the overlap between a coadsorbate orbital and the $2\pi^*$ orbital of CO in the direct interaction model would lead to the formation of a coadsorbate-CO quasi-complex. In effect, electron delocalization of the C–O multiple bond density to a coadsorbed O atom causes the C–O bond to weaken, inducing a red shift in the ν(C–O) frequency. In this model, the proposed O–CO quasi-complex can be used to explain the red shift observed in our experiments. In particular, an orbital from O overlaps with the $2\pi^*$ orbital of CO to form a partial bond, which reduces the bond order of CO and gives rise to a red shift in the ν(C–O) frequency. In the case of possible geometry-related effects, an earlier infrared study on the interactions of CO adsorbed on oxygen-precovered Cu(111) and Cu(110) surfaces [22] has revealed a doublet structure near 2110 cm^{-1}, which was proposed to be caused by different bonding sites. In contrast, our studies do not find any change in the ν(C–O) frequency upon different exposures of oxygen and under different ion irradiation conditions, which suggests that the bonding-site effect does not cause the observed frequency shift. Finally, we cannot rule out the contribution due to the electrostatic interaction between the permanent dipole of CO and

Reproduced with permission of the copyright owner. Further reproduction prohibited without permission.

the dipole generated by a coadsorbate and its surface image charge, because of the unknown magnitude of the dipole interaction involved.

Given the observed red shift, we favour a direct-interaction bonding model involving an O–CO quasi-complex. In particular, the unusual stabilization of CO adsorption found in our experiments can be explained by a partial bond between a CO molecule adsorbed on an atop site and a coadsorbed O atom. Furthermore, a calculated potential energy surface for the ground state of CO_2 suggests that a "free" CO_2 molecule dissociates into CO and O at an O-to-CO separation of ~2.2 Å [24]. The proposed direct interaction between CO and O must therefore involve an O-to-CO separation smaller than 2.2 Å. In the commonly accepted terminally-bonded adsorption model for CO on Cu(100) [4], this separation can only be realized if CO is slightly tilted towards the coadsorbed O atom. Since the earlier studies for O on Cu(100) have demonstrated that O adsorbs in a four-fold hollow site [13], a plausible bonding structure therefore involves the stabilization of a terminally bonded CO molecule, slightly tilted at the atop site, by a coadsorbed O atom in a nearest-neighbour four-fold hollow site (Figure 3.13). The lack of any direct evidence for the vibration of the coadsorbed-O-to-CO bond in the HREELS experiments is consistent with the weak dipole intensity of a nearly surface-parallel bond.

Finally, in addition to the coadsorption-induced shift, coupling shift and chemical shift may also occur. In particular, it has been shown that on a clean Cu(111) surface the nearly constant value for the ν(C–O) frequency observed at different CO coverages is a consequence of the interplay between two large but opposing effects: a coupling shift that tends to increase the frequency with increasing coverage and a chemical shift that tends to reduce it [25]. However, the frequency shifts induced by these effects are usually smaller than 40 cm^{-1} individually and even smaller when the two effects are combined together. They are therefore not expected to play an important role for the 73 cm^{-1} red shift found in the present case.

By the same token, we can also propose that the feature observed at 2163 cm^{-1} for the case of high ethylene ion dose (Section 3.5) corresponds to a "perturbed" C–O stretch,

Reproduced with permission of the copyright owner. Further reproduction prohibited without permission.

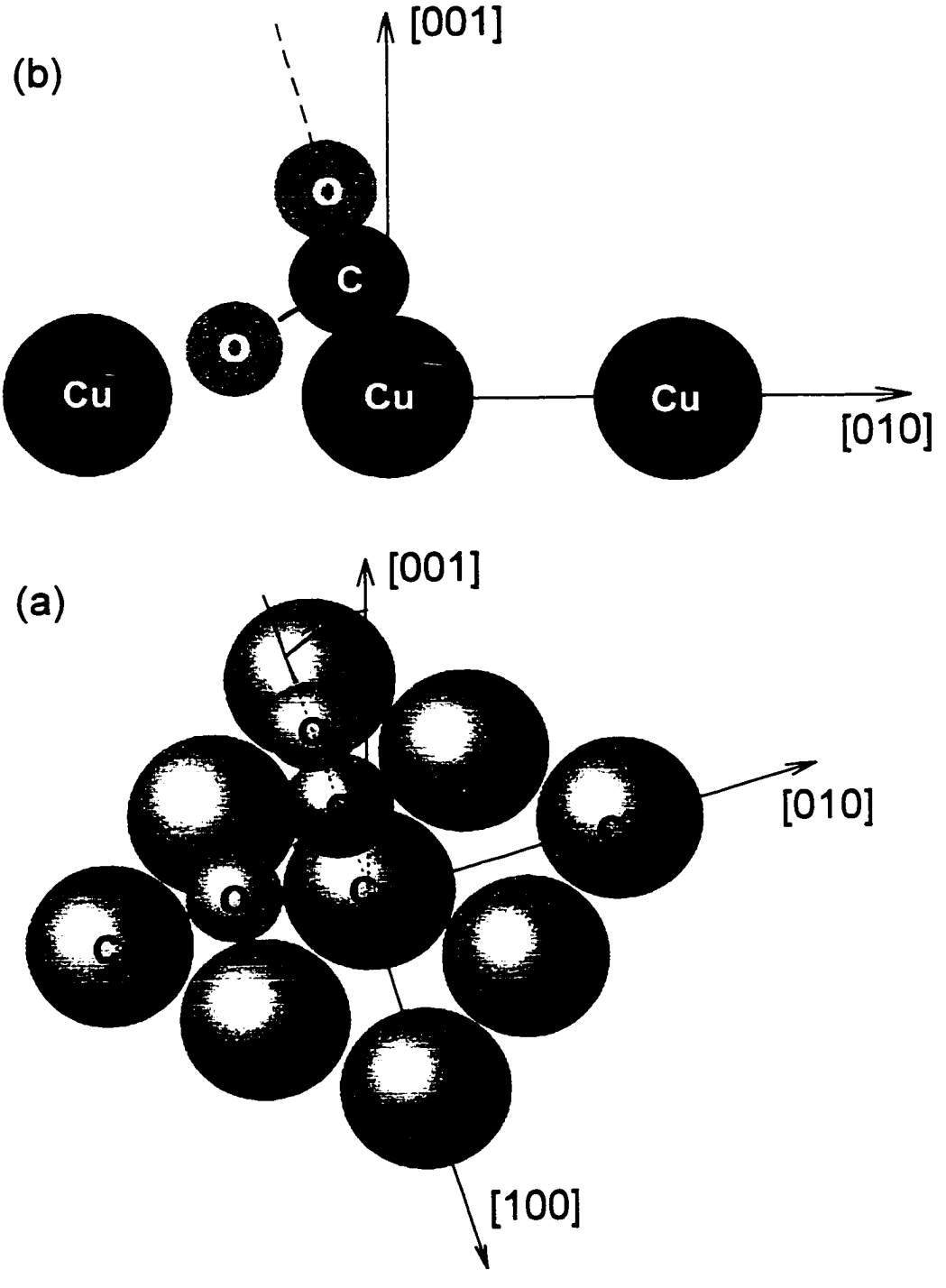

Figure 3.13 Perspective (a) and side-view (b) diagrams of a proposed bonding structure for CO coadsorbed with O on Cu(100).

Reproduced with permission of the copyright owner. Further reproduction prohibited without permission.

with its frequency blue-shifted from its nominal position at 2089 cm^{-1} (found in the low-temperature adsorption case) [3]. This blue-shifted feature could be the result of direct interaction between an as-formed CO and a nearby C or hydrocarbon species (Figure 3.9-3.11) produced in the ion irradiation process. In this model, a neighboring C or hydrocarbon species may deplete electrons in the $2\pi^*$ anti-bonding orbital of the CO molecule, hence strengthening the CO triple bond and causing a blue shift in the C–O stretching frequency. The direct interaction between CO and a C or hydrocarbon neighbor gives rise to a C–CO or hydrocarbon–CO quasi-complex that stabilizes CO on Cu(100) at RT. The observed double-peak structure in Figure 3.9-Figure 3.11 can therefore be attributed to the formation of these quasi-complexes, i.e., O–CO for the red-shifted CO peak and C–CO or hydrocarbon–CO for the blue-shifted CO peak, at different locations of the surface. This model is also consistent with the fact that the relative intensity of the peak at 2163 cm^{-1} to that of the peak at 2019 cm^{-1} increased with increasing dosage of ethylene ions, which should increase the hydrocarbon concentration at the expense of the O coverage on the surface (Figure 3.9). Although the surface-mediated (indirect) interactions of O and C with CO could also give rise to blue and red shifts in the C–O stretching frequency respectively, as previously suggested for CO on Mo(110) [21], such indirect interactions would not produce the stabilizing effect observed in our experiment.

3.7 Summary

In the present work, we have investigated the effects of low-energy electron or ion irradiation on the adsorption of CO on Cu(100) using HREELS and TPD techniques. Unusually stable CO adsorption on Cu(100) at RT was found as a result of the surface reaction: C (ad.) + O (ad.) $\rightarrow$ CO (ad.), whereby the atomic reactants C and O were produced *in situ* by electron irradiation of CO/Cu(100) or by ion irradiation of Cu(100) in CO or in C_2H_4 with pre- and post-exposure of O_2. In particular, CO adsorption was found to be stabilized on Cu(100) at a temperature as high as 420 K, and was characterized by a red shift of 73 cm^{-1} in the nominal ν(C–O) frequency (observed at low temperature). Different possible effects induced by electron or ion irradiation have been considered. To explain the observed red shift and stabilization effects, we propose a bonding model that involves direct

Reproduced with permission of the copyright owner. Further reproduction prohibited without permission.

interaction between a CO molecule on an atop site and a coadsorbed O atom in a neighboring four-fold hollow site. At higher ethylene ion dosage, a blue-shifted CO feature was also found in the corresponding HREELS spectra. This feature can also be explained by using the direct interaction model with CO interacting with coadsorbed C or C-containing species. The present work therefore not only provides direct evidence for in-situ CO production at RT by electron- and ion-induced surface reactions on an "unreactive" surface such as Cu(100), but also illustrates the importance of coadsorbed surface O and C or C-containing species on practical surface reactions. It further demonstrates the enormous potential of activating surface reactions by means of low-energy electron or ion irradiation and the effectiveness of studying this type of systems by using standard surface analysis methods such as HREELS and TPD.

3.8 References

[1] Gabor A. Somorjai, "Introduction to Surface Chemistry and Catalysis", Wiley, Toronto (1994).

[2] B. A. Sexton, Chem. Phys. Lett. **63**, 451 (1979).

[3] S. Andersson, Surf. Sci. **89**, 477 (1979).

[4] S. Andersson and B. N. J. Persson, Phys. Rev. Lett. **45**, 1421 (1980); Phys. Rev. B **24**, 3659 (1981).

[5] S. Andersson and J. B. Pendry, Phys. Rev. Lett. **43**, 363 (1979).

[6] G. J. Blyholder, J. Phys. Chem. **68**, 2772 (1964).

[7] E. L. Garfunkel, J. E. Crowell and G. A. Somorjai, J. Phys. Chem. **86**, 310 (1982).

[8] F. A. Cotton and G. Wilkinson, "Advanced Inorganic Chemistry", Wiley, New York (1988).

[9] B. A. Sexton, Surf. Sci. **88**, 299 (1979).

[10] D. L. Smith, "Thin Film Deposition Principles and Practice", Chapter 8, McGraw-Hill, New York (1995).

[11] M. H. Mohamed and L. L. Kesmodel, Surf. Sci. Lett. **185**, L467 (1987).

[12] It should be noted that differences in the changes in the C and O intensities observed by using AES and HREELS are due to the different surface sensitivity of each

Reproduced with permission of the copyright owner. Further reproduction prohibited without permission.

technique. In the present case, HREELS is considerably more surface sensitive than AES.

[13] M. Wuttig, R. Franchy, and H. Ibach, J. Electron Spectrosc. Relat. Phenom. **44**, 317 (1987), and references therein.

[14] M. Moskovits and J. E. Hulse, J. Phys. Chem. **81**, 2004 (1977).

[15] "Eight Peak Index of Mass Spectra", Vol. **1**, Mass Spectrometry Data Center, Aldermaston (1974).

[16] L. McDonnell, B. D. Powell, and D. P. Woodruff, Surf. Sci. **40**, 669 (1973).

[17] J. E. Greene, S. A. Barnett, J. E. Sundgren, and A. Rockett, "Ion Beam Assisted Film Growth", T. Itoh (ed.), Elsevier, Amsterdam (1989), p. 101.

[18] C. Nyberg, C. G. Tengstal, and S. Andersson, Chem. Phys. Lett. **87**, 87 (1982).

[19] L. Wallden, Surf. Sci. Lett. **134**, L513 (1983).

[20] L. H. Dubois, B. R. Zegarski, and H. S. Luftman, J. Chem. Phys. **87**, 1367 (1987).

[21] W. K. Kuhn, J. W. He, and D. W. Goodman, in "Surface Science of Catalysis", D. J. Dwyer and F. M. Hoffmann (eds.), ACS Symposium Series **482**, 71 (1992).

[22] P. Hollins and J. Pritchard, Surf. Sci. **134**, 91 (1983).

[23] G. Pacchioni and P. S. Bagus, Chem. Phys. **177**, 373 (1993).

[24] G. Herzberg, "Molecular Spectra and Molecular Structure", Van Nostrand, Toronto (1966), Vol. **3**, p. 429.

[25] P. Hollins and J. Pritchard, Surf. Sci. **89**, 486 (1979).

Reproduced with permission of the copyright owner. Further reproduction prohibited without permission.

Chapter 4
INTERACTIONS OF LOW-ENERGY (20-800 eV) NITROGEN IONS WITH Cu(100)

4.1 Introduction

Given its technological importance, the formation of a nitride film on metal and semiconductor surfaces continues to attract great interest in surface science [1]. In the case of a "generic" unreactive metal surface such as Cu(100), it is well known that molecular chemisorption of N_2 does not occur at RT. Furthermore, although dissociative adsorption of N_2 on Cu(100) has not been observed at RT [2,3], it has been shown to occur readily if activated by electron irradiation [4,5,6]. The resulting c(2×2) N overlayer on Cu(100) was found to be extremely stable, up to 770 K [5]. Studies by Mohamed and Kesmodel using HREELS further revealed that the Cu–N stretching vibrations in the perpendicular and parallel modes for N adsorbed on a four-fold-hollow site occur at 324 cm^{-1} and 750 cm^{-1}, respectively [6]. The bond length of the Cu–N bond has been determined to be 1.84 Å in an extended electron energy loss fine structure study [7].

In addition to electron-activated surface processes, low-energy ion-activated surface reactions are also found to be effective in generating new surface species [8]. For instance, Heskett *et al.* showed that the adsorption of atomic nitrogen on the (110) plane of Cu could be obtained by ion irradiation [9]. The interactions of an ion beam with a solid surface have been studied extensively both in the context of ion scattering [10,11] and ion beam processing [12]. The prominent effects of the interactions appear to greatly depend on the IE of the ion. According to the studies of the interactions of rare-gas ions with a solid surface [13], back-scattering is generally believed to be the predominant process for an IE below 30 eV, while radiation damage and other sputtering effects become increasingly important when the IE increases from 30 eV to 1000 eV. Furthermore, the entrapment (implantation) effect also becomes more evident at a higher IE. When a reactive gas is used as the source of the ion, the activation of surface reactions also plays an important role in determining the resulting surface properties. Indeed, in practical applications such as ion- or plasma-assisted thin films deposition [14], reaction activation and sputtering are believed to

Reproduced with permission of the copyright owner. Further reproduction prohibited without permission.

introduce competing results. In the present work, we investigate the interactions of low-energy N_2^+ and N^+ ions with Cu(100) by using TPD, LEED and HREELS. We show that "surface" nitrogen atoms that make up the c(2×2) overlayer on Cu(100) coexist with "entrapped" nitrogen species (that arise from N^+ or N_2^+ implantation) in the sub-surface region when the IE is greater than 75 eV. Of particular interest is the dependence of their relative concentrations on different experimental conditions (including, in particular, the IE and the ion dosage) used for the ion irradiation. Finally, the effects of radiation damage on the formation of the surface and entrapped nitrogen species are also investigated.

4.2 Results and Discussion

The experimental setup for ion irradiation has been described in Chapter 2 (see Figure 2.1). Unlike electron-activated adsorption [5,6], where contribution from neutral nitrogen atoms is possible, only positive ions (N^+ or N_2^+) could reach the sample in the present sputtering setup. Furthermore, because the ionization cross section for N_2^+ is much larger than that for N^+ [15], the impact dissociation of N_2^+ upon collision with the surface may play an important role in the production and subsequent chemisorption of atomic nitrogen [4,16].

Figure 4.1 shows the TPD profiles of mass 28 for a Cu(100) sample after ion irradiation with 12 kL of N_2 at RT as a function of IE. Mass 28 corresponds to the parent ion of N_2, which came from recombinative desorption of N adsorbed on the surface because no evidence for molecular adsorption of N_2 has been found [5]. The desorption maximum at 680 K for 20 eV IE (Figure 4.1a) was found to shift gradually to a higher temperature of 760 K when the IE was increased to 200 eV (Figure 4.1e). Further increase in the IE to 800 eV did not affect the position of the desorption maximum (Figure 4.1f-h). It should be noted that the IE used for the ion irradiation is directly related to the effective coverage because a higher ion deposition rate can be obtained at a higher IE. This coverage-dependent shift of the desorption maximum (Figure 4.1a-e) was confirmed by a similar shift to a higher temperature found for a sample prepared with a longer irradiation time at 20 eV IE (not shown). The shift in the desorption maximum to a higher temperature below 200 eV IE would suggest a zeroth-order desorption kinetics process, contrary to the second-order

Reproduced with permission of the copyright owner. Further reproduction prohibited without permission.

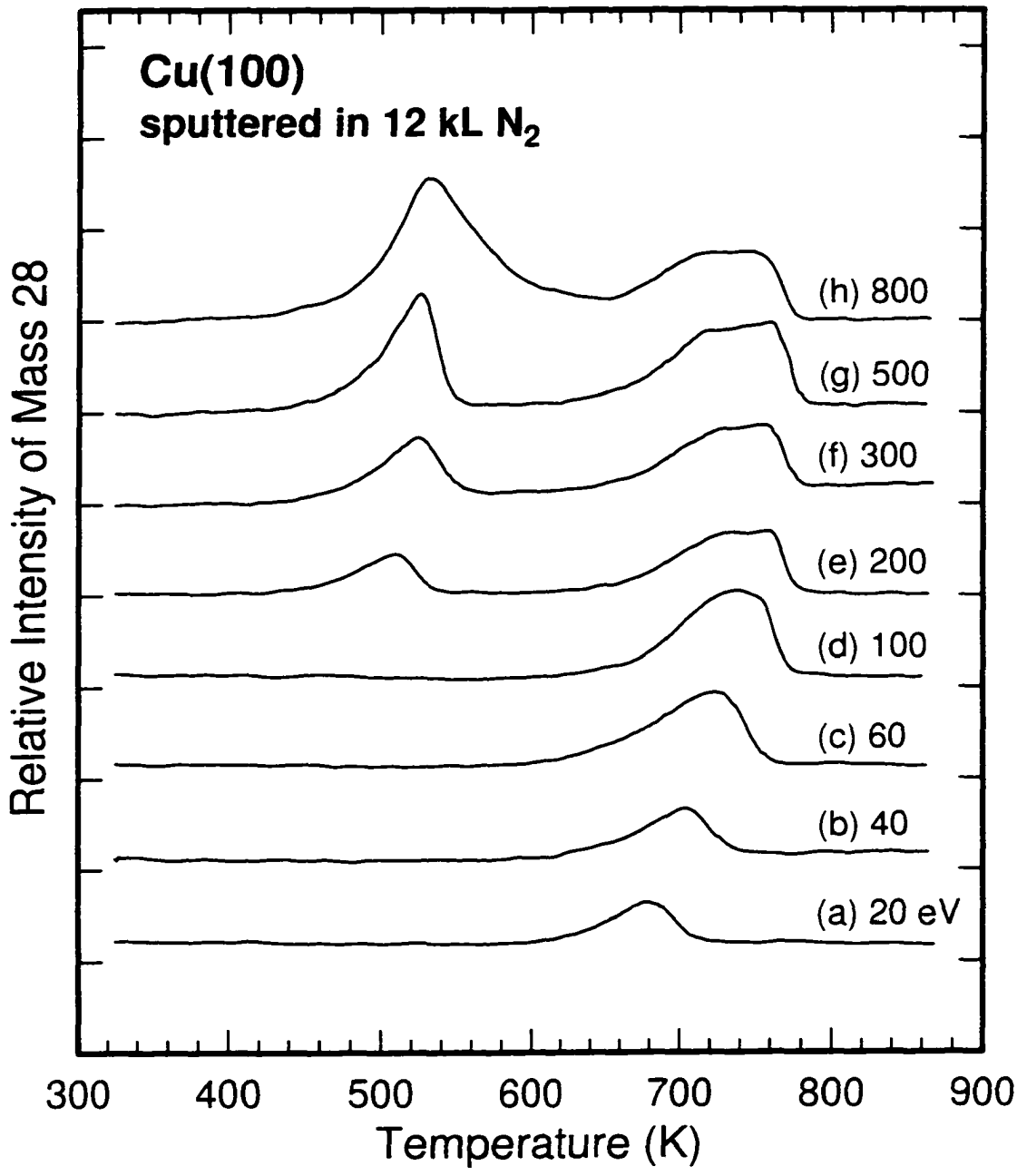

Figure 4.1 Temperature programmed desorption profiles of the parent ion (mass 28) of N_2 for Cu(100) ion-irradiated with 12 kL of N_2 at an impact energy of (a) 20, (b) 40, (c) 60, (d) 100, (e) 200, (f) 300, (g) 500, and (h) 800 eV.

Reproduced with permission of the copyright owner. Further reproduction prohibited without permission.

kinetics expected for recombinative desorption [17]. A plausible explanation is that the steady-state approximation may not be applicable in the present case and that the observed desorption process involves a coverage-dependent activation energy [18]. Above 100 eV IE, a second desorption peak appeared at a (lower) temperature of 510 K (Figure 4.1e). As the IE was increased, this lower-temperature feature became more intense and its desorption maximum shifted to a higher temperature, which provided support for the hypothesis that a higher effective ion dosage and deeper implantation could be achieved with irradiation at a higher IE. In contrast, the intensity of the higher-temperature desorption feature appeared to level off when the IE was above 200 eV (Figure 4.1e-h). Furthermore, the higher-temperature peak was found to be broadened with increasing IE and become a double-peak band above 200 eV IE, lending support for the on-set of adsorption of atomic nitrogen on the less stable sites after the c(2×2) sites were saturated. These "less stable" sites may include adsorption sites related to surface defects.

For IE below 200 eV, the corresponding samples (Figure 4.1a-d) exhibited a diffuse c(2×2) LEED pattern. The LEED pattern became a diffuse (1×1) pattern at 200-500 eV IE (Figure 4.1e-g) and totally disordered above 500 eV IE (Figure 4.1h). The gradual degradation in the sharpness of the observed LEED spots with increasing IE was consistent with the increase in surface damage caused by ion irradiation. Upon annealing the samples to 600 K for 10 minutes, the LEED patterns of the samples prepared with different IEs (Figure 4.1a-h) all reverted back to a sharp c(2×2) pattern observed previously [3,5]. The "sharpest" c(2×2) LEED pattern, obtained after the 600 K anneal, was found for the sample prepared with an IE between 100 eV and 200 eV, indicating that there were more complete c(2×2) domains on the sample so prepared than those irradiated at a lower IE but with less radiation damage than those irradiated at a higher IE. If the samples (Figure 4.1a-h) were further annealed to 800 K for 10 minutes, the LEED pattern changed from a c(2×2) pattern [corresponding to N/Cu(100)] to a sharp (1×1) pattern [corresponding to clean Cu(100)]. Evidently, the c(2×2) LEED pattern corresponds only to the higher-temperature desorption feature observed above 600 K. A similar desorption profile with two desorption peaks has also been reported by Heskett *et al.* [9] for a Cu(110) surface bombarded with a nitrogen ion beam at 200 eV. In particular, a (2×3) LEED pattern was attributed to the corresponding

Reproduced with permission of the copyright owner. Further reproduction prohibited without permission.

higher-temperature desorption feature of the nitrogen overlayer while no assignment was given for the lower-temperature desorption feature [9].

In order to determine whether the lower-temperature desorption band was caused by a different chemisorption state or by entrapment of N^+ or N_2^+ during ion irradiation, we performed HREELS experiments on a typical sample reported in Figure 4.1. Figure 4.2 shows the HREELS spectra, recorded in both the specular and 10° off-specular geometries, for a Cu(100) surface ion-irradiated with 12 kL of N_2 at 200 eV IE for two different annealing temperatures. It should be noted that the peak intensities of the energy loss features are relative only to the corresponding elastic peak in a single HREELS spectrum, and the elastic peaks in all the spectra have been normalized identically to one another. Since the desorption maximum of the lower-temperature feature occurs above 370 K (Figure 4.1e), annealing the sample to 370 K should only produce the effect of surface smoothing, resulting in a more "reflective" surface to enhance the signals in our HREELS experiments. On the other hand, annealing the sample to 600 K would remove the nitrogen associated with the lower-temperature desorption feature (Figure 4.1e). All four EELS spectra in Figure 4.2 depict a prominent vibrational feature at 316 cm^{-1}, which has been previously assigned to a Cu–N stretch in the perpendicular mode by Mohamed and Kesmodel [6]. An additional weak feature at 752 cm^{-1} can also be discerned in the off-specular spectra in Figure 4.2. In accord with the dipole selection rules for surface electron scattering [19] and with the previous work [6], this feature is attributed to the parallel modes of the Cu–N stretching vibration. Evidently, there is no notable difference (between the specular spectra and between the off-specular ones) for the sample after annealing to the two different temperatures. The changes in the relative peak intensities are likely caused by differences in the surface reflectivity as a result of the different annealing temperatures. Because vibrational HREELS is a surface-sensitive technique, the lack of any substantial difference between the HREELS spectra for the 370 K and 600 K anneals suggests that the lower-temperature desorption feature at ~520 K (Figure 4.1e) does not correspond to a new chemisorption state. The lower-temperature desorption band may therefore be due to implantation of N^+ or N_2^+ into the sub-surface region during the ion irradiation

Reproduced with permission of the copyright owner. Further reproduction prohibited without permission.

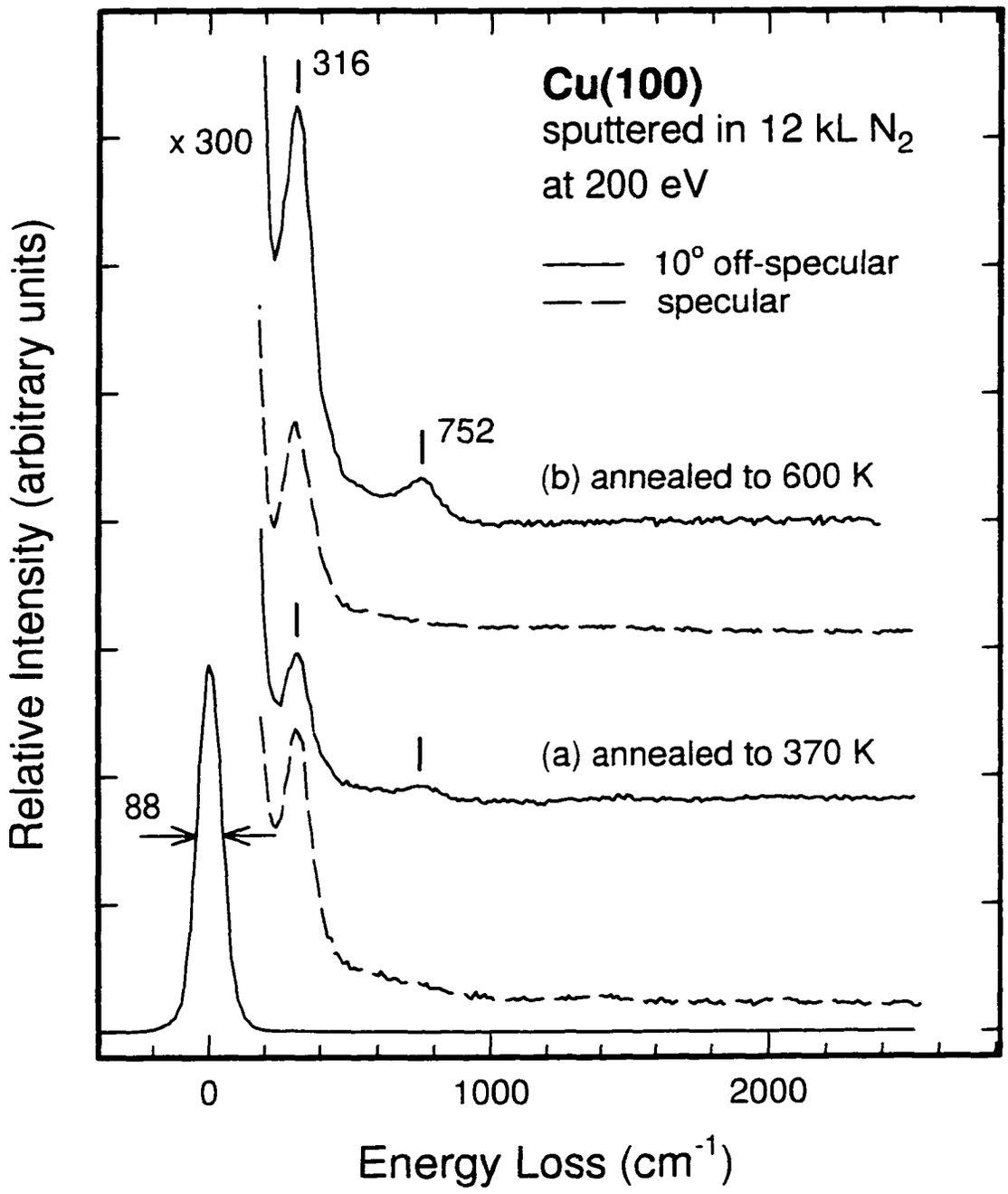

Figure 4.2 Vibrational electron energy loss spectra for Cu(100) ion-irradiated with 12 kL of N_2 at an impact energy of 200 eV followed by annealing to (a) 370 K and (b) 600 K, recorded in the specular (dashed lines) and 10° off-specular (solid lines) directions.

Reproduced with permission of the copyright owner. Further reproduction prohibited without permission.

process. This hypothesis is also supported by the fact that the desorption intensity of the lower-temperature desorption feature increases with increasing IE, in contrast to that of the higher-temperature feature (Figure 4.1). Furthermore, the implanted nitrogen species were likely dominated by the atomic form rather than the molecular form, because the IE employed was sufficiently high to overcome the dissociation energy of N_2 (9.8 eV) [5]. The different extent of implantation in the sub-surface region as a result of different IEs would lead to a zero-order desorption kinetics for the entrapped species [17], which is consistent with the observed shift of the lower-temperature desorption peak to a higher temperature shown in Figure 4.1e-h. Finally, in accord with the conclusion made by Tibbetts [5], our HREELS results also do not reveal any features that could be attributed to molecularly adsorbed nitrogen species, which were previously proposed by Lee and Farnsworth [3].

Figure 4.3 shows the effects of ion dosage on the TPD profiles at a fixed IE of 200 eV. At this IE, the higher-temperature desorption feature (corresponding to atomic nitrogen chemisorption) could be observed at a relatively low ion dosage (Figure 4.3a). The intensity of this higher-temperature feature became saturated at higher dosages (Figure 4.3b-c), in contrast to that of the lower-temperature feature (corresponding to nitrogen implantation), which continued to increase with increasing ion dosage. Moreover, the broadening of the higher-temperature desorption peak at a higher dosage also lends support to the proposed adsorption of nitrogen on other (surface defect related) sites after saturation of the four-fold hollow sites.

When the IE was below 200 eV, the lower-temperature desorption peak could not be observed (Figure 4.1), which is consistent with the notion that less energetic ions are less likely to implant into the bulk. However, if the ion dosage was increased sufficiently by extending the irradiation time, the lower-temperature desorption band could again be obtained. Figure 4.4 shows the TPD results of Cu(100) irradiated with a higher nitrogen ion dosage (i.e., six times that used in Figure 4.1) for three typical IEs not exceeding 100 eV. Evidently, a weak desorption peak at ~500 K could be observed in the TPD profiles for 75 eV and 100 eV but not in that for 50 eV, which suggests that an upper bound of the minimum IE required for the implantation to occur is below 75 eV. Furthermore, the entrapment of nitrogen species did not appear to affect the adsorption of atomic nitrogen

Reproduced with permission of the copyright owner. Further reproduction prohibited without permission.

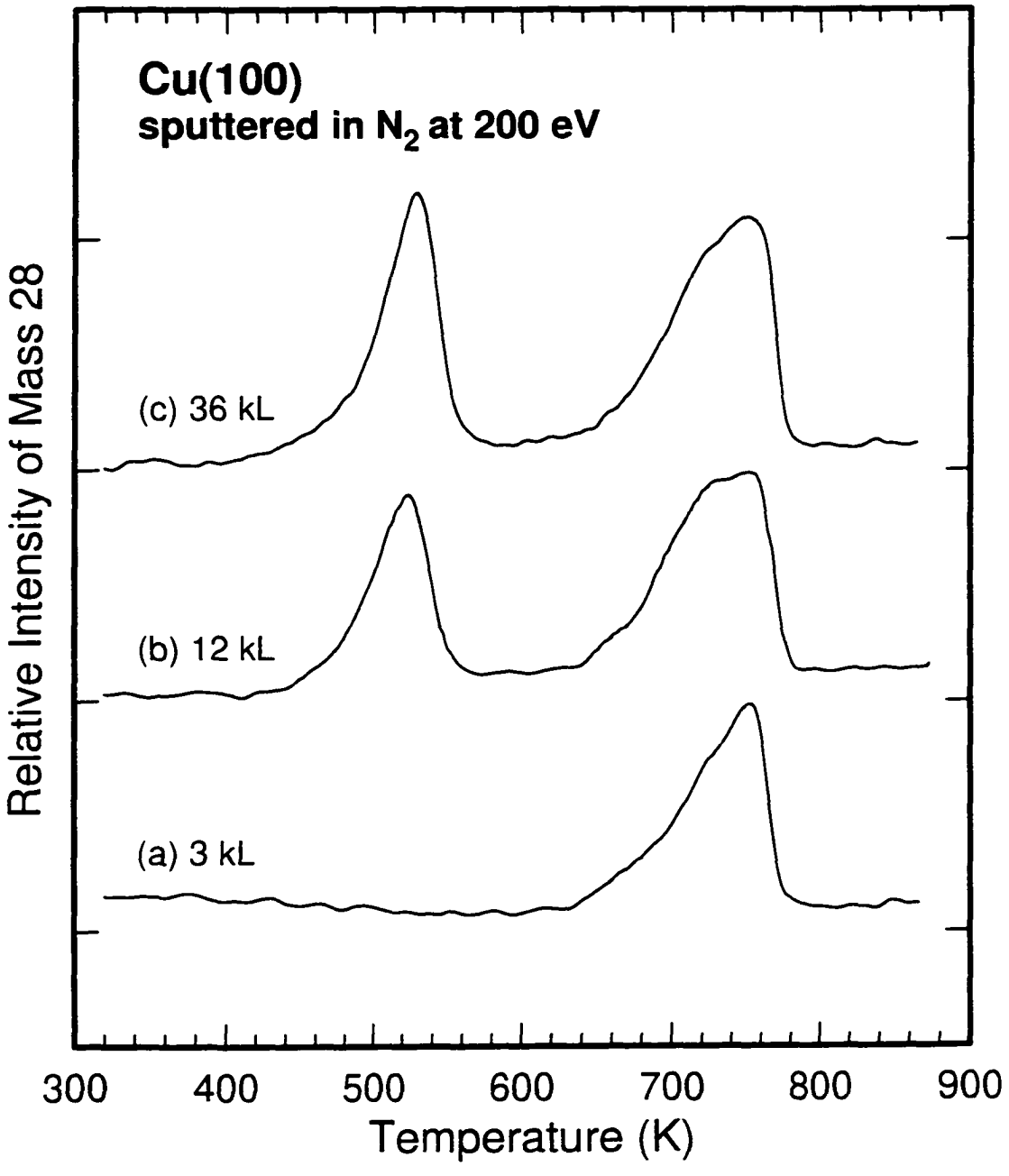

Figure 4.3 Temperature programmed desorption profiles of the parent ion (mass 28) of N_2 for Cu(100) ion-irradiated at an impact energy of 200 eV with N_2 dosages of (a) 3 kL, (b) 12 kL, and (c) 36 kL.

Reproduced with permission of the copyright owner. Further reproduction prohibited without permission.

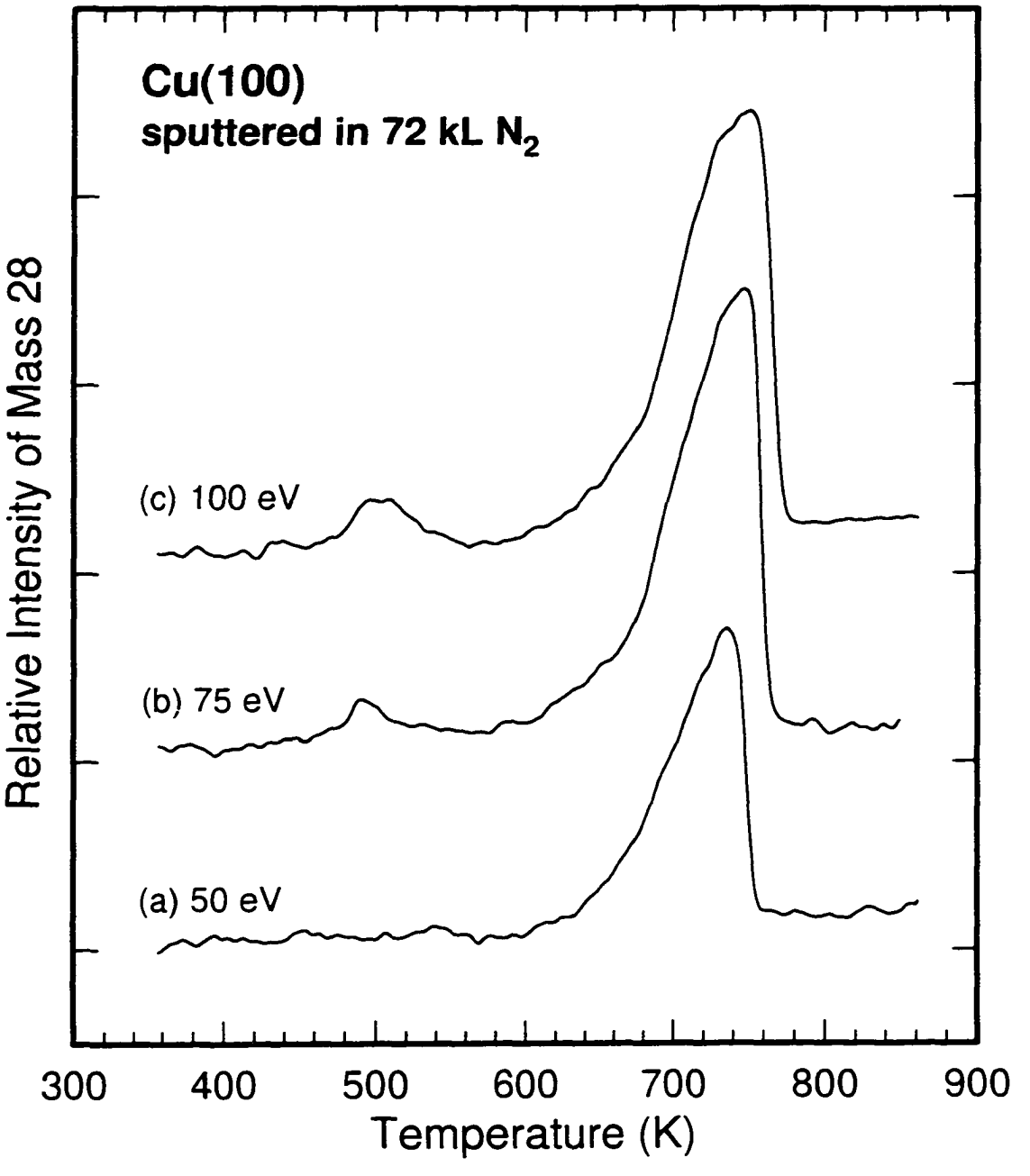

Figure 4.4 Temperature programmed desorption profiles of the parent ion (mass 28) of N_2 for Cu(100) ion-irradiated with 72 kL of N_2 at an impact energy of (a) 50 eV, (b) 75 eV, and (c) 100 eV.

Reproduced with permission of the copyright owner. Further reproduction prohibited without permission.

that gave rise to the c(2×2) overlayer on Cu(100). It apparently occurred only after the adsorption of atomic nitrogen was nearly complete, as depicted by the saturated intensity of the higher-temperature desorption feature in Figure 4.4b.

It is well known that ion irradiation at an IE above 30 eV is sufficient to generate defect sites on a surface [12,20]. In order to examine the effects of defects, we compare the desorption of N_2 from an amorphous surface [obtained by Ar^+ sputtering a Cu(100) surface at 500 eV IE] with that from a clean surface at two different IEs of the nitrogen ions (Figure 4.5). Evidently, there is no notable difference in the TPD profiles between the Ar^+-pre-sputtered surface and the clean Cu(100) surface for both 50 eV (Figure 4.5a) and 200 eV IE (Figure 4.5b). If the lower-temperature desorption band was due to nitrogen adsorbed on the defect sites of the surface, we would expect stronger lower-temperature desorption on the Ar^+-pre-sputtered surface because of the high concentration of defect sites. The lack of any discernible difference in the TPD results between the two surfaces therefore provides strong evidence for our previous assignment of the lower-temperature peak to implanted nitrogen species. In the case of the chemisorbed nitrogen (the higher-temperature desorption feature), the similarities observed for the two different surface conditions suggest possible surface migration of N, whereby the nitrogen atoms, initially adsorbed at different sites of the amorphous surface with equal efficiency, underwent surface diffusion into the more stable four-fold-hollow sites [giving the c(2×2) reconstruction] when the temperature was increased.

4.3 Summary

We present the TPD and HREELS results for a Cu(100) surface after different treatments of nitrogen ion irradiation. In addition to the desorption band at 760 K, corresponding to recombinative desorption of "surface" nitrogen atoms primarily adsorbed on four-fold-hollow sites, the TPD results reveal the on-set of a second desorption band at 520 K. This new lower-temperature desorption feature is attributed to "entrapped" nitrogen species in the sub-surface region, in good accord with the HREELS results. Furthermore, nitrogen implantation appears to be insignificant when the IE is less than 75 eV. Depending on the IE and ion dosage, the ion irradiation process can also introduce different

Reproduced with permission of the copyright owner. Further reproduction prohibited without permission.

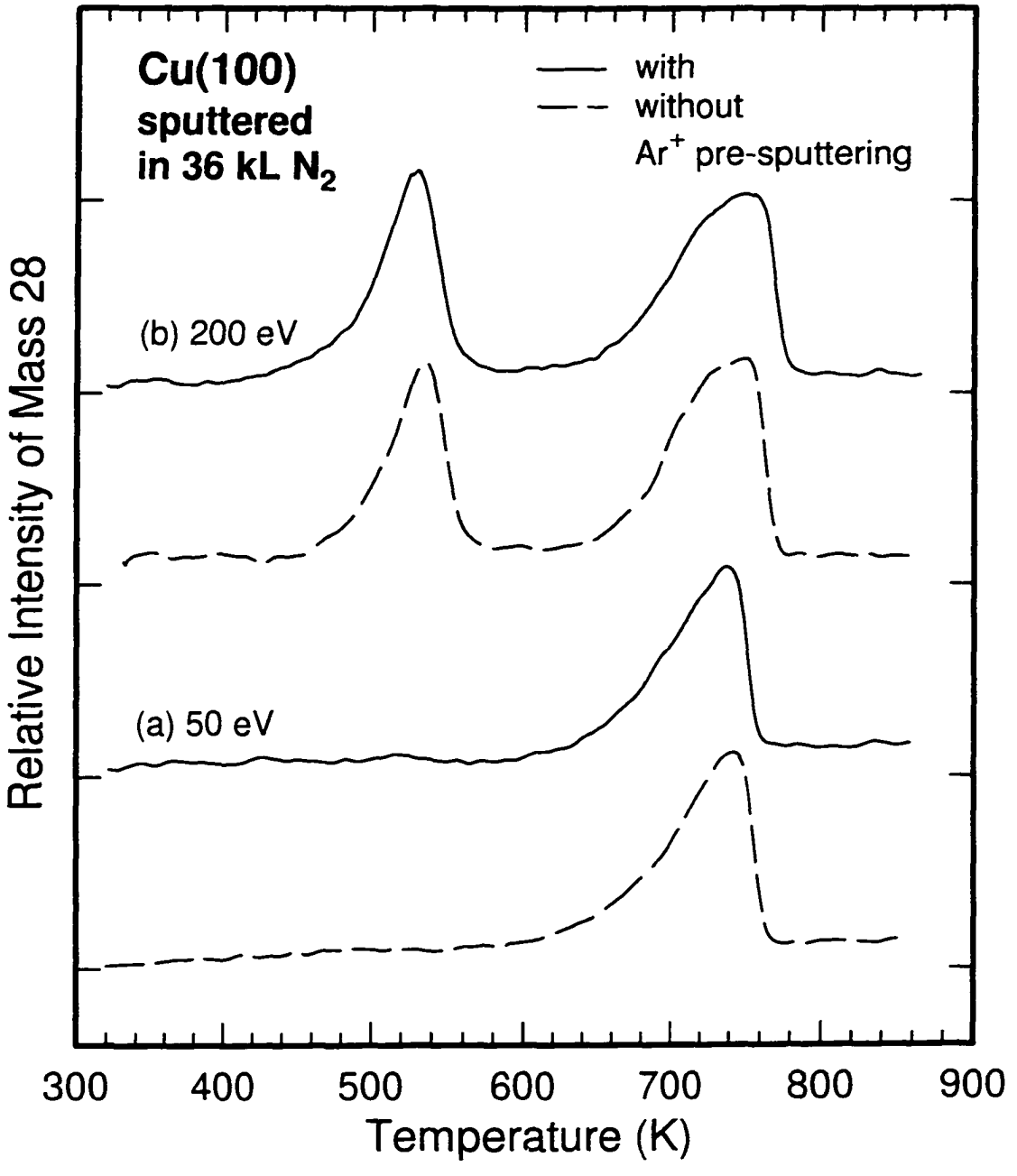

Figure 4.5 Temperature programmed desorption profiles of the parent ion (mass 28) of N_2 for a clean Cu(100) surface ion-irradiated with 36 kL of N_2 at an impact energy of (a) 50 eV and (b) 200 eV, with (solid lines) and without (dashed lines) Ar^+ pre-sputtering at 500 eV.

Reproduced with permission of the copyright owner. Further reproduction prohibited without permission.

levels of damage to the surface. The surface defects do not appear to significantly affect the concentration of the implanted nitrogen species and that of the nitrogen atoms chemisorbed on the c(2×2) sites. Adsorption on these less stable defect sites occurs only after the saturation of the more stable c(2×2) sites.

4.4 References

[1] I. Kusunoki, T. Takaoka, Y. Igari, and K. Ohtsuka, J. Chem. Phys. **101**, 8238 (1994).

[2] B. M. W. Trapnell, Proc. R. Soc. London A **218**, 566 (1953).

[3] R. N. Lee and H. E. Farnsworth, Surf. Sci. **3**, 461(1965).

[4] H. F. Winters, D. E. Horne, and E. E. Donaldson, J. Chem. Phys. **41**, 2766 (1964).

[5] G. G. Tibbetts, J. Chem. Phys. **70**, 3600 (1978).

[6] M. H. Mohamed and L. L. Kesmodel, Surf. Sci. Lett. **185**, L467 (1987).

[7] Q. Dai and A. J. Gellman, Surf. Sci. **248**, 86 (1991).

[8] T. Itoh (ed.), "Ion Beam Assisted Film Growth", Elsevier, Amsterdam (1989).

[9] D. Heskett, A. Baddorf and E. W. Plummer, Surf. Sci. **195**, 94 (1988).

[10] H. Akazawa, I. Kusunoki, and Y. Murata, Surf. Sci. **177**, 577 (1986).

[11] J. W. Rabalais (ed.), "Low Energy Ion - Surface Interactions", Wiley, Baffins Lane (1994).

[12] J. J. Cuomo, S. M. Rossnagel, and H. R. Kaufman (eds.), "Handbook of Ion Beam Processing Technology", Noyes Publications, Park Ridge (1989).

[13] P. A. Redhead, J. P. Hobsen and E. V. Kornelsen, "The Physical Basis of Ultrahigh Vacuum", Chapman and Hall, London (1968).

[14] D. L. Smith, "Thin Film Deposition Principles and Practice", McGraw-Hill, New York (1995), Chapter 8.

[15] J. W. Gallagher, C. E. Brion, J. A. R. Samson and P. W. Langhoff, J. Phys. Chem. Ref. Data **17**, 9 (1988).

[16] H. F. Winters, J. Chem. Phys. **44**, 1472 (1966).

[17] P. A. Redhead, Vacuum **12**, 203 (1962).

[18] H. Froitzheim, P. Schenk, and G. Wedler, J. Vac. Sci. Technol. A **11**, 345 (1993).

[19] H. Ibach and D. L. Mills, "Electron Energy Loss Spectroscopy and Surface

Reproduced with permission of the copyright owner. Further reproduction prohibited without permission.

Vibrations", Academic, New York (1982). Also: H. Ibach, "Electron Energy Loss Spectrometers", Springer Ser. Opt. Sci.,Vol. **63**, Springer-Verlag, New York (1991).

[20] M. Ritter, M. Stindtmann, M. Farle and K. Baberschke, Surf. Sci. **348**, 243 (1996).

Reproduced with permission of the copyright owner. Further reproduction prohibited without permission.

Chapter 5

FORMATION OF SURFACE RADICALS ON N-PRECOVERED Cu(100) INDUCED BY LOW-ENERGY ION IRRADIATION IN ETHYLENE

5.1 Introduction

The chemisorption and surface reactions of hydrocarbons on metal surfaces have continued to be the subjects of intense investigation in surface science. Of particular interest is the dissociative chemisorption of hydrocarbons on transition metal surfaces, such as platinum and related bimetallic alloys, because of their applications in hydrocarbon catalysis [1]. In particular, hydrocarbon adsorbates were reported to undergo sequential C–H bond breaking and skeletal rearrangement between 340 K and 700 K to produce chemically active hydrocarbon fragments, which became an integral part of the catalytic surface [2]. As the simplest unsaturated hydrocarbon with a single π bond, ethylene has often been used as a model system for studying chemisorption on metal surfaces. For instance, decomposition of chemisorbed ethylene has been found to occur on various transition metal surfaces (including Pt, Pd, Rh, Ru, and Ni) [1] and is believed to lead to the formation of such novel surface species as ethylidyne, vinylidene and vinyl radicals [1,3]. Similar decomposition processes have, however, not been observed for noble metal surfaces. Furthermore, unlike the chemisorption of ethylene on most transition metal surfaces, which involves di-σ or rehybridization bonding to the substrate, ethylene usually retains most of its π bonding character when adsorbed on noble metal surfaces [such as Cu(100) and Ag(110)] [3,4]. In practice, ethylene was found to adsorb molecularly on Cu(100) only at low temperature (<200 K) with the π bond parallel to the surface, and to undergo molecular desorption when the temperature was increased. Also found were a number of characteristic vibrations for ethylene adsorbed at 80 K, which include the C–H out-of-plane bending mode at 901 cm^{-1}, the C–H scissoring mode at 1287 cm^{-1}, the C=C stretch at 1553 cm^{-1} and the C–H stretch at 2984 cm^{-1} [5].

In recent years new technologies involving ion or plasma assisted surface reactions have been widely used for developing novel materials [6]. In particular, various organic thin films deposited on metal and semiconductor surfaces have been achieved by activating

Reproduced with permission of the copyright owner. Further reproduction prohibited without permission.

hydrocarbon reactants with low-energy ion beams or plasmas. In these applications, the reactive carbonaceous species were found to play a crucial role in the formation of these thin films [7]. Because the reaction mechanisms of surface reactions involving ion-activated hydrocarbon species are fundamentally different from that of thermal gas-surface reactions, it is of practical interest to investigate the adsorption properties and surface chemistry of hydrocarbon fragments created by ion irradiation. Depending on the impact energy of the ions, other processes (such as ion implantation and creation of defect sites) can also occur concurrently with reaction activation during ion irradiation (Chapter 4). The interrelations among the ion-induced effects of different processes are particularly intriguing. Due to the potential complexities of the ion-induced effects, we again choose a relatively unreactive and well-defined surface such as Cu(100) for the aforementioned studies. Together with pre-exposures of O (Chapter 3, Section 3.5) and N atoms, we can extend these studies to investigate the interactions between the pre-deposited atoms and ethylene ions and their fragments. Examining the possible initial surface products from these ion-surface reactions is of practical interest to applications in catalysis and thin films deposition. In particular, hydrocarbon fragments produced during ion irradiation in ethylene at RT are found to react with clean, O-precovered, and N-precovered Cu(100) surfaces to form different surface species. In the case of clean Cu(100), the HREELS results suggest "stabilized" chemisorption of hydrocarbon species up to ~600 K. For the O-precovered surface, both red- and blue-shifted CO stretching modes were observed in the HREELS spectra at high ethylene ion dosage. These results have already been presented in Chapter 3 (Section 3.5) in connection with CO stabilization. In the case of low-energy ethylene ion interactions with a N-precovered Cu(100) surface, the presence of CN and NH species generated *in situ* on the surface during ion irradiation is inferred from the observed HREELS features attributable to C≡N and N–H stretching modes. Other effects due to defect sites created by low-energy ion irradiation are also investigated.

In the present experimental setup, ethylene was ionized by electrons with 200 eV kinetic energy inside the ion gun and only positive ions from the ion gun could reach the sample without mass selection (Chapter 2). A cracking pattern of ethylene revealed that the parent ions, $C_2H_4^+$, are the majority ions, with other smaller ions such as $C_2H_3^+$, $C_2H_2^+$,

Reproduced with permission of the copyright owner. Further reproduction prohibited without permission.

C_2H^+, CH_2^+ and CH^+ present with decreasing concentrations [8]. When the ions collide with the surface, they may become neutralized or may further dissociate into smaller fragments including carbon and hydrogen atoms. The resulting radicals may in turn undergo reactions with the substrate atoms or pre-deposited atoms (O or N) to form stable surface species at RT.

5.2 Hydrocarbon species created on clean Cu(100)

In an earlier study by Nyberg, Tengstal and Andersson, C_2H_4 was found to adsorb molecularly on clean Cu(100) only at low temperature [5]. In Chapter 3, the AES results (Figure 3.8) for Cu(100) exposed at RT to a relatively low dose (600 L) of ethylene ions at a low IE of 50 eV revealed the presence of surface carbon on the Cu(100) sample without any discernible HREELS feature (Figure 3.7). However, if the ion dosage and IE were increased, several prominent features were observed in the HREELS spectra. Figure 5.1 shows the HREELS spectra recorded after annealing to different temperatures for a clean Cu(100) surface ion-irradiated in 9 kL of C_2H_4 at 200 eV IE. After ion irradiation at RT (Figure 5.1a), the sample exhibited a diffuse (1×1) LEED pattern, which became sharper with increasing annealing temperature. In the corresponding HREELS spectra (Figure 5.1a-d), three broad bands centered at 764, 1392 and 2944 cm^{-1} were observed. Each of the bands appeared to be made up of several peaks that could not be resolved by our spectrometer, because the effective resolution was degraded by the roughened surface caused by ion irradiation. In order to identify the observed HREELS features, we replaced C_2H_4 with deuterated ethylene (C_2D_4) for ion irradiation and repeated the same experiment. The corresponding HREELS spectra shown in Figure 5.2 reveal that the bands at 547 and 2196 cm^{-1} can be assigned, respectively, to the isotope-shifted features at 764 and 2944 cm^{-1} for the C_2H_4 case shown in Figure 5.1a. The broad structure between 547 and 1086 cm^{-1} in Figure 5.2a can be attributed to the isotope-shifted features in the 764-1392 cm^{-1} region in Figure 5.1a. The small peak at 2944 cm^{-1} in Figure 5.2 is due to the presence of residual C_2H_4 in our 98% pure C_2D_4 sample. On the other hand, the broad band centered at 1384 cm^{-1} (which becomes more evident in Figure 5.2c-d) is found to be at essentially the same energy loss position as that at 1392 cm^{-1} in Figure 5.1. This feature is therefore not

Reproduced with permission of the copyright owner. Further reproduction prohibited without permission.

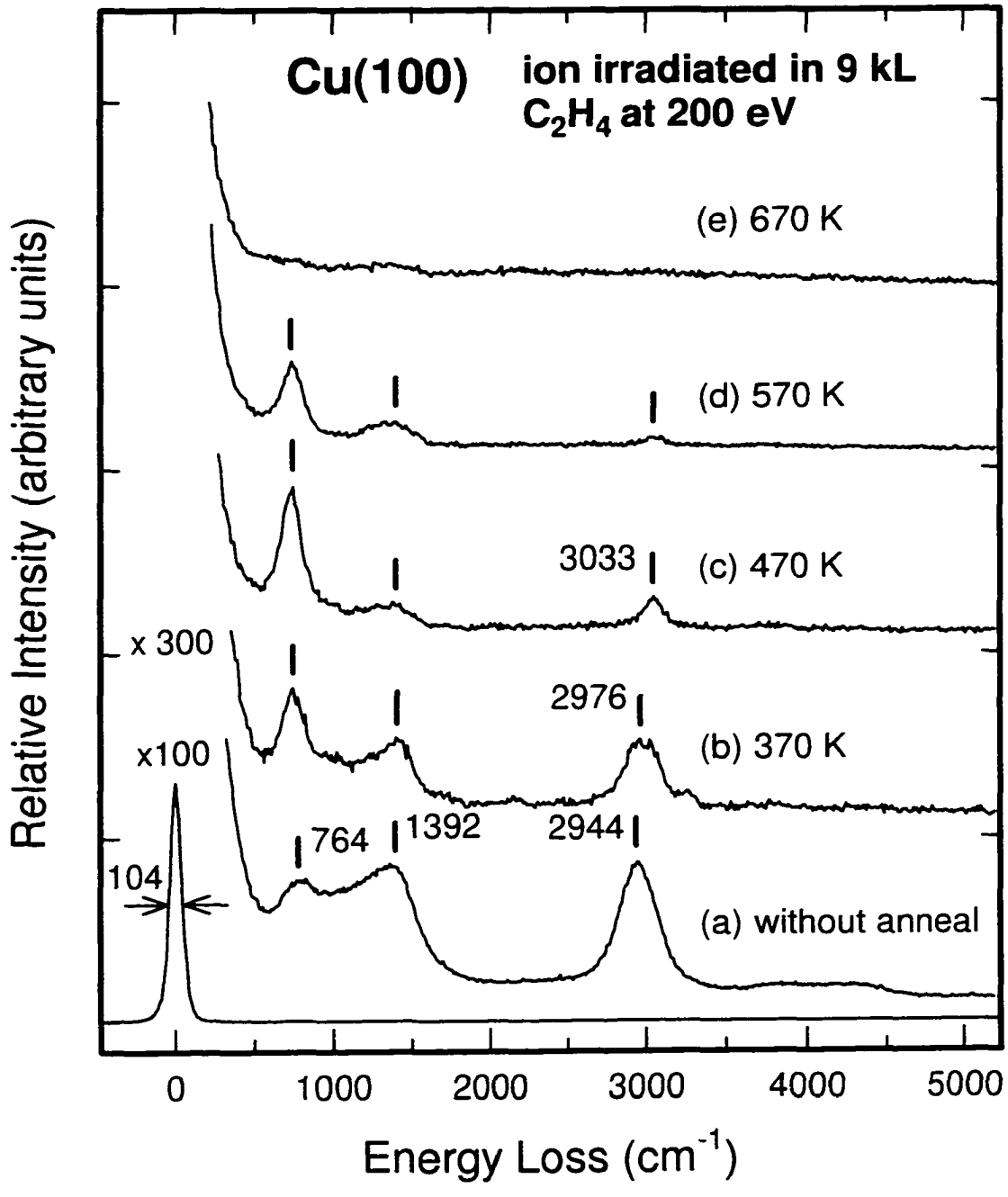

Figure 5.1 Vibrational electron energy loss spectra for (a) a clean Cu(100) surface ion-irradiated in 9 kL of C_2H_4 at 200 eV impact energy at room temperature, and for sample (a) annealed to (b) 370 K, (c) 470 K, (d) 570 K, and (e) 670 K.

Reproduced with permission of the copyright owner. Further reproduction prohibited without permission.

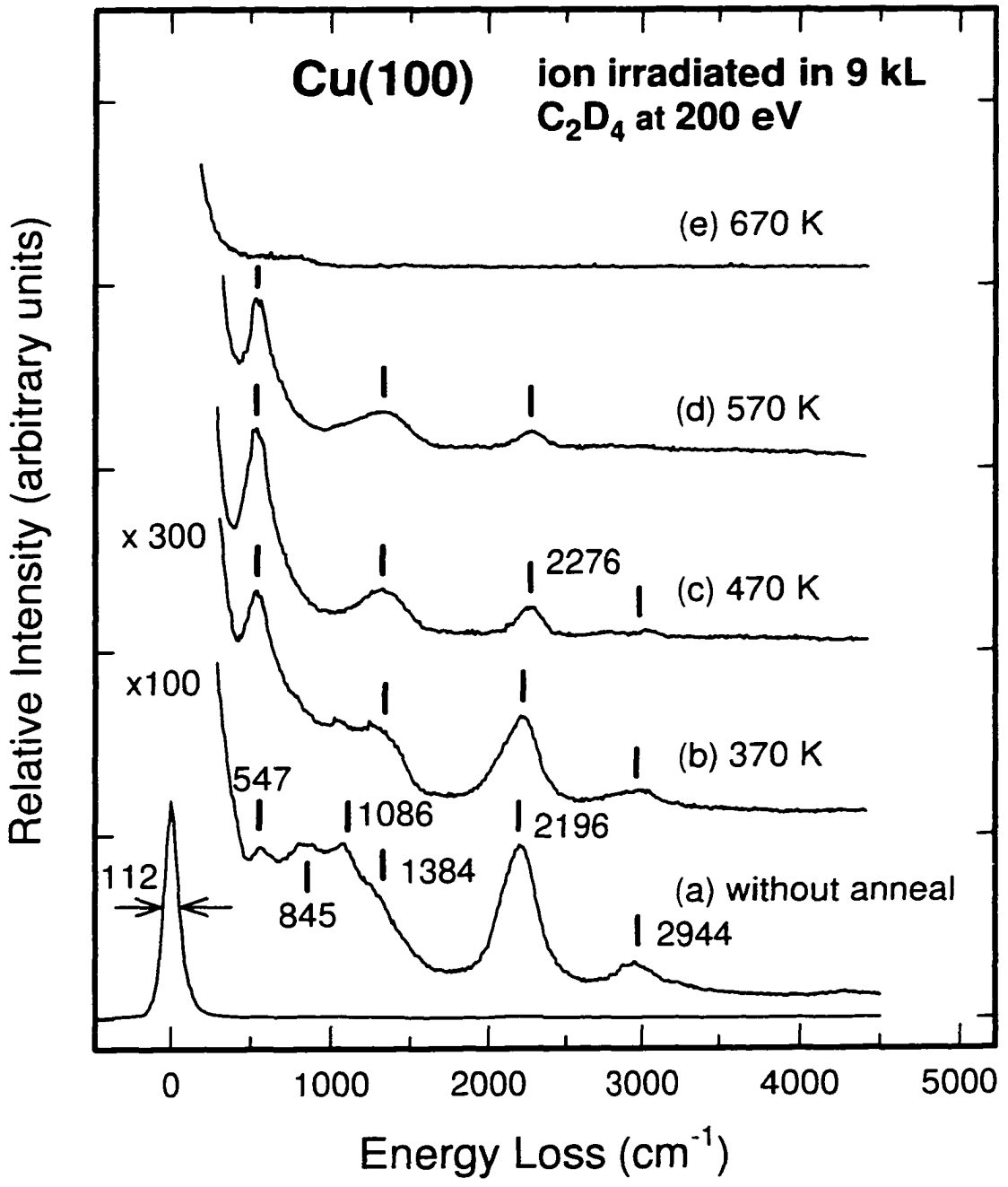

Figure 5.2 Vibrational electron energy loss spectra for (a) a clean Cu(100) surface ion-irradiated in 9 kL of C_2D_4 at 200 eV impact energy at room temperature, and for sample (a) annealed to (b) 370 K, (c) 470 K, (d) 570 K, and (e) 670 K.

Reproduced with permission of the copyright owner. Further reproduction prohibited without permission.

related to hydrogen and can be assigned to the stretching mode of a C=C bond. The characteristic stretching frequencies for the single and double C-to-C bonds in common hydrocarbons in the gas phase are generally located at ~900 cm^{-1} and ~1650 cm^{-1}, respectively [9]. Although the observed frequency (1392 cm^{-1}) is lower than that of a typical C=C double bond (1650 cm^{-1}), this frequency may vary from 1200 to 1600 cm^{-1} depending on the chemisorption geometry [e.g., 1200 cm^{-1} for C_2H_4/Ni(111) [10], 1440 cm^{-1} for C_2H_2/Si(100) [11], and 1570 cm^{-1} for C_2H_4/Ni(100) [3]]. The broadness of this band may be due to contributions from hydrocarbon species with a C=C bond adsorbed with different adsorption structures. In addition to the C=C contribution, the peak at 1392 cm^{-1} in Figure 5.1a may also contain a contribution from CH scissors modes, which are located in the same frequency region [12]. It should be noted that changing either the ethylene ion dosage between 4 kL and 32 kL or the IE between 50 eV and 500 eV in general only affects the overall intensities but not the widths of the HREELS features. HREELS spectra with similar intensities could be obtained if ion irradiation was performed for an amorphous Cu surface (obtained by sputtering Cu(100) in 2×10^{-5} Torr of Ar for 30 minutes at 500 eV IE). However, direct dosing of ethylene without ion irradiation on an amorphous Cu surface did not give rise to any adsorption, which indicates that the presence of defect sites did not play an important role in the observed adsorption.

In comparison with molecular adsorption of C_2H_4 on Cu(100) at low temperature [5], there are several notable differences in the observed vibrational features obtained by ion irradiation at RT. The broad feature centered at 2944 cm^{-1} (Figure 5.1a) suggests the presence of overlapping C–H stretching modes (both symmetric and asymmetric) in several hydrocarbon species, in marked contrast to the C_2H_4/Cu(100) system at 80 K which exhibited a sharp peak corresponding to a symmetric stretching mode (asymmetric mode was not observed because of the smaller cross section) [5]. In the low-temperature adsorption case, the sharp peak at 1553 cm^{-1} was assigned to the stretching vibration of a C=C double bond [5]. In the present experiment, no corresponding peak was observed near this frequency. Instead, the broad feature located at a lower frequency of 1392 cm^{-1} (Figure 5.1a) is indicative of adsorbates with a weakened C=C bond involving possibly quite different adsorption arrangements. Although the features between 764 and 1392 cm^{-1} in

Reproduced with permission of the copyright owner. Further reproduction prohibited without permission.

Figure 5.1 [or those between 547 and 1086 cm^{-1} for C_2D_4 in Figure 5.2] are not resolved, contributions from other modes (rock, twist, wag and scissors modes) of different hydrocarbon fragments are possible [12]. The most intense feature also occurs at a different location (764 cm^{-1} in Figure 5.1b-d) from the low-temperature adsorption case (901 cm^{-1}), which was assigned to an out-of-plane C–H bending mode [5]. The difference in the frequencies and the observed RT adsorption together suggest that the dominant species involves a different adsorption configuration from the π-bonded geometry found for C_2H_4 in the low-temperature adsorption case.

The vibrational frequencies along with their tentative assignments for the HREELS features obtained in the present ion-irradiation experiment are compared with those of the corresponding features for C_2H_4/Cu(100) at 80 K [5], gaseous C_2H_4 [9], and the CH_2 functional group [12] in Table 5.1. Figure 5.3 illustrates some of the plausible adsorption structures of ethylene-derived hydrocarbon species on Cu(100). The di-σ bonding

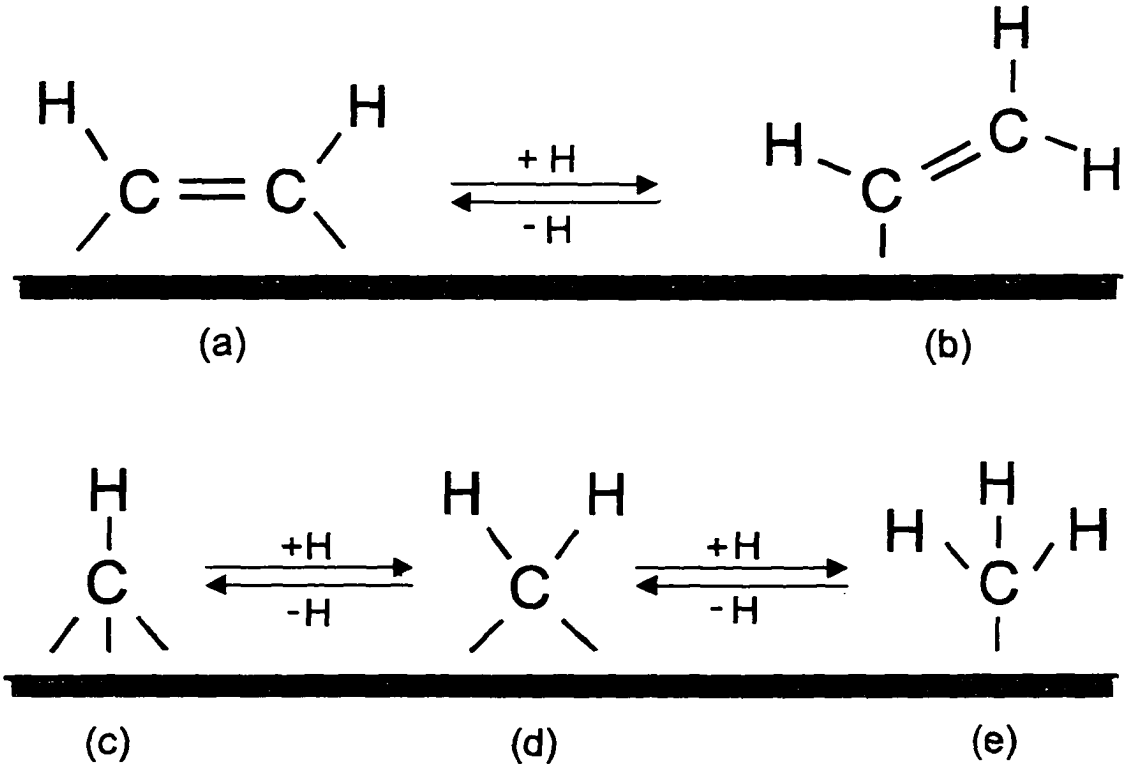

Figure 5.3 Plausible hydrocarbon species adsorbed on Cu(100) after low-energy ion irradiation in ethylene at room temperature.

Reproduced with permission of the copyright owner. Further reproduction prohibited without permission.

Table 5.1 Comparison of vibrational frequencies (cm^{-1}) of the observed species on Cu(100) at room temperature obtained by ion irradiation in C_2H_4 at 200 eV (this work) with those obtained by molecular adsorption at 80 K and those for C_2H_4 and CH_2 group in the gas phase. Values for the deuterated analogs are given in parentheses.

Mode	This work	C_2H_4/Cu(100) at 80 K (Ref. 5)	C_2H_4 (Ref. 9)	CH_2 (Ref. 12)
C–H stretch	2944-3033 (2196-2276)	2984 (2229)[b]	3009 (2245)	2990 (2241)[a] 2932 (2145)[b]
C=C stretch	1392 (1384)	1553 (1416)	1617 (1520)	-
CH_2 scissors	1392 (1086)	1287 (949)	1336 (981)	1447 (1103)
Out-of-plane bend	764 (547)[c]	901 (676)	949 (660)	1267 (996) wag 1213 (877) twist
CH_2 rock	-	-	-	875 (668)

[a] asymmetric stretch; [b] symmetric stretch; [c] part of a broad feature.

configuration of the ethen-1,2-diyl radical (H C C H) shown in Figure 5.3a can be regarded as a resonance structure of the single-σ bonding one of the vinyl (ethenyl, $-C_2H_3$) radical with the loss of a hydrogen atom (Figure 5.3b). Similarly, the "bridge" configuration of the methylene ($>CH_2$) radical (Figure 5.3d) together with the gain or loss of an adsorbed H atom may be considered as a resonance structure of the atop configuration of the methyl ($-CH_3$) radical (Fig. 3e) or that of the methine ($\succ$CH) radical (Figure 5.3c) (likely in a four-fold hollow site), respectively. Since the C–H stretching frequencies for the different adsorption configurations are quite close to one another [12], the broadness of the observed HREELS features precludes us from unambiguously identifying the nature of the adsorbed hydrocarbon species, observed in the aforementioned and all of the low-energy ethylene ion irradiation experiments (discussed below) in the present work. Indeed, the adsorption of a combination of the aforementioned species (Figure 5.3) is likely and could account for the observed broad peaks (e.g, that at 2944 cm^{-1}). Adsorption of different hydrocarbon fragments at different adsorption sites may also contribute to the observed broad features. It should be noted that other structures including vinylidene (ethen-1,1-diyl, $\succ CCH_2$) and

Reproduced with permission of the copyright owner. Further reproduction prohibited without permission.

acetylide (≻CCH), observed on Pt(111) and related transition metal surfaces [1], are less likely on a (100) fcc surface, though these structures cannot be ruled out from our data [13].

When the sample was annealed to 370 K (Figure 5.1b), the band at 764 cm^{-1} became sharper and more evident while the relative intensities of the other two bands were reduced. The center of the band at 2944 cm^{-1} (Figure 5.1a) was also shifted to 2976 cm^{-1} (Figure 5.1b). Upon further annealing the sample to 470 K (Figure 5.1c), the peak at 764 cm^{-1} remained strong while the band at 1392 cm^{-1} became very weak. The band at 2976 cm^{-1} (Figure 5.1b) was reduced to a small peak at 3033 cm^{-1} (Figure 5.1c). Only the peak at 764 cm^{-1} remained evident after the 570 K anneal (Figure 5.1d), and all the peaks were removed after further annealing to 670 K (Figure 5.1e). These changes with increasing annealing temperature indicate that the adsorbed hydrocarbon species underwent decomposition at different temperatures. At 470 K (Figure 5.1c), only C–H stretching, C=C stretching and C–H out-of-plane bending modes are clearly discernible. Among the five proposed hydrocarbon species shown in Figure 5.3, only the ethen-1,2-diyl radical has just these three modes, which suggests that other adsorbed species decomposed at a temperature below 470 K. This assignment is also consistent with the apparent shift in the C–H stretching frequency from 2944 cm^{-1} to 3033 cm^{-1} upon annealing because the C–H stretching frequency in the ethen-1,2-diyl radical is generally higher than that of other species [12].

The decomposition of hydrocarbon species is also supported by the TPD results shown in Figure 5.4. Due to the relatively high hydrogen background in our chamber, the TPD experiments were performed on the deuterated sample used in Figure 5.2a. Only recombinative desorption of deuterium (corresponding to mass 4) was found over the temperature range 360-660 K. Because no other deuterated hydrocarbon species was detected in the TPD study, deuterated hydrocarbon species must have undergone complete decomposition on the surface in this temperature range. The multiple-peak structure of the mass-4 TPD profile in Figure 5.4 suggests the presence of many desorption phases (pathways) for D_2, indicating different sources of D atoms as a result of thermal decomposition of the adsorbed hydrocarbon species. The desorption of embedded hydrogen due to ion implantation could also contribute to the observed desorption profile. TPD results

Reproduced with permission of the copyright owner. Further reproduction prohibited without permission.

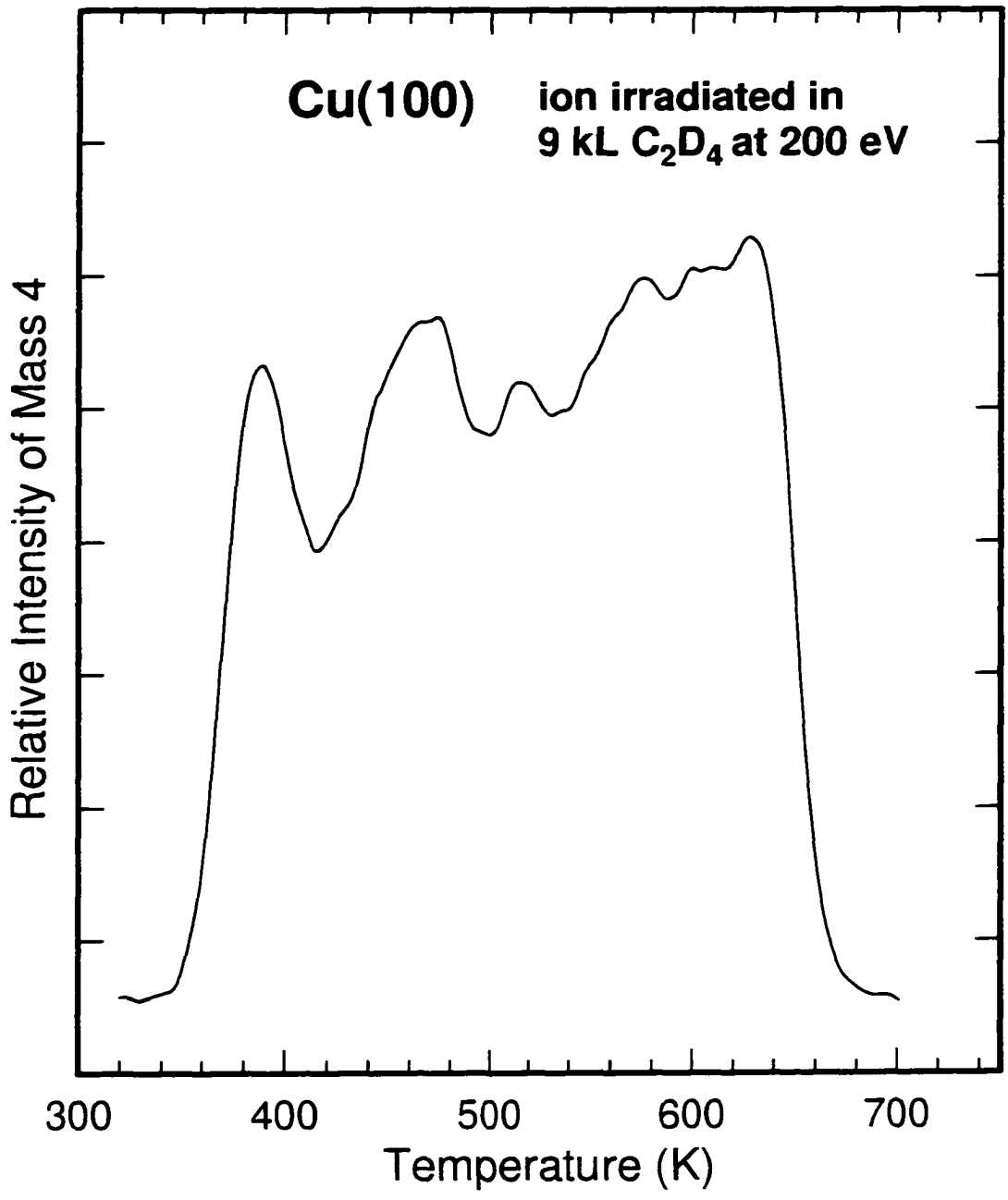

Figure 5.4 Temperature programmed desorption profile of the parent ion (mass 4) of D_2 for Cu(100) ion-irradiated in 9 kL of C_2D_4 at 200 eV impact energy.

Reproduced with permission of the copyright owner. Further reproduction prohibited without permission.

have also been obtained for different ion dosage and at different impact energies (not shown). In these cases, the overall intensities of the desorption profiles were found to be different while the temperature range over which desorption occurred remained unchanged.

5.3 Low-energy ethylene ion interactions with N-pre-covered Cu(100)

Although N_2 does not readily adsorb on Cu(100) at RT, a c(2×2)N overlayer can be obtained by low-energy electron or ion irradiation in N_2 at RT followed by annealing to 550 K. The nitrogen atoms were reported to adsorb in the four-fold hollow sites [14]. Details of the adsorption and desorption of atomic nitrogen on Cu(100) have been given in Chapter 4.

Figure 5.5 shows the HREELS spectra of a c(2×2)N/Cu(100) sample after ion irradiation in 5 kL of ethylene followed by annealing to different temperatures. Evidently, the broad band at 2944 cm^{-1} corresponding to the C–H stretch observed in Figure 5.1a is replaced by a prominent and much sharper peak at 3379 cm^{-1} in Figure 5.5a, which cannot be assigned to contributions related to hydrocarbon species due to its significantly higher frequency. Also shown in Figure 5.5a are two weak, broad features at 2091 cm^{-1} and 2735 cm^{-1}. Furthermore, the broad features below 1500 cm^{-1} cannot be clearly resolved. The corresponding EELS spectra for an isotope substitution experiment are shown in Figure 5.6. The peak at 3379 cm^{-1} in Figure 5.5a has an isotope-shifted analog at 2445 cm^{-1} in Figure 5.6a, while the peak at 2091 cm^{-1} in Figure 5.5a remains at essentially the same position in the deuterated ethylene case (Figure 5.6a). The vibrational frequencies of the features obtained for the ion irradiation case and their tentative assignments are compared with the corresponding features for gaseous HCN [14], gaseous HNC [14], HCN/Cu(111) [15], and HCNH/W(100) [16] in Table 5.2.

In accord with the earlier studies [15,17] the peak at 2091 cm^{-1} (Figure 5.5) can clearly be assigned to a C≡N stretching mode in a cyanide related adsorbate. The peak at 2735 cm^{-1} in Figure 5.5a could be assigned to a "perturbed" C–H stretch in the hydrocarbon fragments produced by ion irradiation (Figure 5.3). The assignment for the peak at 3379 cm^{-1} (Figure 5.5) is however less clear and there are three possibilities. The first possibility is C–H stretch in a hydrogen cyanide (HCN) adsorbate. In keeping with the representative

Reproduced with permission of the copyright owner. Further reproduction prohibited without permission.

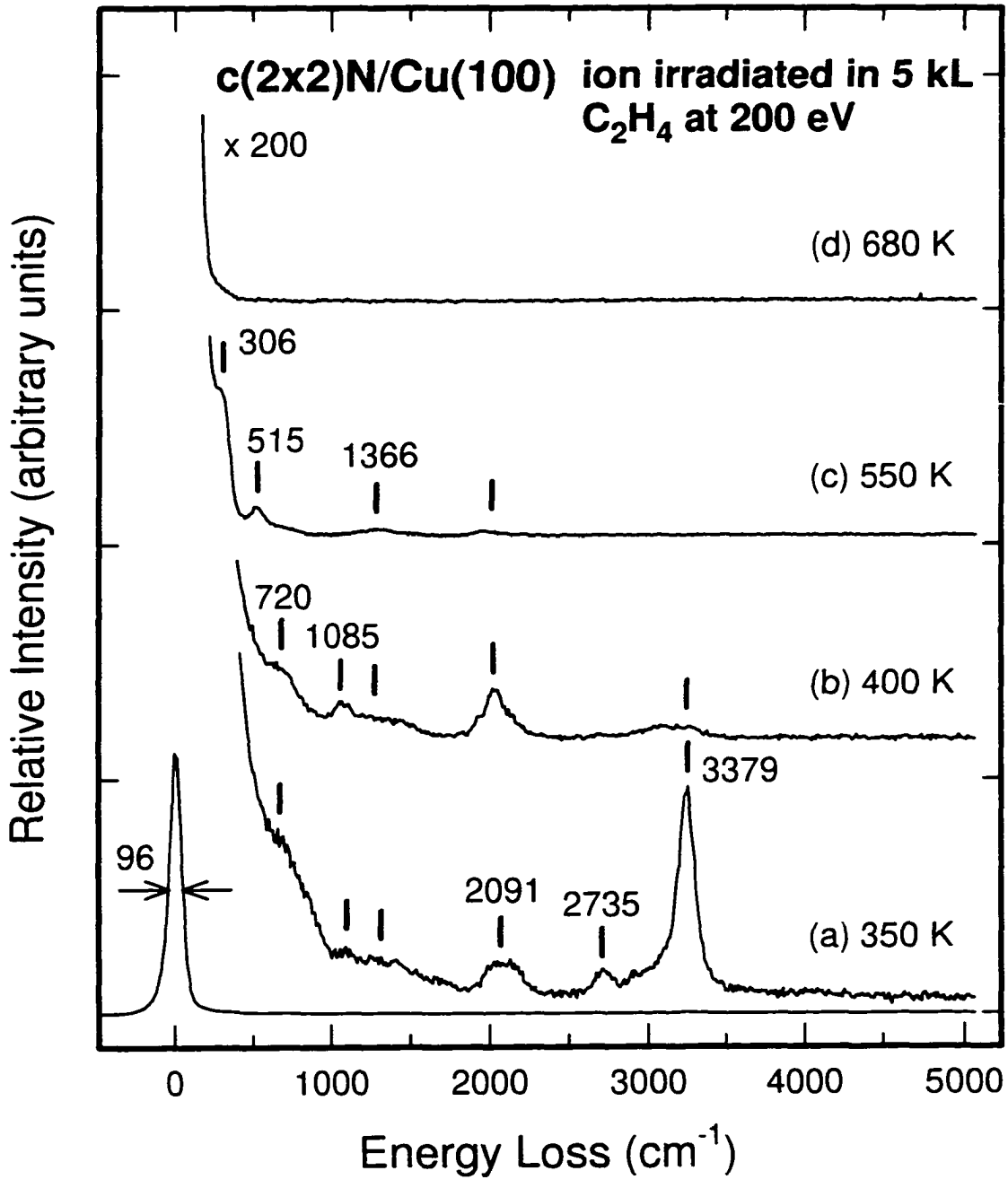

Figure 5.5 Vibrational electron energy loss spectra for a nitrogen-precovered Cu(100) surface ion-irradiated at 200 eV impact energy in 5 kL of C_2H_4 and annealed to (a) 350 K, (b) 400 K, (c) 550 K, and (d) 680 K.

Reproduced with permission of the copyright owner. Further reproduction prohibited without permission.

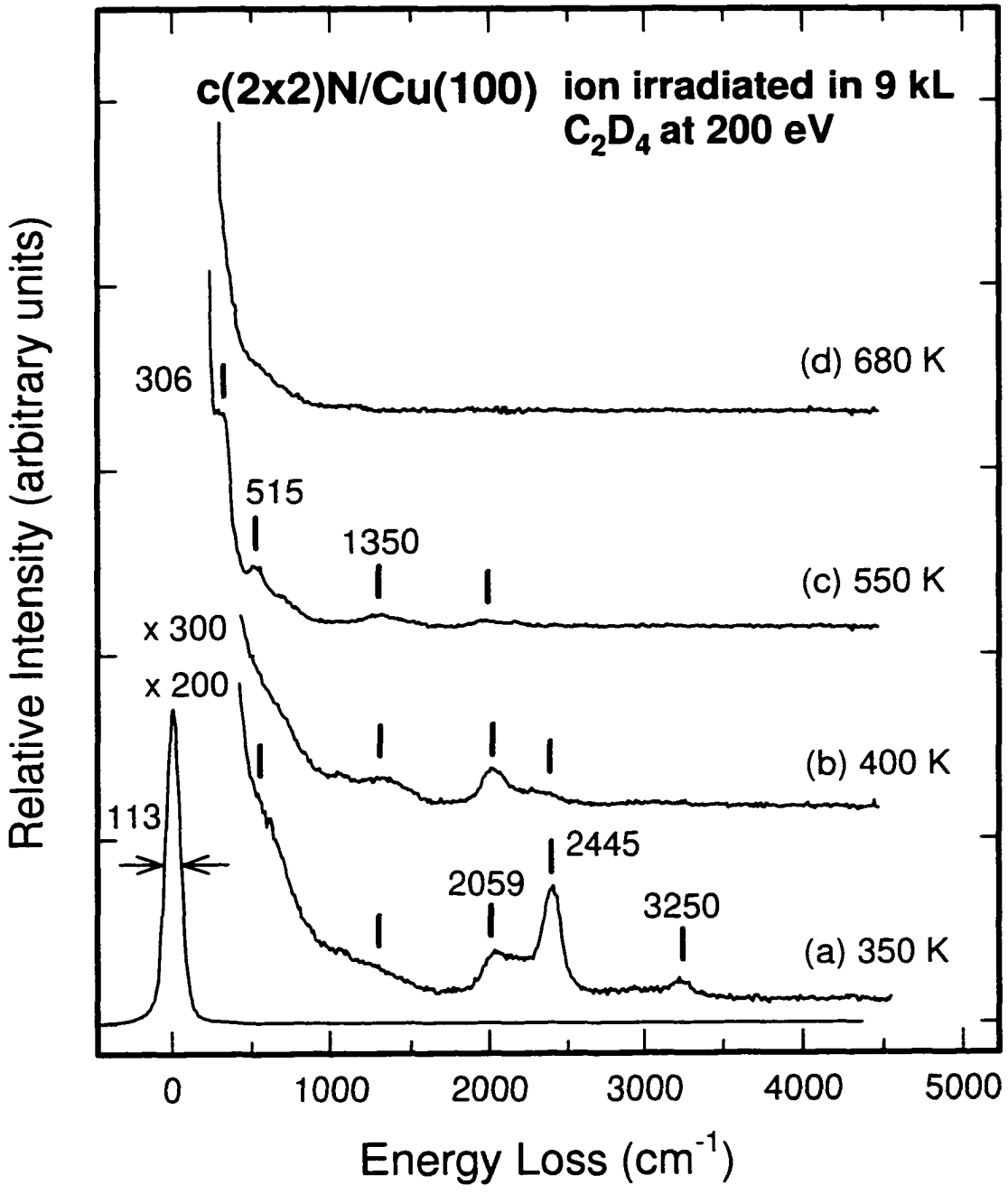

Figure 5.6 Vibrational electron energy loss spectra for a nitrogen-precovered Cu(100) surface ion-irradiated at 200 eV impact energy in 9 kL of C_2D_4 and annealed to (a) 350 K, (b) 400 K, (c) 550 K, and (d) 680 K.

Reproduced with permission of the copyright owner. Further reproduction prohibited without permission.

Table 5.2 Comparison of vibrational frequencies (cm^{-1}) of the observed species obtained on N-precovered Cu(100) by ion irradiation in C_2H_4 at 200 eV (this work) with those for gaseous HCN, gaseous HNC, HCN/Cu(111), and HCNH/W(100). Values for the corresponding matrix isolated samples of HCN and HNC are given in parentheses.

Mode	This work	HCN (Ref. 14)	HNC (Ref. 14)	HCN/Cu(111) (Ref. 15)	HCNH/W(100) (Ref. 16)
N–H stretch	3379	-	3842 (3653)	-	3360
C–H stretch	2735	3441 (3312)	-	3121	2940
C≡N stretch	2091	2127 (2097)	2067 (2029)	2068	-
C=N stretch	-	-	-	-	1400
C=C stretch	1366	-	-	-	-
XCN bend	515[a]	727 (714)[b]	490 (477)[b]	821[b]	-
Cu–N stretch	306	-	-	-	-

[a] X = C or N; [b] X = H.

vibrational frequencies reported for the common hydrocarbon groups [12], a C–H stretching frequency as high as 3330 cm^{-1} can only be found in the(≡C–H) radical. Because it is unlikely that carbon forms a triple bond to a single Cu atom directly, the bonding to Cu must involve a N atom through the formation of H–C≡N (hydrogen cyanide). In this model, the energy loss feature observed at 2091 cm^{-1} can be assigned as a C≡N stretch [15]. Although the C–H stretching frequency for HCN has been found to be 3312 cm^{-1} in a matrix-isolation experiment and 3441 cm^{-1} in the gas phase [14], it usually occurs at a lower frequency for a HCN adsorbate on a metal surface. For example, the C–H stretch was reported at 3145 cm^{-1} for condensed HCN [18], 3121 cm^{-1} for HCN/Cu(111) [15], and 2940 cm^{-1} for HCNH/W(100) [16]. The presently observed frequency at 3379 cm^{-1} may therefore be too high to be assigned as a C–H stretch in an adsorbed HCN molecule. The second possible assignment for this peak is the N–H stretching mode in a hydrogen isocyanide (HNC) adsorbate. Although the N–H stretching frequency for matrix–isolated HNC is 3653 cm^{-1} and that for gaseous HNC is 3842 cm^{-1} [14,17], it has also been observed at 3360 cm^{-1} for a HCNH intermediate on a W(100) surface [16]. These frequencies are quite similar to that

Reproduced with permission of the copyright owner. Further reproduction prohibited without permission.

observed in the present work (3379 cm^{-1}). The third possibility is that the NH_x (x = 1-3) and cyanide (C≡N) radicals coexist separately on the surface, which could also give rise to the peaks at 3379 cm^{-1} for N–H stretch and 2091 cm^{-1} for C≡N stretch. Among the possible NH_x species (NH, NH_2 and NH_3), the most likely adsorbate is the NH radical because of the high activation barriers in the hydrogenation reaction pathways from NH to NH_2 and to NH_3 [19]. Furthermore, although the N–H stretching frequencies for the three possible NH_x species could locate between 3300 cm^{-1} and 3400 cm^{-1} [20], the presence of NH_2 or NH_3 is expected to produce a broader N–H feature due to additional asymmetric stretching modes. It is therefore unlikely that the observed single peak at 3379 cm^{-1} (Figure 5.5a) would contain contributions from the NH_2 or NH_3 species. In this model, the peak at 3379 cm^{-1} could be assigned to a N–H stretch with NH in a four-fold hollow site while the peak at 2091 cm^{-1} could be assigned to a C≡N stretch with CN in an upright position [21]. Among the three possible assignments for the 3379 cm^{-1} peak, we favour the last model involving the coexistence of CN and NH radicals on the surface because additional energy is required for the formation of HCN or HNC in the other models. The peak at 3379 cm^{-1} can apparently be removed at a lower annealing temperature (400 K, Figure 5.5b) than the peak at 2091 cm^{-1}, which indicates that breaking the N–H bond requires less energy than breaking the Cu–CN bond. As discussed below, the desorption of NH radical was not observed in the TPD experiments, indicating thermal dissociation of NH.

After the sample was annealed to 550 K, the peak at 515 cm^{-1} became more evident in both samples prepared with normal ethylene ions (Figure 5.5c) and deuterated ethylene ions (Figure 5.6c). This feature could be attributed to a XCN bending mode, where X is a neighboring C or N atom [22]. This proposed bonding picture is similar to the direct interaction model, involving as-formed CO stabilized by neighboring O or C-containing species, discussed Chapter 3. The weak broad feature at 1366 cm^{-1}, which can clearly be seen in Figure 5.5c (and Figure 5.6c), could be assigned to a C=C stretch as discussed in Section 5.2. The shoulder at 306 cm^{-1} found in both Figure 5.5c and Figure 5.6c is due to the Cu–N stretch [13]. Finally, all the energy loss features were removed after the samples were annealed to 680 K (Figure 5.5d and Figure 5.6d).

Figure 5.7 shows the corresponding TPD profiles for the deuterated sample used in

Reproduced with permission of the copyright owner. Further reproduction prohibited without permission.

Figure 5.6. Desorption profiles for mass 4 (corresponding to D_2), mass 28 and 14 (corresponding to N_2), and mass 26 (corresponding to CN) were recorded. Mass 4 came from recombinative desorption of deuterium atoms which originated from thermally dissociated N–D radicals and embedded deuterium atoms. The maximum CN desorption observed in the TPD experiment occurred at ~680 K, which is inconsistent with the temperature range (350-550 K) over which the peak reduction of the C≡N stretch occurred (Figure 5.6a-c). This indicates that the CN species desorbed at 680 K in the TPD experiments came from recombinative desorption of surface C and N atoms. The disappearance of the CN features in the EELS spectra below 550 K can be explained by the decomposition of the as-formed CN radical. Desorption of mass 28 came from recombinative desorption of the N atoms in the c(2×2)N/Cu(100) substrate. It should also be noted that no HCN or HNC (mass 27) nor DCN or DNC (mass 28) species could be found in the TPD experiments for the samples used in Figure 5.5 and Figure 5.6 respectively, which supports the model of separate adsorption of CN and NH (ND) radicals instead of that of HCN (DCN) or HNC (DNC) on the surface. The relative intensity of hydrogen to nitrogen desorption is found to increase with increasing ethylene ion dosage or impact energy, which indicates that the nitrogen species could be displaced from the surface by ethylene ion irradiation.

5.4 Summary

In the present work, we have studied the adsorption induced by low-energy ion irradiation in ethylene without mass selection at RT on clean and N-precovered surfaces of Cu(100) by HREELS and TPD techniques. Together with the work on O-precovered Cu(100) (Chapter 3, Section 3.5), we demonstrated the effectiveness of low-energy ion irradiation in generating stabilized surface species, which cannot be obtained otherwise by normal gas-surface thermal reactions. By using standard surface analysis techniques such as HREELS and TPD, we found the coexistence of several adsorbates under different surface conditions at RT. In particular, the adsorption of different hydrocarbon species (Figure 5.3) on a clean Cu(100) surface could be produced *in situ* by low-energy ion irradiation in ethylene. These hydrocarbon species underwent decomposition upon annealing and their

Reproduced with permission of the copyright owner. Further reproduction prohibited without permission.

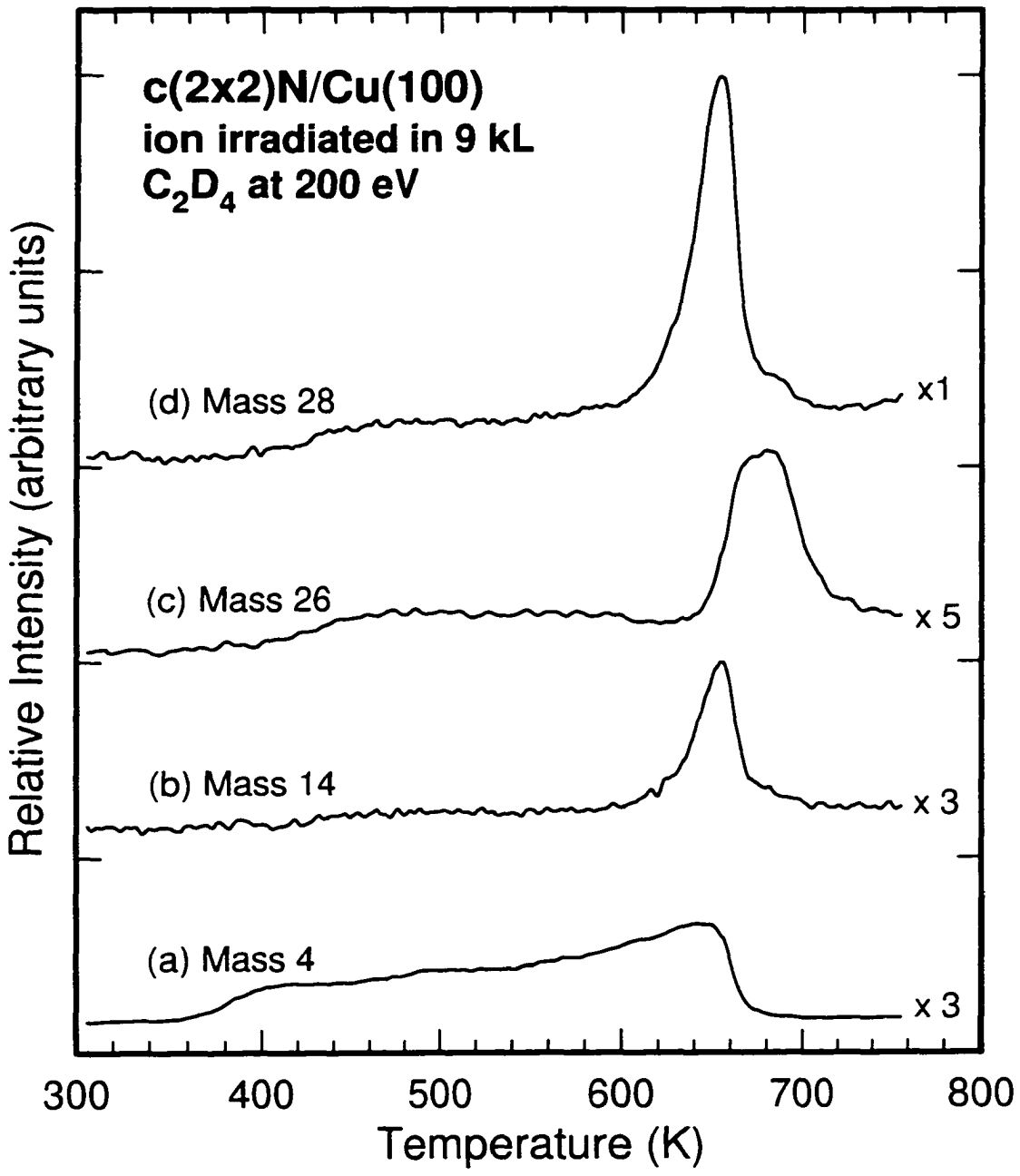

Figure 5.7 Temperature programmed desorption profiles of the parent ions of (a) D_2 (mass 4), (c) CN (mass 26) and (d) N_2 (mass 28), and of mass 14 (corresponding to the N atoms dissociated from N_2 in the ionizer) for a nitrogen-precovered Cu(100) surface ion-irradiated in 9 kL of C_2D_4 at 200 eV impact energy.

Reproduced with permission of the copyright owner. Further reproduction prohibited without permission.

characteristic HREELS features could be observed at a temperature as high as ~600 K. In the case of an O-precovered surface (Chapter 3), we observed the presence of both red-shifted and blue-shifted C–O stretching modes, which are attributed to as-formed CO stabilized by direct interactions with, respectively, nearby O and C-containing species generated by irradiation with a heavy dose of low-energy ethylene ions. In the case of a N-precovered surface, surface nitrogen atoms were found to react with the hydrocarbon fragments generated by ion irradiation to produce CN and NH (containing) species on the surface. The reactions of ethylene ions with a N-precovered Cu(100) surface therefore appear to be quite different from those with an O-precovered surface (Chapter 3). The formation of NH (containing) species indicates that the hydrocarbon fragments must undergo some forms of dissociation to produce H on the N-covered surface in order for the subsequent reaction(s) with surface nitrogen to occur. In all cases studied in the present work, low-energy ion irradiation played a crucial role in both the formation and stabilized adsorption of these surface species.

5.5 References

[1] G. A. Somorjai, "Introduction to Surface Chemistry and Catalysis", Wiley-Interscience, New York (1994).

[2] D. A. King and D. P. Wordruff (eds.), "The Chemical Physics of Solid Surfaces and Heterogeneous Catalysis", Vol. **4**, Elsevier, New York (1982) Chapter 7, p. 217.

[3] F. Zaera and R. B. Hall, Surf. Sci. **180**, 1 (1987).

[4] N. Sheppard, J. Electron Spectrosc. and Relat. Phenom. **38**, 187 (1986).

[5] C. Nyberg, C. G. Tengstal, and S. Andersson, Chem. Phys. Lett. **87**, 87 (1982).

[6] D. L. Smith, "Thin Film Deposition Principles and Practice", McGraw-Hill, New York (1995), Chapter 8.

[7] C. C. Cheng, P. A. Taylor, R. M. Wallace, H. Gutleben, L. Clemen, M. L. Colaianni, P. J. Chen, W. H. Weinberg, W. J. Choyke, and J. Y. Yates Jr., Thin Solid Films **225**, 196 (1993).

[8] "Eight Peak Index of Mass Spectra", Vol. **1**, Mass Spectrometry Data Center, Aldermaston (1974).

Reproduced with permission of the copyright owner. Further reproduction prohibited without permission.

[9] G. Herzberg, "Molecular Spectra and Molecular Structure: Infrared and Raman Spectra of Polyatomic Molecules", Vol. **2**, Van Nostrand, Toronto (1945).

[10] S. Lehwald and H. Ibach, Surf. Sci. **89**, 499 (1979).

[11] W. Widdra, C. Huang, S. I. Yi, and W. H. Weinberg, J. Chem. Phys. **105**, 5605 (1996).

[12] H. Ibach and D. L. Mills, "Electron Energy Loss Spectroscopy and Surface Vibrations", Academic, New York (1982).

[13] L.L. Kesmodel, G.D. Waddill, and J.A. Gates, Surf. Sci. **138**, 464 (1984).

[14] T. J. Lee, C. E. Dateo, B. Gazdy, and J. M. Bowman, J. Phys. Chem. **97**, 8937 (1993).

[15] M.E. Kordesch, W. Feng, W. Stenzel, M. Weaver, and H. Conrad, J. Electron Spectrosc. Relat. Phenom. **44**, 149 (1987).

[16] J. G. Serafin and C. M. Friend, J. Phys. Chem. **92**, 6694 (1988). See also: C. M. Friend and J. G. Serafin, J. Chem. Phys. **88**, 4037 (1988).

[17] D. E. Milligan and M. E. Jacox, J. Chem. Phys. **39**, 712 (1963).

[18] H. B. Friedrich and P. F. Krause, J. Chem. Phys. **59**, 4942 (1977).

[19] N. Takehiro, K. Mukai, and K. Tanaka, J. Chem. Phys. **103**, 1650 (1995).

[20] I. C. Bassignana, K. Wagemann, J. Kuppers, and G. Ertl, Surf. Sci. **175**, 22 (1986).

[21] K. Hermann, W. Moller, and P.S. Bagus, J. Electron Spectrosc. Relat. Phenom. **39**, 107 (1986).

[22] A. J. Capote, A.V. Hamza, N. D. S. Canning, and R. J. Madix, Surf. Sci. **175**, 445 (1986).

Reproduced with permission of the copyright owner. Further reproduction prohibited without permission.

Chapter 6

HREELS STUDY OF CARBON AND AMBIENT-GAS CONTAMINATION ON Si(111)7×7

6.1 Introduction

The surface chemistry of semiconductors (especially silicon) has continued to be one of the most extensively studied subjects in surface science because of its wide-ranging applications in electronics, telecommunications, and computer industries [1]. The performance of modern electronic devices is very much determined by the properties of interfaces (particularly their geometrical and electronic structures), which are strongly dependent on the preparation details of the fabrication processes and are very sensitive to contamination [2]. Compared to metal surfaces, a semiconductor surface has more highly localized electronic states (dangling bonds) and greater surface corrugation, which give rise to significantly different surface chemistry. Studies of the adsorption properties on semiconductor surfaces can therefore provide important information on the modification of the electronic structure caused by adsorption [2].

Si(111) is a popular semiconductor surface with a unique 7×7 reconstruction structure. The most generally accepted model for the 7×7 unit cell is the dimer-adatom-stacking-fault (DAS) model [3], reproduced in Figure 6.1. In this model, the surface is composed of periodically arranged rhombohedral 7×7 unit cells with their long and short diagonals being 46.4 and 26.9 Å, respectively [4,5]. There are 12 adatoms in the topmost layer and 6 rest-atoms at the second level of the reconstructed surface, each contributing a dangling bond. Along with the dangling bond from a corner hole atom at the fourth layer, there are a total of 19 dangling bonds in one unit cell, reduced from 49 dangling bonds if the surface is unreconstructed. Each side of the triangular halves is also bounded by three Si-Si dimers. The rest-atoms are generally believed to be more reactive than the adatoms, with the center adatoms being more reactive than the corner adatoms [6]. Between the two halves of the unit cell, the faulted half (the half on the left hand side in Figure 6.1) is found to be more reactive than the unfaulted half (right hand side) [7].

Reproduced with permission of the copyright owner. Further reproduction prohibited without permission.

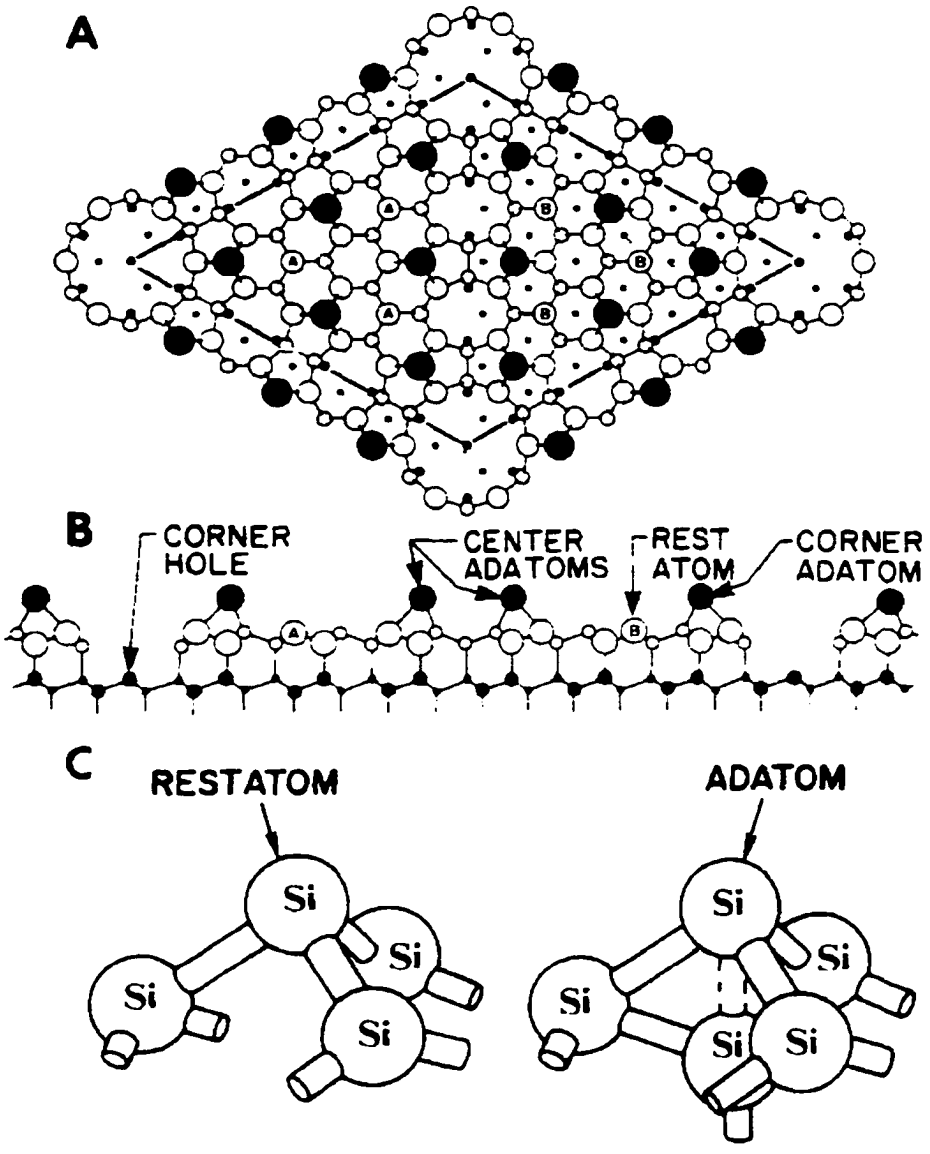

Figure 6.1 (A) Top view of the dimer-adatom-stacking fault (DAS) model of Si(111)7×7. Atoms in the (111) layer at increasing depth are indicated by circles of decreasing size. (B) Side view along the diagonal of the unit cell. (C) The structure and bonding at the rest-atom and adatom sites (After Ref. 3).

Reproduced with permission of the copyright owner. Further reproduction prohibited without permission.

The contamination problem with silicon remains one of the important issues in device fabrication and semiconductor materials processing [1]. Although the adsorption of common gases, such as oxygen [8,9], hydrogen [10,11], water [12,13], and hydrocarbons [14,15], on clean Si(111)7×7 has been studied extensively, the results are often inconsistent and incomplete. Furthermore, there are no studies on the coadsorption of these gases on clean or carbon-contaminated surfaces. These studies would, however, provide valuable information and better understanding of the bonding geometry and surface reactions involved in the coadsorption process, which are of immense technological interest. In addition, contamination by or coadsorption with the ambient gas commonly found in standard stainless steel UHV chambers employed not only in almost all the surface science work but also in manufacturing facilities (such as growth chambers, etc.) is often unavoidable. Better understanding of the effects of the ambient gas on surface adsorption and reactions is therefore very important for correctly interpreting the experiment results and effectively improving the industrial procedures.

In this chapter, we first present an investigation on carbon contamination on Si(111)7×7 by using HREELS and AES, followed by a study on the adsorption of oxygen and ambient gas on the carbon-contaminated surface, in order to probe the effects of carbon contamination. Furthermore, the coadsorption of oxygen and the ambient gas will also be examined. Specifically, the goal of this study is to investigate the effects of the common contaminants on the adsorption properties of oxygen and water on Si(111)7×7.

6.2 Common contamination on Si(111)7×7

6.2.1 Carbon contamination

Carbon is one of the most commonly found contaminants on the Si(111) surface. It can be deposited onto a clean silicon surface when exposed to ambient gas in a UHV chamber. The presence of surface C contaminant can be easily detected by HREELS due to the characteristic Si–C stretching vibration at 800 cm^{-1} [8]. On one hand, carbon contamination is an annoying problem for the preparation of a clean surface because it could affect the adsorption properties of other adsorbates. Its prominent feature at ~800 cm^{-1} in a HREELS spectrum could also obscure other neighboring features characteristic of other

Reproduced with permission of the copyright owner. Further reproduction prohibited without permission.

adsorbates in the important 700-1000 cm^{-1} range. On the other hand, the deposition of carbon on a silicon surface provides a natural means of growing silicon carbide or amorphous carbon films, which are of interest to a number of industrial applications.

The AES spectra shown in Figure 6.2 depict the contamination level of a "dirty" Si(111) surface after successive cleaning cycles. It should be noted that a 4-grid retarding-field-analyzer was used for the Auger measurements (Chapter 2). Before cleaning, the AES spectrum of the Si(111) surface exhibited large amounts of carbon and oxygen (Figure 6.2a) and no LEED pattern was observed. After two cleaning cycles, each of which consisted of 30 minutes of Ar^+ sputtering and annealing to 1200 K (see Section 2.1), the oxygen contaminant was removed, while carbon remained evident (Figure 6.2b). After four cleaning cycles, the carbon contamination level dropped to a level not detectable by our AES spectra (Figure 6.2c). A sharp 7×7 LEED pattern could also be obtained by simply flashing the sample rapidly to a higher temperature (~1270 K). However, the corresponding HREELS spectrum shown in Figure 6.3 for the resulting surface (Figure 6.2c) still indicates a strong peak at 845 cm^{-1}, which can be assigned to a Si–C stretching mode [15,16]. After a few more additional cleaning cycles, the carbon contamination dropped eventually below the detectable level of HREELS (Figure 6.3b-c).

During annealing in the cleaning process, carbon underwent bi-directional diffusion between the surface and the bulk. Depending on the carbon concentrations on the surface and in the bulk, this diffusion would continue until a dynamic equilibrium was reached. At the beginning, the carbon concentration was high, the annealing after each sputtering step transferred some carbon from the bulk to the surface, which could then be sputtered away and the total carbon level dropped. However, when the total carbon concentration reached a sufficiently low level, the residual ambient gas in a vacuum below 1×10^{-9} Torr could cause carbon to re-deposit onto the surface during the subsequent sputtering and annealing cycles. It should be noted that outgassing the sample holder during annealing could also produce a similar effect. Although annealing could also cause some of the carbon to diffuse back into the bulk, such a process would eventually give rise to an equilibrium level of the surface carbon. It is therefore important to have a good vacuum and to design a sample holder with minimal outgassing during annealing in order to achieve an effective sample preparation.

Reproduced with permission of the copyright owner. Further reproduction prohibited without permission.

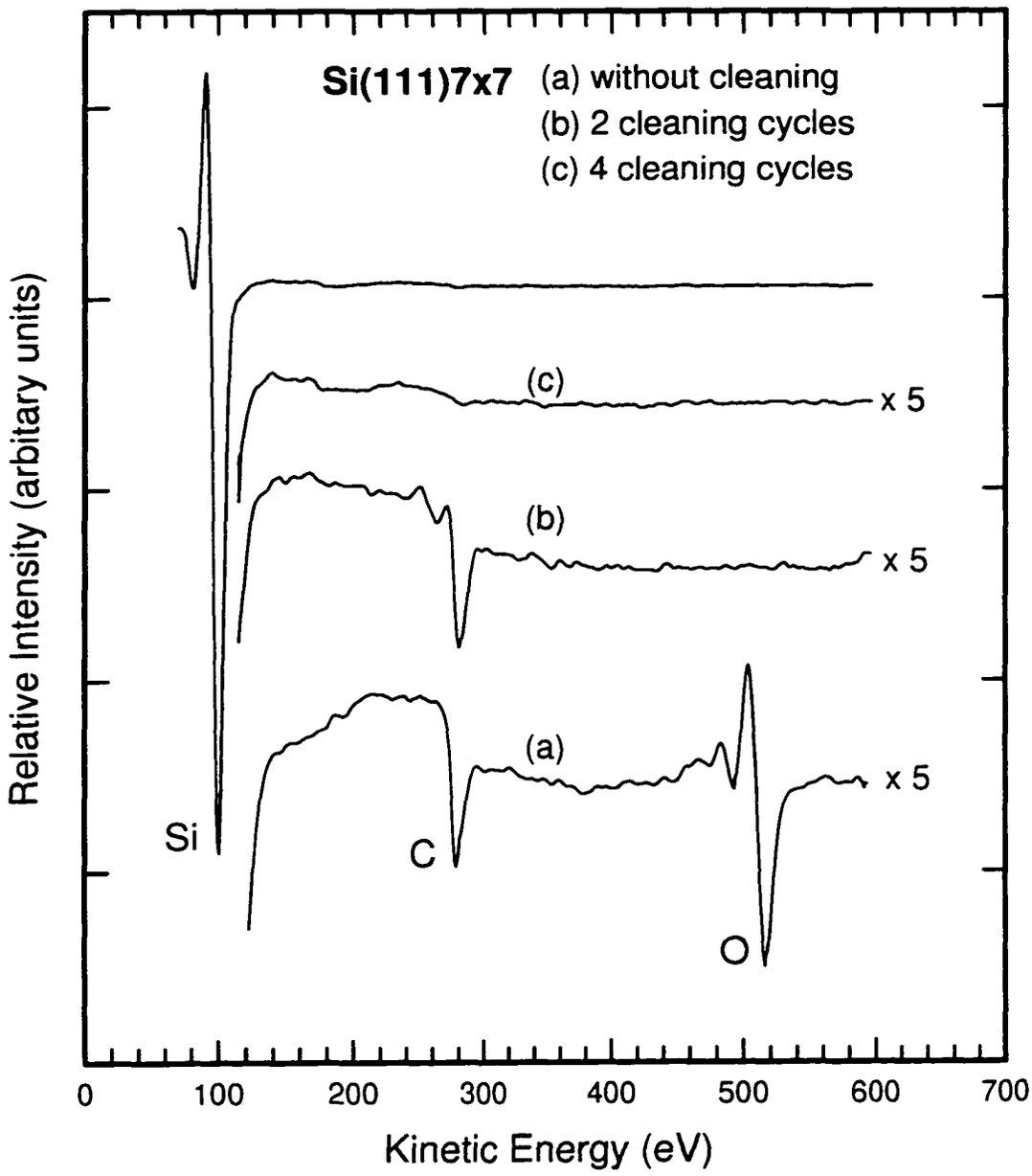

Figure 6.2 AES spectra of common contaminants on a Si(111) surface (a) without cleaning, and with (b) two and (c) four cleaning cycles (each cleaning cycle consisted of 30 minutes of Ar^+ sputtering and annealing to 1200 K).

Reproduced with permission of the copyright owner. Further reproduction prohibited without permission.

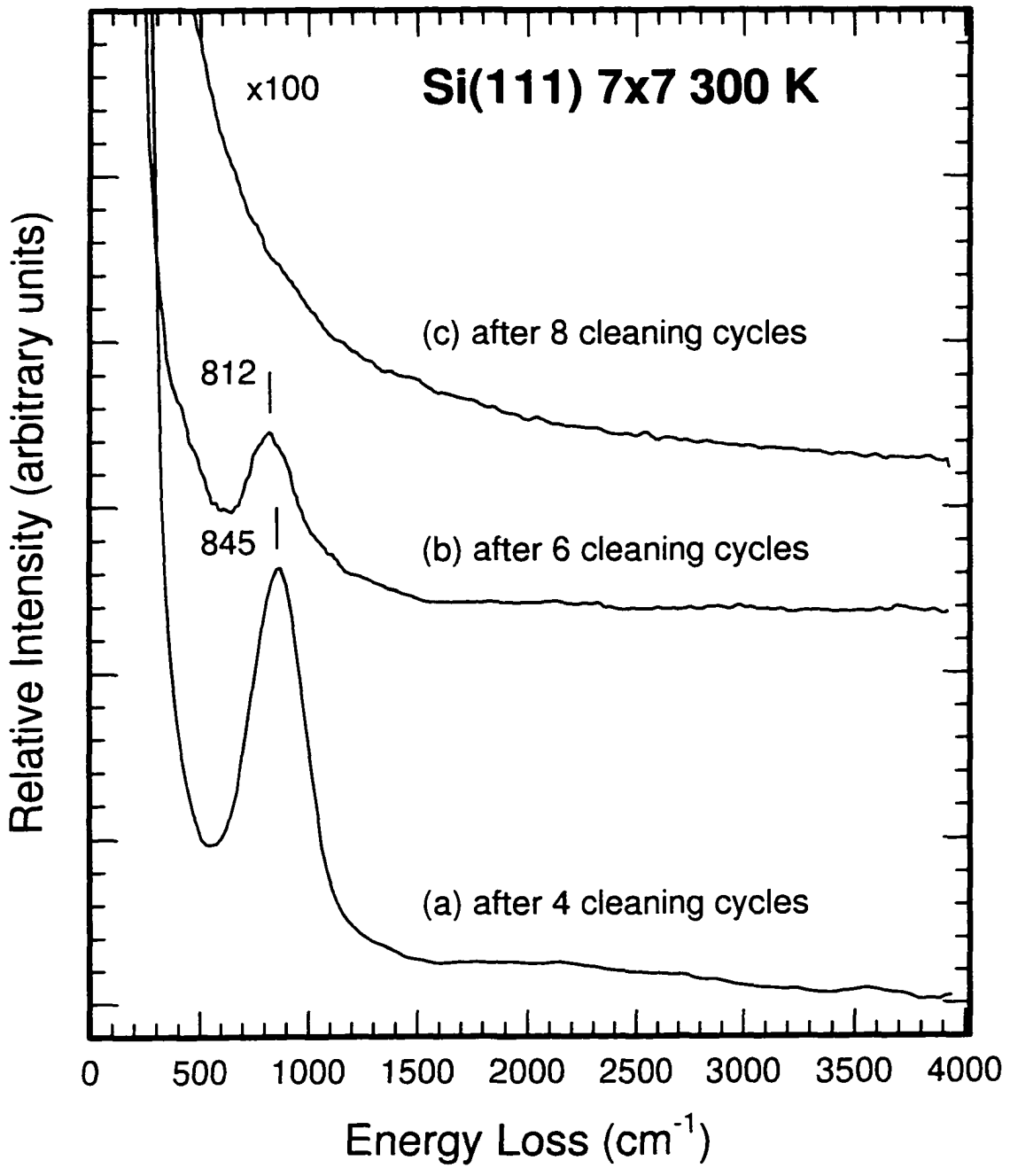

Figure 6.3 Vibrational electron energy loss spectra for residual carbon contamination on Si(111)7×7, after (a) 4, (b) 6, (c) 8 cleaning cycles (each consisting of 30 minutes Ar^+ of sputtering and annealing to 1200 K).

Reproduced with permission of the copyright owner. Further reproduction prohibited without permission.

Clearly, the presence of a 7×7 LEED pattern does not necessarily mean that the surface is totally free of carbon.

6.2.2 Contamination due to ambient gas

Unlike Cu(100), the Si(111)7×7 surface is more susceptible to contamination by the residual ambient gas in an UHV chamber. Usually the ambient gas in a standard UHV chamber (Section 2.1) consists primarily of water and hydrogen, along with oxygen, nitrogen, carbon dioxide and hydrocarbons (e.g., CH_4) present at lower concentrations. Figure 6.4 shows the cracking pattern of the ambient gas in our UHV chamber at 2×10^{-10} Torr, which indicates the presence of hydrogen (mass 1 and 2), water (mass 18 and 17), nitrogen and CO (mass 28), CO_2 (mass 44), and methane (mass 16). Molecular hydrogen and N_2 do not react with the Si(111)7×7 surface in molecular form at room temperature [10,17], while other gases (H_2O, O_2, CH_4) interact strongly with the surface. For example, the initial sticking probability of water on Si(111)7×7 is 0.23 [13] and only 2 L exposure of water was found to be sufficient to produce strong features in the HREELS spectrum by Ibach *et al.* [12]. Figure 6.5 shows a clean Si(111)7×7 surface (Figure 6.5a) in contact with the ambient gas for 10 hours (Figure 6.5b) and 24 hours (Figure 6.5c) at 2×10^{-10} Torr. The "water-related" features at 804, 2075, and 3701 cm^{-1} can be attributed to Si–OH bending, SiH stretching, and OH stretching mode, respectively [12]. The peak at 2920 cm^{-1} can be assigned to a CH stretching mode [15], which is indicative of the presence of hydrocarbons in the ambient gas. The weak features between 1000 and 1400 cm^{-1} can also be attributed to the adsorption of hydrocarbons. The characteristic oxygen feature [8] was not evident in the HREELS spectrum of the contaminated surface (Figure 6.5c), which could be due to the low relative concentration of oxygen in the chamber (Figure 6.4). It is of interest to note that even after 24 hours of exposure (Figure 6.5c), the 7×7 LEED pattern remained clear (though not as sharp as the freshly prepared Si(111)7×7 sample in Figure 6.5a). Annealing the contaminated surface to 1200 K removed most of contaminants except for a small residual amount of carbon detectable by HREELS. To completely restore the clean surface, the surface must be re-treated with repeated sputtering-annealing cycles described in Chapter 2 (Section 2.1) until no contaminant feature is detectable by HREELS.

Reproduced with permission of the copyright owner. Further reproduction prohibited without permission.

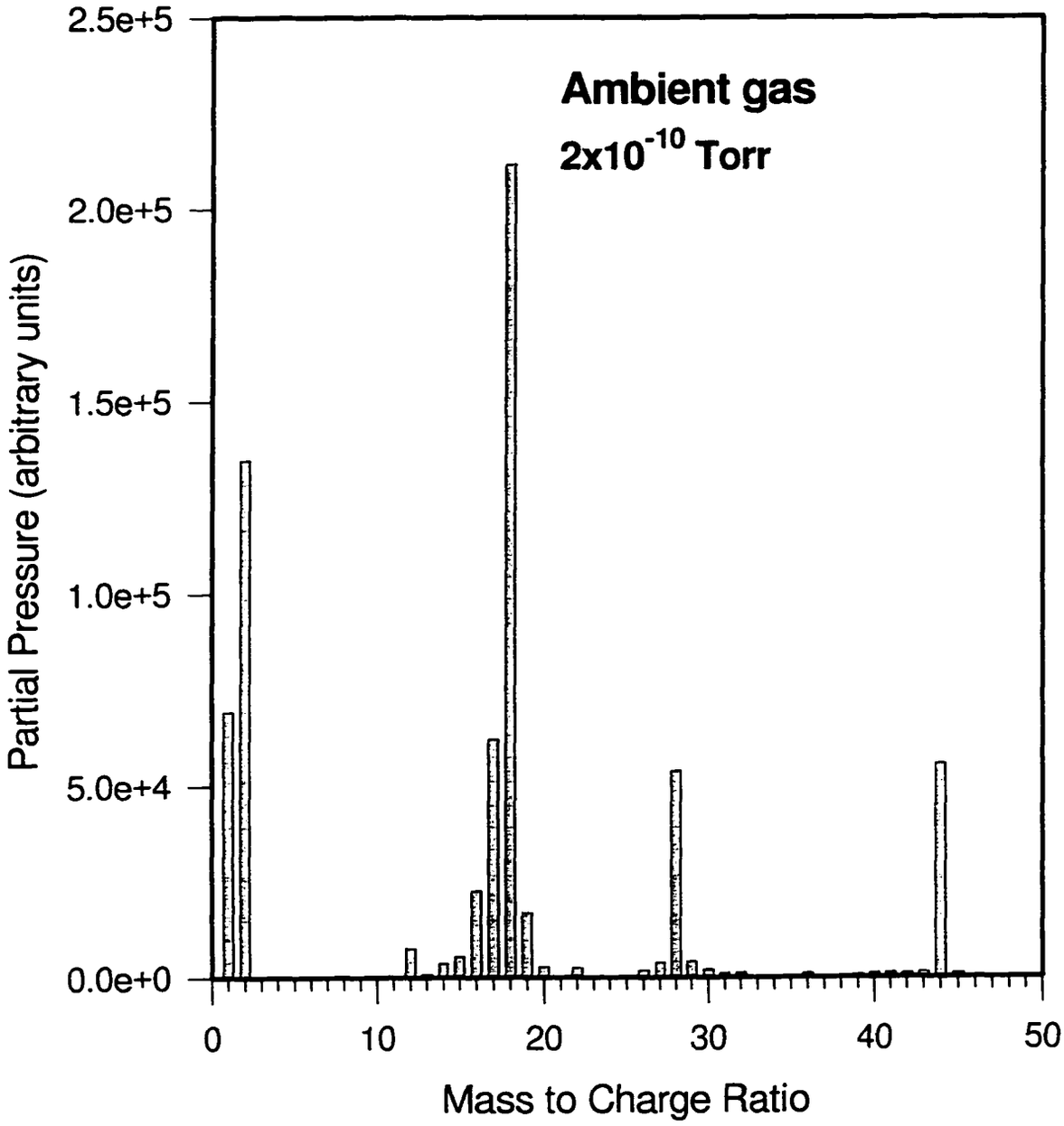

Figure 6.4 A typical mass spectrum of ambient gas at 2×10^{-10} Torr.

Reproduced with permission of the copyright owner. Further reproduction prohibited without permission.

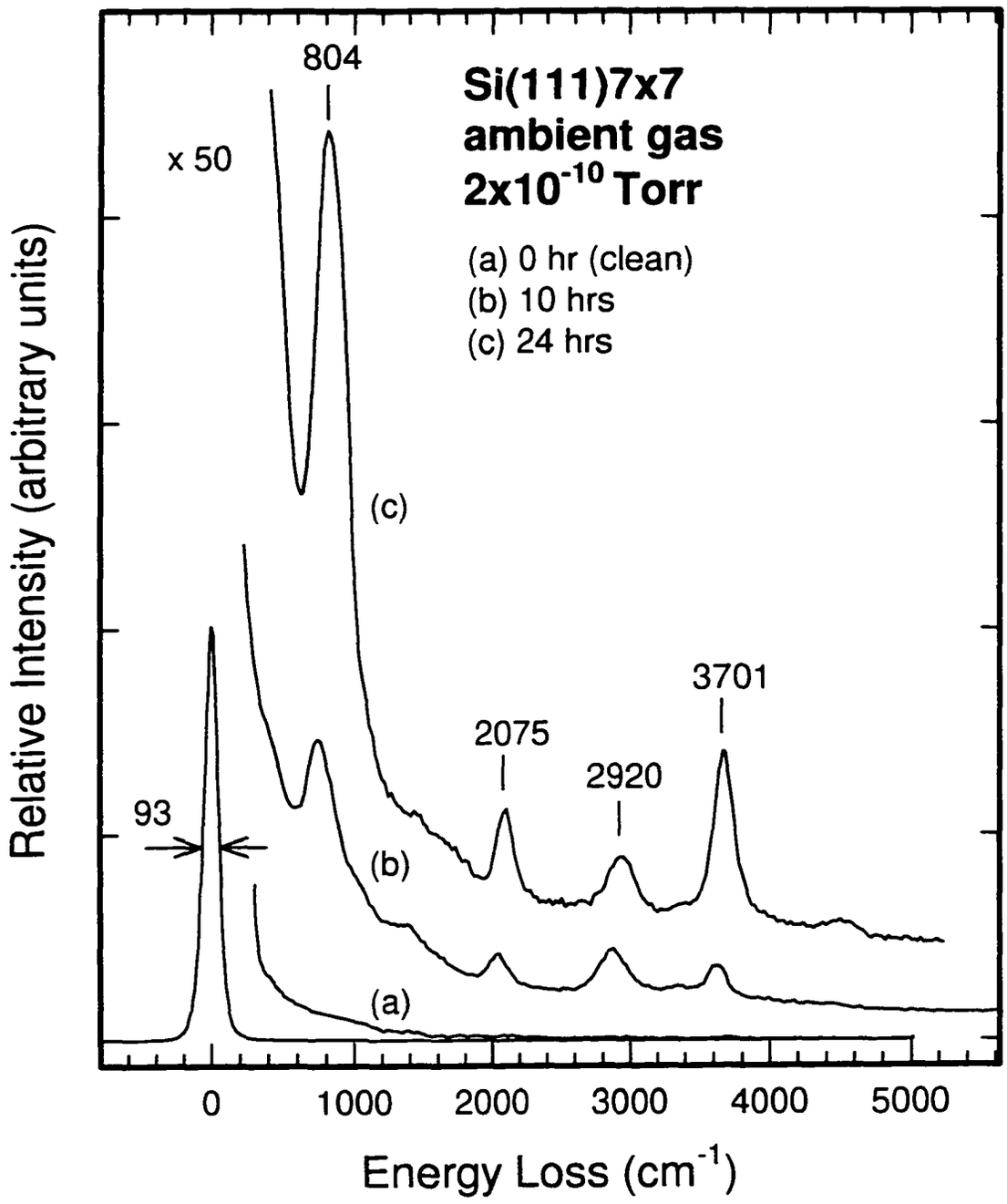

Figure 6.5 Vibrational electron energy loss spectra for (a) clean Si(111)7×7, and after (b) 10, and (c) 24 hours in an ambient pressure of $2x10^{-10}$ Torr.

Reproduced with permission of the copyright owner. Further reproduction prohibited without permission.

6.3 Coadsorption of water and oxygen on clean and C-precovered Si(111)7×7

Oxygen adsorption (or oxidation) on Si(111)7×7 is a very technologically important but complicated process. Although a voluminous amount of studies have been devoted to this topic, fundamental questions, especially those regarding the initial mechanisms involved in oxidation, continue to attract a lot of attention [9,18,19]. It is generally accepted that molecular adsorption is the precursor step to the stable atomic adsorption observed by Ibach *et al.* [8] and Edamoto *et al.* [20], which involves insertion of O atoms into the Si-Si bonds. However, even at a monolayer coverage several different bonding arrangements could coexist, making theoretical modeling employing a single type of atomic or molecular configuration inappropriate [21]. Furthermore, there is only a limited amount of work on the coadsorption of oxygen with other species. Of interest to the present work, oxygen and water coadsorption has been reported on Si(100)2×1 and Si(111)2×1 surfaces [22]. In this Section, we present results for oxygen coadsorption with ambient gas and carbon deposited on Si(111)7×7.

Figure 6.6 shows the effects of dosing 200 L of oxygen on Si(111)7×7 contaminated with ambient gas to different extent. The peaks at 386, 709, and 1046 cm^{-1} can be assigned to the rocking, symmetric and asymmetric stretching modes of the Si–O–Si radical respectively, in accord with previous studies [8,9]. The features at 2229 and 3684 cm^{-1} correspond, respectively, to the well-known H–Si and O–H stretching modes from dissociated water [12] (see also Figure 6.5). The feature at 2864 cm^{-1} can be assigned to a C–H stretching mode of adsorbed hydrocarbon species from the ambient gas, as described in previous section. It should be noted that the Si–H stretching frequency (2229 cm^{-1}) observed in Figure 6.6b-c is evidently higher than that (2075 cm^{-1}) in Figure 6.5. This shift could be caused by the change in the electronegativity of the Si atoms due to the presence of oxygen atoms as their neighbors [23]. Apparently a small amount of contamination due to water and hydrocarbons did not prevent the adsorption of oxygen. This is because the oxygen atoms are inserted into the Si–Si back bonds while the surface dangling bonds remain free for interacting with the H and OH radicals from dissociated water [12] and molecularly adsorbed hydrocarbons [14]. If we reversed the adsorption sequence (i.e., dosing the clean 7×7 surface with oxygen first, followed by exposing the sample to the

Reproduced with permission of the copyright owner. Further reproduction prohibited without permission.

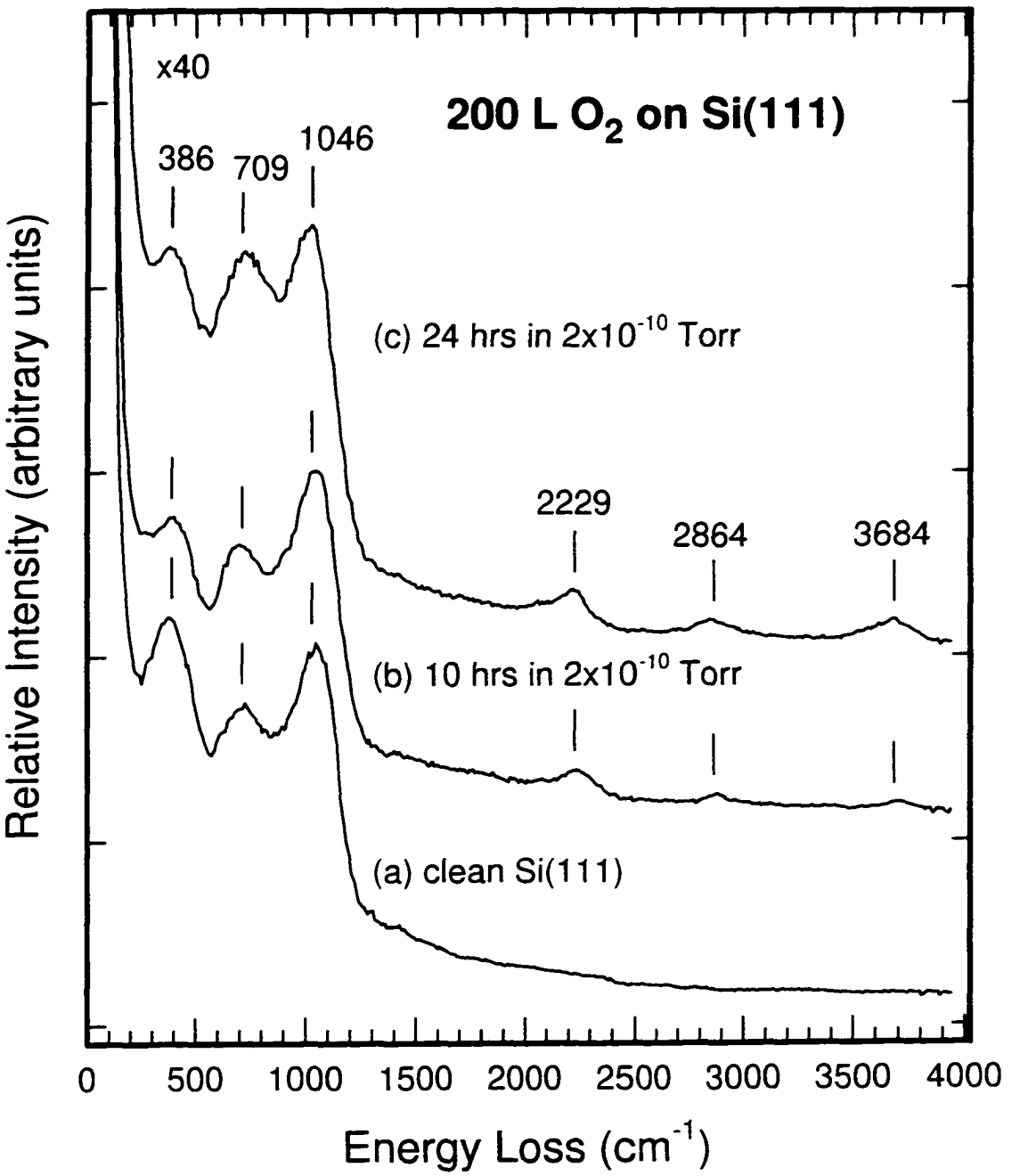

Figure 6.6 Vibrational electron energy loss spectra for a 200 L O_2 exposure on (a) a clean Si(111)7×7 surface, and sample (a) exposed to $2x10^{-10}$ Torr ambient gas for (b) 10 hours, and (c) 24 hours.

Reproduced with permission of the copyright owner. Further reproduction prohibited without permission.

ambient gas), we obtained similar results, whereby both water and hydrocarbons were found to adsorb on the oxygen precovered surface.

The formation of SiC on silicon surfaces has been achieved by exposing ethylene to a silicon surface at high temperature (~1000 K) by Bozso *et al.*, using a molecular beam technique [24]. In order to study a carbon precovered silicon surface, we used a similar approach by annealing the sample in ethylene at low dosage. Figure 6.7 shows the HREELS spectra for a sample annealed with different dosages of ethylene at 800 K. The strengthening of the peak at 826 cm^{-1} (Figure 6.7b-c) clearly shows the growth in the carbon concentration. The peak at 1714 cm^{-1} (Figure 6.7c) corresponds to an overtone of the Si–C stretch at 826 cm^{-1}. As the dosage was increased to 2000 L, the corresponding LEED pattern changed from a sharp 7×7 pattern to diffuse 7×7, 1×1, and finally to a very diffuse 1×1. This indicates that the SiC so produced was disordered and may be described as a thin Si–C alloy film, which was found on Si(100) in an earlier study [24]. Annealing this C-covered surface to a higher temperature (1200 K) could reduce the carbon feature (at 826 cm^{-1}) and partially restore the 7×7 LEED pattern, which indicates carbon diffusion into the bulk. This result is also consistent with the results obtained on Si(100) [24].

A small amount of carbon contamination (similar to the case used in Figure 6.7b) did not appear to affect the adsorption of oxygen and water. However, water adsorption became less efficient with increasing carbon concentration. Figure 6.8 compares the HREELS spectra for the adsorption of ambient gas on a clean surface and that on a surface with carbon contamination. On the clean Si(111)7×7 surface (Figure 6.8a), the adsorption of water and other hydrocarbon contaminants occurred readily (Figure 6.8b), in accord with the results shown in Figure 6.5. On the carbon precovered surface (Figure 6.8c), however, the adsorption rates for water and hydrocarbons were reduced significantly (Figure 6.8d). This indicates that the formation of Si–C alloy consumed the surface dangling bonds, hence poisoning the surface reactions. After annealing the C-covered surface to a higher temperature (1200 K), the adsorption rate of ambient gas became enhanced, which again suggests C diffusion into the bulk.

The pre-deposition of C-containing species on Si(111)7×7 was also not found to have any adverse effect on the adsorption of oxygen. Figure 6.9 shows the HREELS

Reproduced with permission of the copyright owner. Further reproduction prohibited without permission.

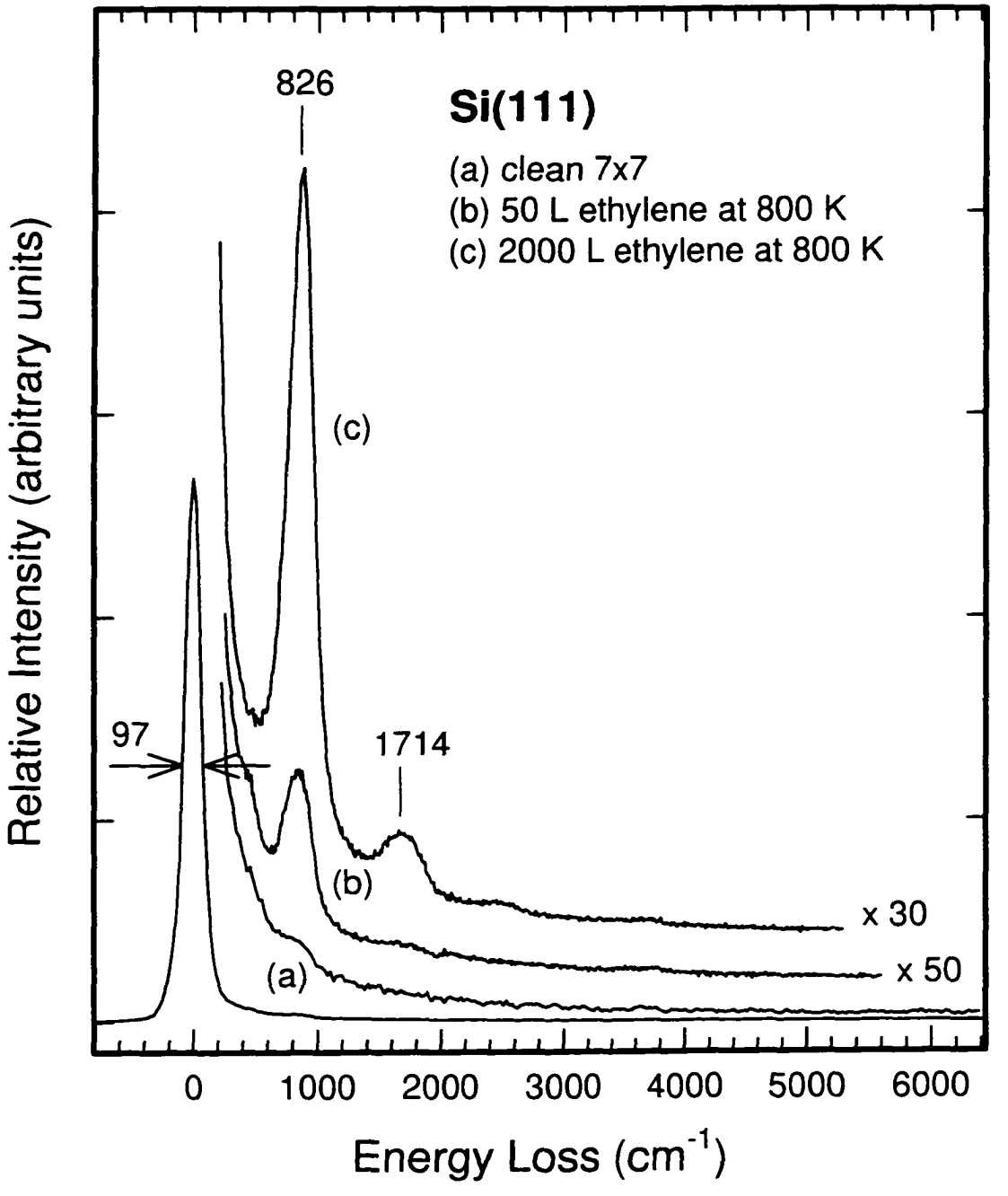

Figure 6.7 Vibrational electron energy loss spectra for carbon deposition on Si(111)7×7 by annealing (a) a clean Si(111)7×7 surface in ethylene for (b) 50 L, and (c) 2000 L at 800 K.

Reproduced with permission of the copyright owner. Further reproduction prohibited without permission.

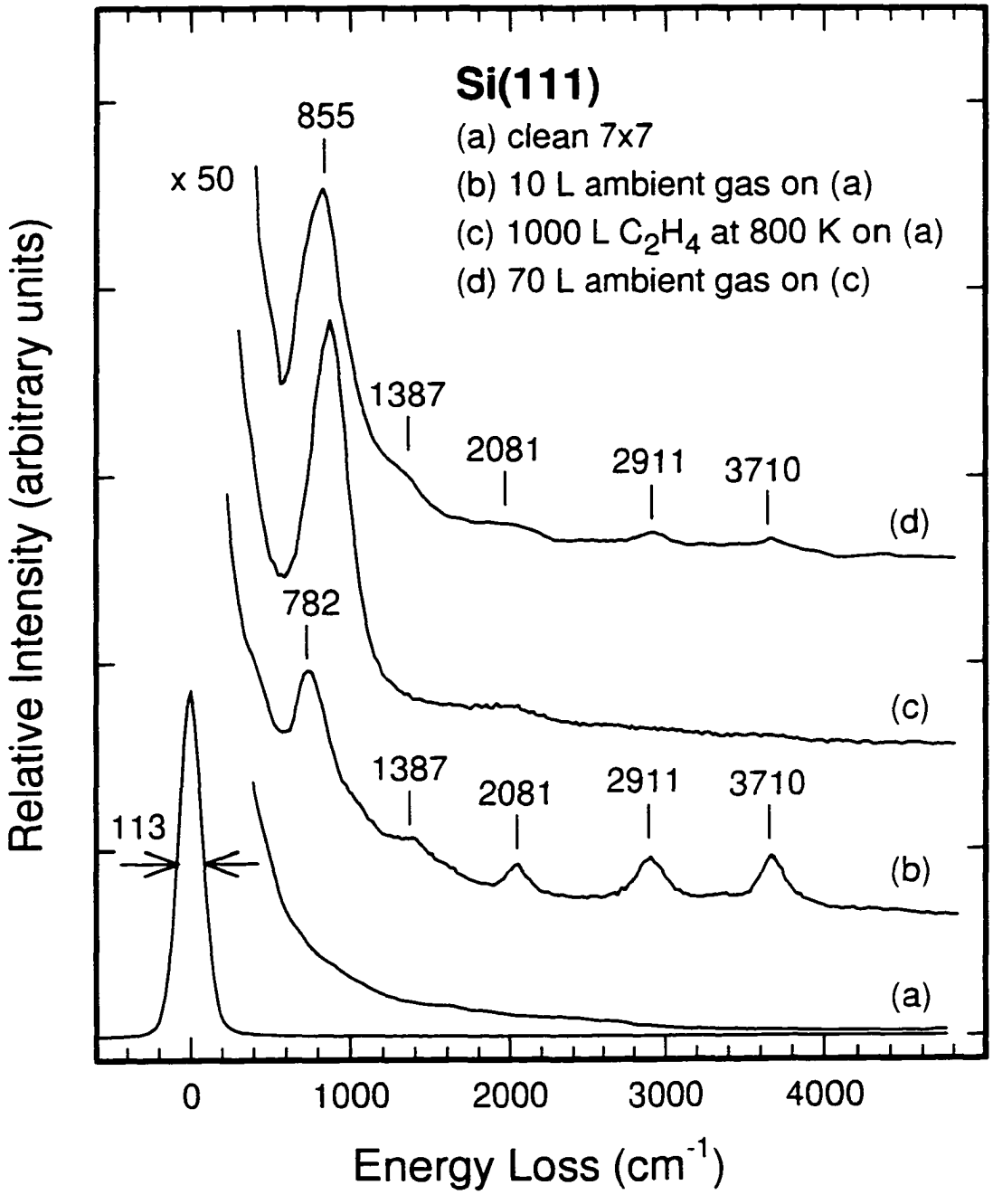

Figure 6.8 Vibrational electron energy loss spectra for (a) clean Si(111)7×7, (b) sample (a) exposed to an equivalence of 10 L of ambient gas commonly found in an ultrahigh vacuum chamber, (c) sample (a) dosed with 1000 L of ethylene at 800 K, and (d) sample (c) exposed to an equivalence of 70 L of ambient gas.

Reproduced with permission of the copyright owner. Further reproduction prohibited without permission.

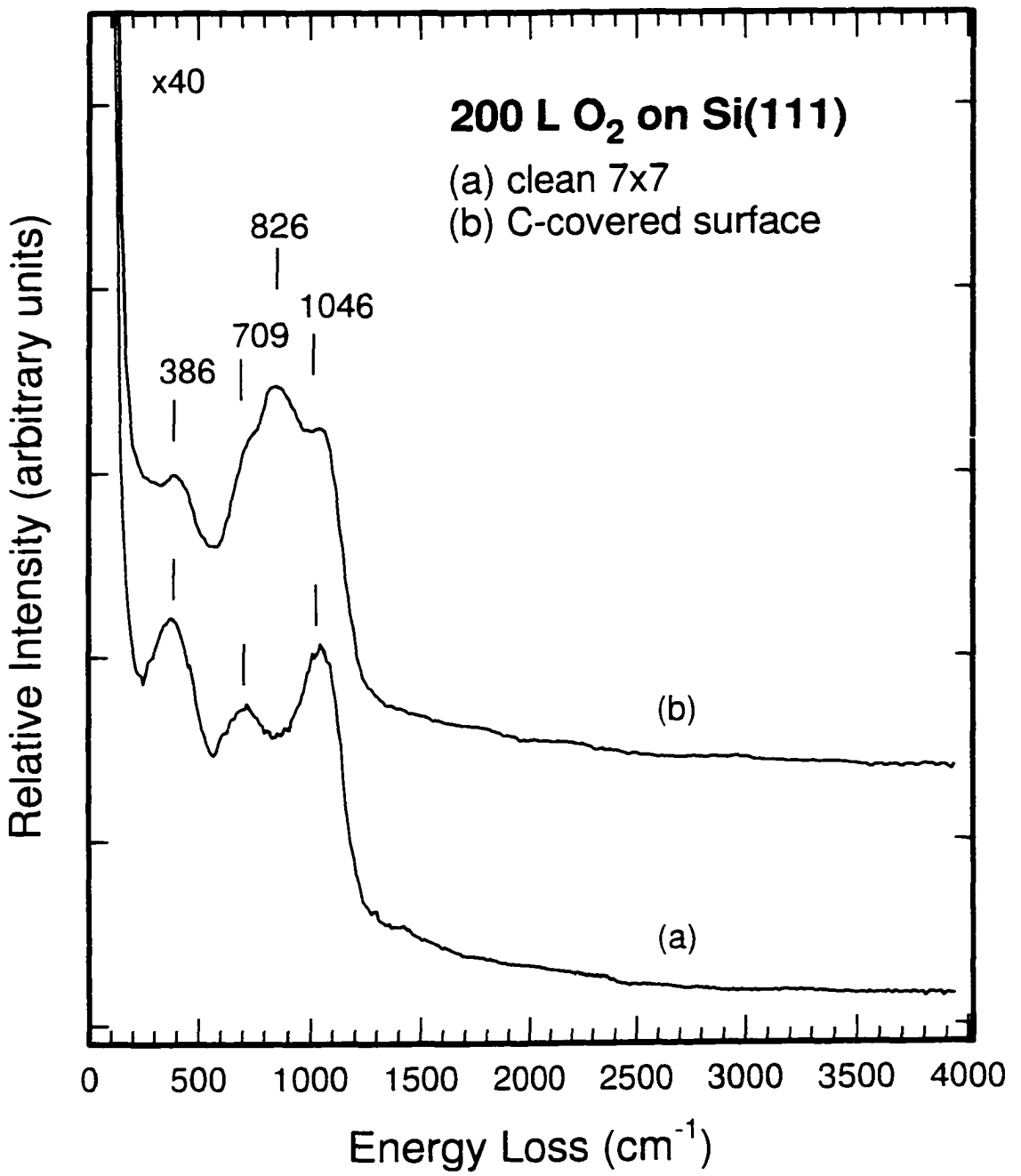

Figure 6.9 Vibrational electron energy loss spectra for 200 L of oxygen adsorption on (a) clean Si(111)7×7, and on (b) C-covered Si(111) prepared by dosing sample (a) with 1 kL of C_2H_4 at 800 K.

Reproduced with permission of the copyright owner. Further reproduction prohibited without permission.

spectra for oxygen exposure on clean (Figure 6.9a) and C-precovered Si(111)7×7 surface (Figure 6.9b). Except for the addition of the Si–C stretch at 826 cm^{-1}, the oxygen-related features (observed at 386, 709, and 1046 cm^{-1}) for the C-precovered surface are clearly present and remain essentially unchanged from those for the clean surface. The coexistence of carbon and oxygen on Si(111)7×7 provides further evidence to support the conjecture that oxygen adsorption does not rely on the dangling bonds but on the insertion into the Si–Si back bonds. In addition, the lack of a C–O stretching mode in Figure 6.9b suggests there was no reaction between oxygen and the pre-deposited surface carbon on Si(111)7×7, unlike the Cu(100) case (Chapter 3).

6.4 Summary

We demonstrate the susceptibility of Si(111)7×7 to the contaminants commonly found in a standard UHV chamber (including carbon, water, and hydrocarbons) and the sensitivity of HREELS in detecting these surface contaminants. We show that a sharp 7×7 LEED pattern for Si(111) does not necessarily mean that the surface is free of contamination, although the contamination level is sufficiently low that no major effects on surface reactions and adsorption are expected. A sharp 7×7 LEED pattern can therefore still be used as a good indicator of surface cleanliness before performing the surface reactions. Furthermore, oxygen was found to coadsorb with different levels of carbon, water, and hydrocarbons at room temperature. The nature of oxygen adsorption was also found to be not sensitive to pre-deposited species, such as water and carbon. However, the coadsorbed oxygen could cause a blue shift in the Si–H stretching frequency when it coadsorbed with water, which can be attributed to changes in the electronegativity of the Si atoms due to the presence of oxygen atoms as their neighbours. Annealing the silicon sample in ethylene at 800 K provides an effective means of depositing carbon to form a disordered Si–C alloy on Si(111)7×7. A high level of surface carbon is found to poison the surface and prevent further water and hydrocarbon adsorption but not oxygen adsorption, which indicates the passivation of dangling bonds by the carbon atoms. Further studies on the coadsorption of pure water, ethylene, oxygen, and hydrogen on both clean and C-precovered Si(111) surfaces will be useful in determining the competition of adsorption sites for these species.

Reproduced with permission of the copyright owner. Further reproduction prohibited without permission.

6.5 References

[1] N. G. Einspruch and H. Huff (eds.), "VLSI Electronics: Microstructure Science", Vol. 12, Academic, Orlando (1985).

[2] D. A. King and D. P. Woodruff (eds.), "The Chemical Physics of Solid Surfaces and Heterogeneous Catalysis", Vol **5**, Elsevier, New York (1988).

[3] K. Takayanagi, Y. Tanishiro, M. Takahashi, and S. Tahahashi, J. Vac. Sci. Technol. A **3**, 1502 (1985).

[4] K. D. Brommer, M. Needels, B. E. Larson, and J. D. Joannopoulos, Phys. Rev. Lett. **68**, 1355 (1992).

[5] R. J. Hamers, R. M. Tromp, and J. E. Demuth, Phys. Rev. Lett. **56**, 1972 (1986).

[6] R. Wolkow and Ph. Avouris, Phys. Rev. Lett. **60**, 1049 (1988).

[7] Ph. Avouris, J. Phys. Chem. **94**, 2246 (1990).

[8] H. Ibach, N. D. Bruchmann and H. Wagner, Appl. Phys. A **29**, 113 (1982).

[9] G. Comtet, L. Hellner, G. Dujardin, and M. J. Ramage, Surface, Sci. **352-354**, 315 (1996).

[10] H. Froitzheim, U. Kohler and H. Lammering, Surf. Sci. **149**, 537 (1985).

[11] F. Owman and P. Martensson, Surf. Sci. **330**, L639 (1995).

[12] H. Ibach, H. Wagner and D. Brchmann, Solid State Commun. **42**, 457 (1982).

[13] M. C. Flowers, N. B. H. Jonathan, A. Morris, S. Wright, Surf. Sci. **351**, 87 (1996).

[14] J. Yoshinobu, H. Tsuda, M. Onchi, and M. Nishijima, Chem. Phys. Lett. **130**, 170 (1986).

[15] J. Yoshinobu, H. Tsuda, M. Onchi, and M. Nishijima, Solid State Commun. **60**, 801 (1986).

[16] C. C. Cheng, P. A. Taylor, etc., Thin Solid Films **225**, 196 (1993).

[17] K. Edamoto, S. Tanaka, M. Onchi, and M. Nishijima, Surf. Sci. **167**, 285 (1986).

[18] R. Martel, Ph. Avouris, and I. W. Lyo, Science **272**, 385 (1996).

[19] T. Engel, Surf. Sci. Rep. **18**, 91 (1993).

[20] K. Edamoto, Y. Kubota, H. Kobayashi, M. Onchi, and M. Nishijima, J. Chem. Phys. **83**, 428 (1985).

Reproduced with permission of the copyright owner. Further reproduction prohibited without permission.

[21] G. Hollinger and F. J. Himpsel, Phys. Rev. B **28**, 3651 (1983).

[22] J. A. Schaefer, F. Stucki, D. J. Frankel, W.Gopel, and G. J. Lapeyre, J. Vac. Sci. Technol. B **2**, 359 (1984).

[23] J. A. Schaefer, D. J. Frankel, F. Stucki, W. Gopel, and G. J. Lapeyre, Surf. Sci. **139**, L209 (1984).

[24] F. Bozso, J. T. Yates, Jr, W. J. Choyke, and L. Muehlhoff, J. Appl. Phys. **57**, 2771 (1985).

Reproduced with permission of the copyright owner. Further reproduction prohibited without permission.

Chapter 7
ELS STUDIES OF THE FORMATION OF SiO_2 AND SiC THIN FILMS ON Si(111)7×7

7.1 Introduction

Both oxide and carbide layers are among the most common types of thin films present on silicon surfaces. The nature of the oxidation layer and its formation mechanisms on different low Miller index planes of Si have been studied extensively over the past three decades. Although the nature of the initial molecular adsorption remains as the subject of intense debates [1,2,3], it has generally been accepted that oxygen exposure to a Si surface at RT leads to the breaking of a Si-Si bond via the insertion of an atomic oxygen between two Si atoms [4,5]. Unlike the vitreous SiO_2 structure in silica with a Si-Si distance of 3.05 Å, the Si-Si distance of the oxide layer formed on a silicon surface at RT is essentially the same as that in crystalline silicon (2.35 Å). This oxide layer therefore has a smaller bond angle (the angle between two Si–O bonds) than that in the vitreous SiO_2 structure and has been described as a "compressed" SiO_2 structure by Ibach et al. [4]. The vitreous SiO_2 layer was not found on Si(111)7×7 for exposure of oxygen even as high as 10^{11} L at RT, but it could be formed if a Si wafer was held at 700 K during O_2 exposure [4]. Hollinger et al. [6] showed that the formation of SiO_2 films involves an evolution of chemical structure from a metastable random bonding phase to a microscopic mixture of Si and SiO_2 when the wafer temperature is increased. Furthermore, the uptake rate at higher temperature (~970 K) was found to be enhanced in the high-exposure region but is significantly reduced in the low-exposure region, which could be due to oxygen desorption as volatile SiO [6]. Although thermally formed SiO_2 layers have been investigated extensively, no study on ion-induced SiO_2 formation has been made. In particular, while Ibach and coworkers have characterized the SiO_2 layer by using second-derivative mode ELS [7], the characterization of SiO_2 films by ELS in the non-derivative (i.e., normal) mode ELS has not been reported.

Another widely investigated film on the silicon surface is the carbonaceous film. Depending on the deposition procedures used [8,9], there are different kinds of carbonaceous films that can be formed on a silicon surface, including SiC, graphite,

Reproduced with permission of the copyright owner. Further reproduction prohibited without permission.

amorphous C, amorphous C:H, diamond-like carbon, and diamond films. Growth of these films usually involves CVD together with various kinds of reaction enhancement technologies (such as ion-sputtering and plasma-assisted methods). The nature of these films is determined by the relative content of sp^3 tetrahedrally coordinated carbon and the concentration of atomic hydrogen in the films. Although a large amount of work has been devoted to the preparation of these films involving different methods and recipes [10], detailed understanding of the growth mechanisms and the initial reaction process is far from complete. Careful in situ studies on the early stages in the formation of these films will therefore be very useful in achieving this goal.

Because of its capability in providing information about electronic transitions and plasmon excitations, ELS is a powerful tool for characterization of thin films [8,11]. Depending on the impact energy and scattering geometry employed, the electron can penetrate to different depths into the surface. It is therefore possible to obtain information about the electronic structures of both the surface and the sub-surface region (approximately 2-6 monolayers underneath the surface for an incident energy of 20-1000 eV) [12,13]. In this Chapter, we apply both ELS and HREELS techniques (along with AES) to investigate the initial formation of SiO_2 and SiC films on a Si(111)7×7 surface prepared by using thermal and ion irradiation methods.

7.2 Characterization of SiO_2 film formation on Si(111)7×7

Previous studies on clean Si(111)7×7 by using ELS in second derivative mode by Ibach and coworkers [7] revealed several interesting spectroscopic features, including a bulk plasmon at ~17 eV, a surface plasmon at 10 eV, three surface-related transitions at 1.8, 8, and 15 eV, and two bulk band transitions at 3 and 4.5 eV. A later work involving normal mode ELS by Froitzheim et al. [14] also reported the surface and bulk transitions below 6 eV with less evident features than that found with second-derivative mode ELS. Figure 7.1 shows our ELS spectra (normal mode) for clean Si(111)7×7 before and after 1 kL of oxygen exposure at RT, and followed by annealing to 570 K and 700 K. The previously reported bulk plasmon at 17.5 eV, surface plasmon peak at 10 eV (appeared as a shoulder), and

Reproduced with permission of the copyright owner. Further reproduction prohibited without permission.

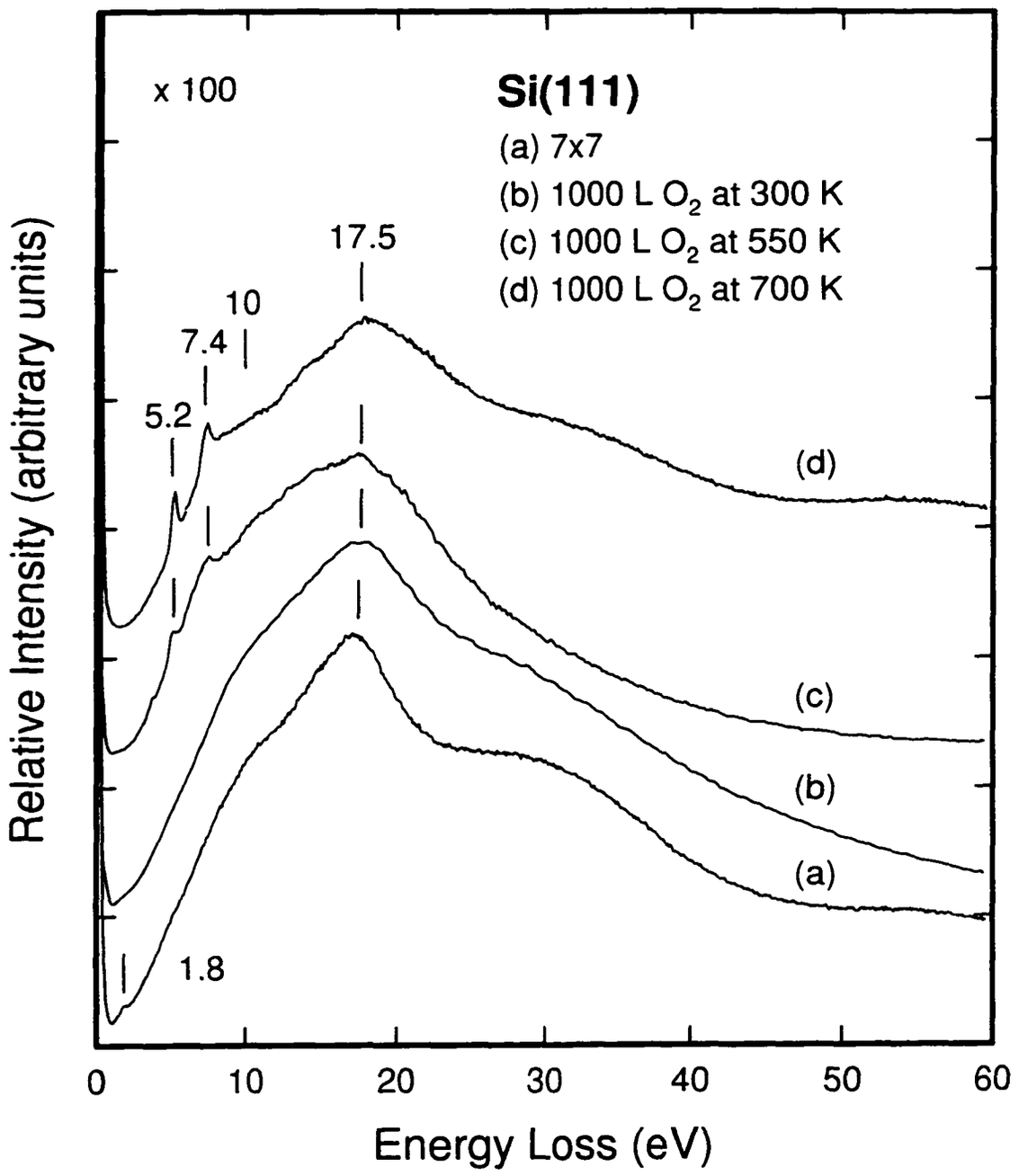

Figure 7.1 Electronic electron energy loss spectra for (a) clean Si(111)7×7 and after exposure of 1 kL of oxygen with sample (a) held at (b) 300 K, (c) 550 K, and (d) 700 K.

Reproduced with permission of the copyright owner. Further reproduction prohibited without permission.

surface-related transition at 1.8 eV on clean Si(111)7×7 are clearly evident in Figure 7.1a. Other features observed by the second-derivative-mode ELS [7] are not observed in our normal-mode spectra, which, however, are consistent with the results obtained using normal-mode ELS by other groups [8,13]. After a 1 kL of oxygen exposure at RT, the surface-related transition at 1.8 eV disappeared and no additional ELS feature was found (Figure 7.1b). The plasmon features became broadened due to the adsorption of atomic oxygen. Although the previous ELS studies using the second derivative mode also indicated an increase in the intensities of the features at 5.2 and 7.4 eV after the dosing of oxygen, these changes are less apparent in our non-derivative-mode spectra. When the oxygen exposure was performed at an elevated temperature (Figures 7.1c-d), two sharp peaks appeared at 5.2 and 7.4 eV. Previous studies showed that at an elevated temperature the chemical composition of the oxidation products changed from a metastable random bonding phase to a microscopic mixture of Si and SiO_2 accompanied by the enhancement of oxidation [1,6,15]. Clearly, the two peaks observed at 5.2 and 7.4 eV can be assigned to SiO_2-related transitions. It is also unlikely that these two peaks were simply caused by an increase in the surface oxygen concentration because a separate experiment involving a significantly higher exposure of oxygen (10 kL) to Si(111)7×7 at RT did not reveal these peaks. Furthermore, as shown in Figure 7.2b, if the sample in Figure 7.1b was annealed to a higher temperature (700 K), the two peaks also appeared (Figure 7.2b), which indicated that these two peaks are related to the bonding structure of SiO_2. The formation of SiO_2 at 700 K is also consistent with a corresponding HREELS spectrum shown in Figure 7.3b, with characteristic blue-shifted frequencies at 465, 812, and 1134 cm^{-1} [4] (the assignments of these three features have been discussed in Chapter 6). When the sample was further annealed to 1270 K (Figure 7.2c), oxygen desorbed from the surface and the 7×7 LEED pattern was restored.

Although a large dose of oxygen at RT does not generate SiO_2 on the silicon surface [4], SiO_2 can be produced by ion-assisted deposition at RT. Figure 7.4 shows the ELS spectra for Si(111)7×7 ion-irradiated in O_2 at RT, following the procedure discussed in Chapter 2. In particular, Figure 7.4a clearly depicts the presence of SiO_2 on the surface, although the features at 5.2 and 7.4 eV are not as intense as those found for the sample

Reproduced with permission of the copyright owner. Further reproduction prohibited without permission.

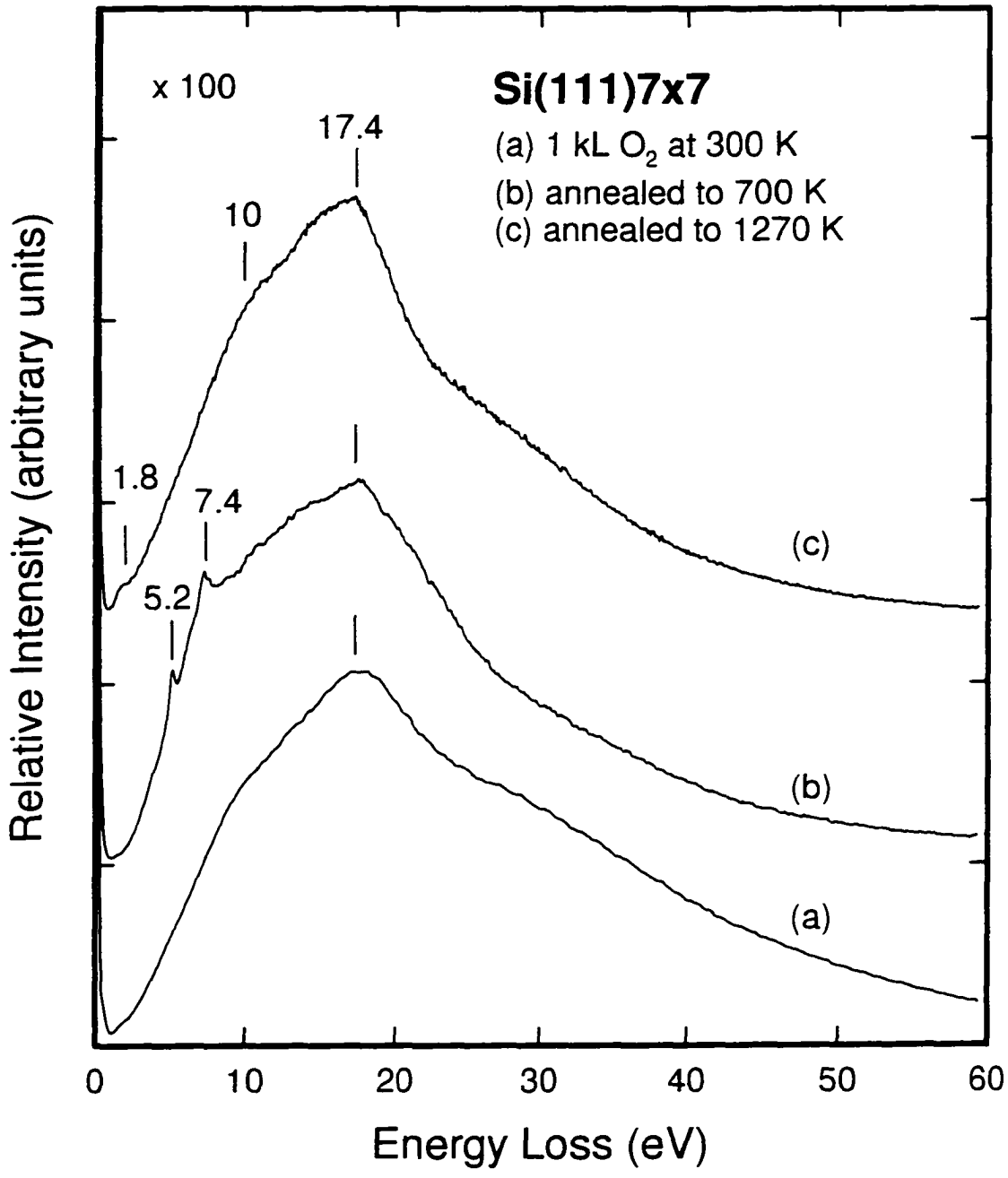

Figure 7.2 Electronic electron energy loss spectra for Si(111)7×7 with (a) 1 kL oxygen exposure at 300 K and sample (a) annealed to (b) 700 K and (c) 1270 K.

Reproduced with permission of the copyright owner. Further reproduction prohibited without permission.

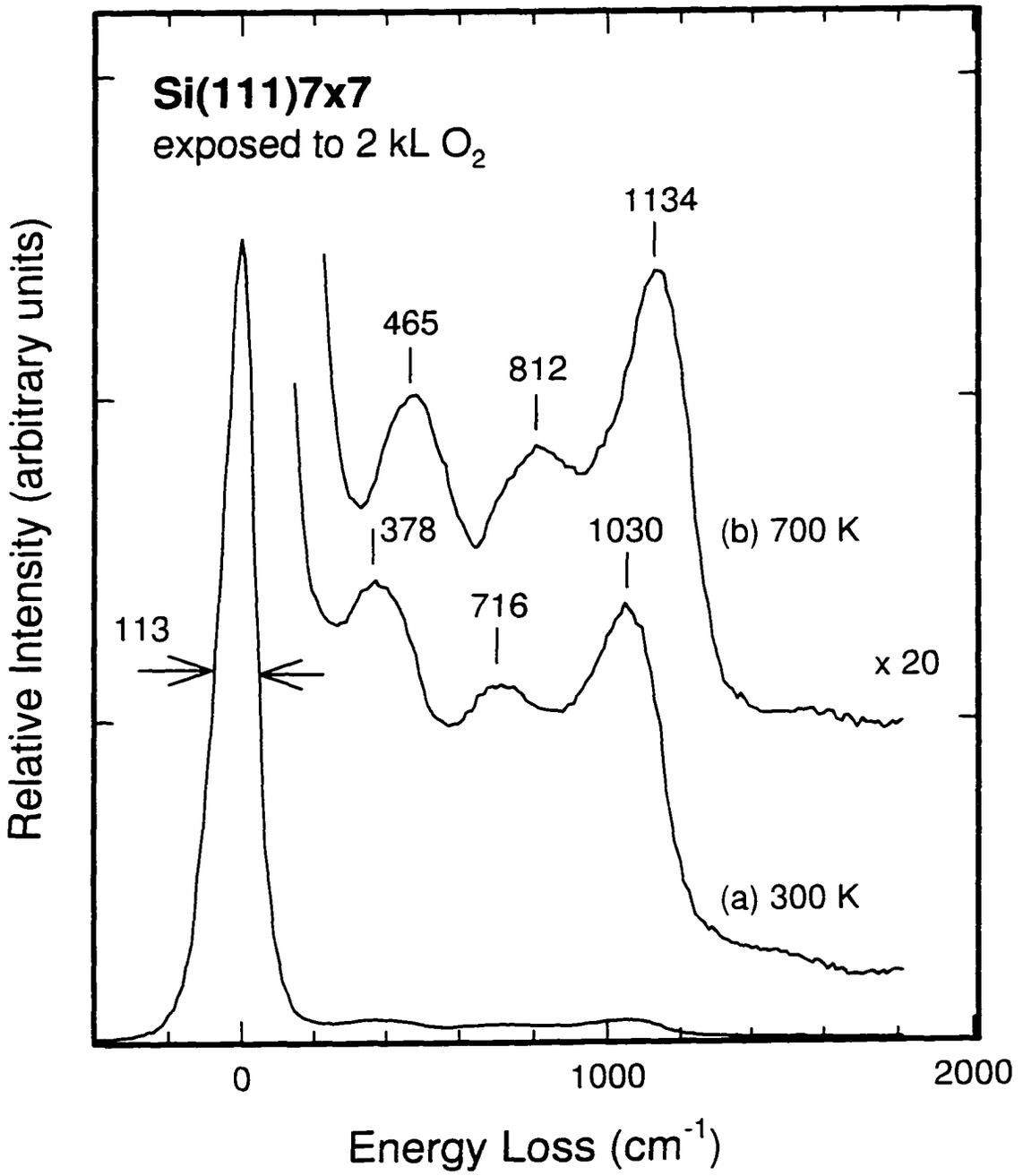

Figure 7.3 Vibrational electron energy loss spectra for 2 kL oxygen exposed to Si(111)7×7 surface at (a) 300 K and (b) 700 K.

Reproduced with permission of the copyright owner. Further reproduction prohibited without permission.

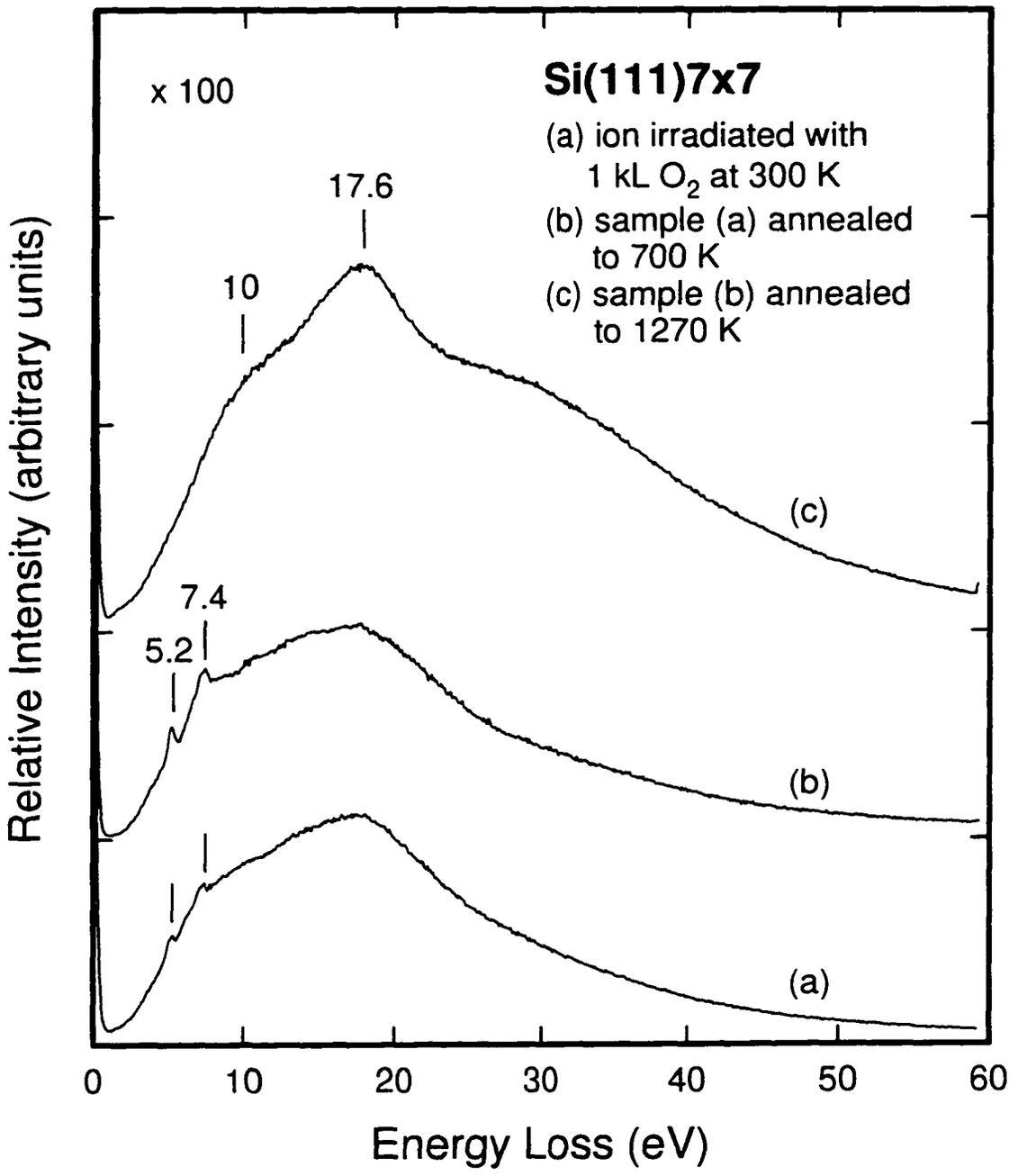

Figure 7.4 Electronic electron energy loss spectra for Si(111)7×7 (a) ion-irradiated at 300 K with 1 kL of O_2 at 200 eV, and sample (a) annealed to (b) 700 K and (c) 1270 K.

Reproduced with permission of the copyright owner. Further reproduction prohibited without permission.

prepared at 700 K with the same amount of oxygen exposure (Figure 7.1c). Annealing the sample in Figure 7.4a to a higher temperature increased the intensity of the peaks at 5.2 and 7.4 eV, which indicates that the initial products after ion irradiation contained both adsorbed atomic oxygen and SiO_2. As the temperature was increased, the adsorbed atomic oxygen apparently underwent transformation to SiO_2. Finally, when the sample was annealed to 1270 K (Figure 7.4c), all the surface oxygen desorbed and the sharp 7×7 LEED pattern was again restored. Because the formation of SiO_2 requires breaking of the Si–Si bonds and dislocation of the Si atoms in the sub-surface region, this experiment therefore provides evidence for ion-induced rearrangement of surface atoms to form SiO_2 at RT.

7.3 Characterization of the formation of a carbonaceous thin film on Si(111)7×7

ELS has proven to be a useful tool for probing plasmon excitations of C-containing thin films [8,13]. In particular, the films with sp^3 bonding structure (such as diamond and SiC) can be characterized by the positions of their surface and bulk plasmon peaks. For the films involving sp^2 bonding structure (such as graphite, *a*-C, and *a*-C:H), their plasmon features can be represented by a π plasmon feature due to the π electrons and a $\pi+\sigma$ plasmon feature due to all valence electrons [8,16]. Table 7.1 summarizes the typical values of the plasmon peaks for different carbonaceous films reported in the Refs. 8, 13, and 17. The films are identified by the sp^2 or sp^3 bond content with respect to the total carbon bonds in the corresponding films.

As demonstrated in Chapter 6, the disordered Si–C alloy could be generated by annealing the Si sample in ethylene at 800 K and the deposited carbon atoms might undergo diffusion into the bulk at a higher temperature. Previous studies by Yates and coworkers [13,18] indicated that below 940 K only a limited amount of carbon could be deposited on a Si(100) surface due to diffusion-limited growth, which suggests that at this temperature range the limited lattice mobility prevents the formation of SiC. In order to determine the properties of the thermally deposited carbon layer, we performed a series of HREELS and AES experiments at different ethylene dosages. In Figure 7.5, we show the intensities of representative carbon-related features observed in HREELS and AES spectra as a function of ethylene exposure to Si(111)7×7 held at 800 K. In particular, the peak at 826 cm^{-1}

Reproduced with permission of the copyright owner. Further reproduction prohibited without permission.

Table 7.1 Energy positions of the plasmon features for common carbon-containing films [after 8,13, and 17].

	Surface plasmon (eV)	Bulk plasmon (eV)	π plasmon (eV)	π+σ plasmon (eV)	sp^2 or sp^3 percentage
Graphite	-	-	7	25	100 sp^2
a-C	-	-	6	23	80 ± 10 sp^2
a-C·H	-	-	6	25	40 ± 5 sp^2
β-SiC	18	23	-	-	100 ± 10 sp^3
Diamond	24	33	-	-	100 ± 10 sp^3

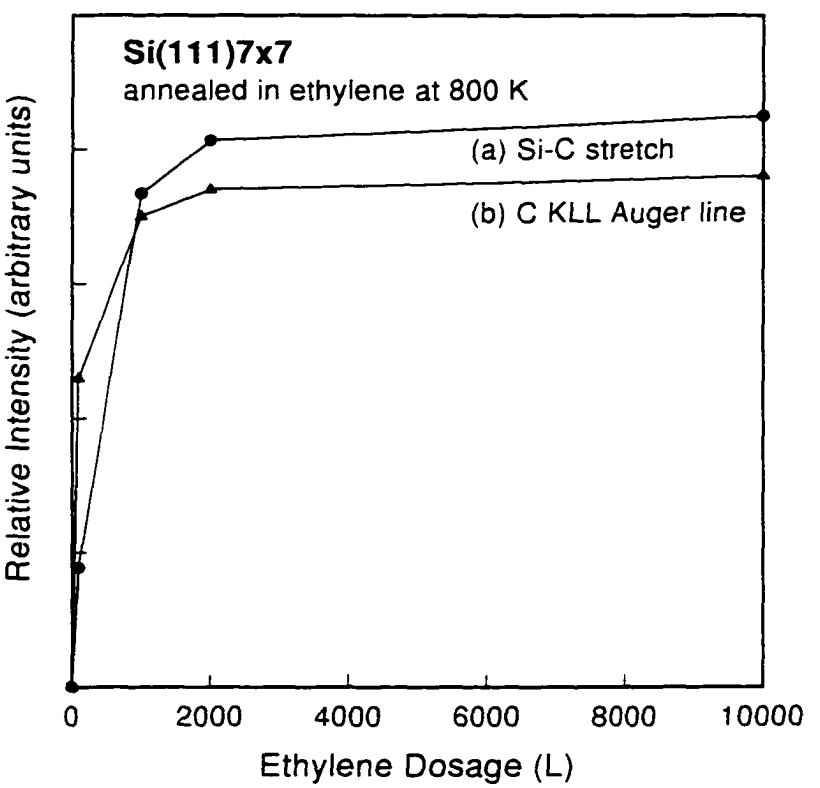

Figure 7.5 Relative intensity of a carbon-related feature for Si(111)7×7 annealed at 800 K as a function of ethylene dose in (a) HREELS (at 826 cm^{-1} energy loss) and (b) AES spectra (at 274 eV kinetic energy).

Reproduced with permission of the copyright owner. Further reproduction prohibited without permission.

corresponding to Si–C stretch as described in Chapter 6 was used for the HREELS spectra (Figure 7.5a), while the carbon KLL Auger transition at 274 eV was used for the AES spectra (Figure 7.5b). Below 1 kL of ethylene exposure, both curves show that the carbon concentration increases rapidly and becomes saturated above 2 kL. Because the HREELS spectra only carry information about the surface region while AES spectra contain a contribution from both the surface and the bulk, we would expect to see the intensities of the HREELS and AES features level off at different ethylene dosages if the surface carbon atoms keep diffusing into the bulk. The similarity in the intensity variation for both HREELS and AES features indicates that predominant carbon diffusion into the bulk is not likely at this temperature, which is consistent with the result found for Si(100) by Bozso et al. [13]. Further annealing the C-covered surface to a higher temperature (>1000 K) reduced the intensities of the corresponding carbon-related features in both the HREELS and AES spectra, which indicates that diffusion of carbon atoms into the bulk occurred at a higher temperature.

To characterize the thermally deposited carbon layer by means of its characteristic plasmon and electronic transition features, ELS experiments were conducted. Figure 7.6 shows the ELS spectra of Si(111)7×7 before and after annealing in 1 kL and 10 kL of ethylene at 800 K. With increasing ethylene dosage, the surface plasmon at 10 eV became less evident and the bulk plasmon peak for the clean surface shifted from 17.4 eV to 20 eV after 10 kL ethylene dosage (Figure 7.6c). According to Table 7.1, the peak observed at 20 eV can be attributed to a combination of the bulk plasmon peaks for silicon at 17 eV and the $\pi+\sigma$ plasmon for *a*-C at 23 eV. Because the bulk plasmon peak of SiC was also found to be at 23 eV, the presence of SiC cannot be ruled out. A similar feature has also been found on Si(100) using a molecular beam CVD technique by Bozso et al. [13] and the corresponding as-formed layer was assigned as a "Si-C alloy". Bozso et al. [13] also suggested that the formation of SiC occurred below the top Si layer at a higher annealing temperature (~940 K). Because the incident energy used in our current ELS setup is limited up to 100 eV, we cannot detect the formation of SiC underneath the silicon surface, due to the limited electron penetration depth [13]. After annealing the sample in Figure 7.6c to a higher temperature (>1200 K), we observed that the plasmon peak shifted back to 18 eV (not shown), indicative

Reproduced with permission of the copyright owner. Further reproduction prohibited without permission.

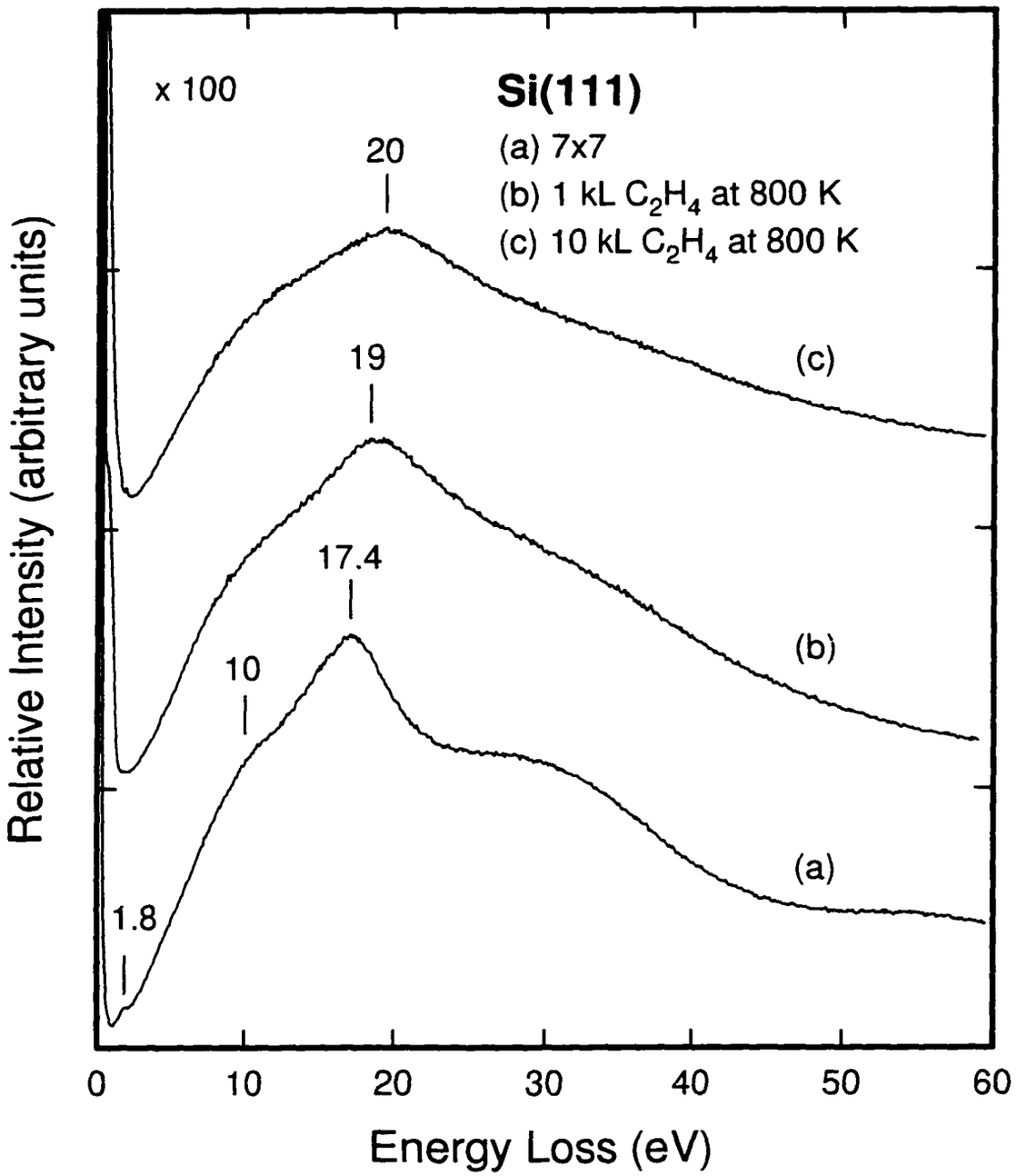

Figure 7.6 Electronic electron energy loss spectra for a clean Si(111)7×7 surface (a) held at 800 K during exposure of 1 kL (b) and 10 kL of ethylene (c).

Reproduced with permission of the copyright owner. Further reproduction prohibited without permission.

of carbon diffusion into the bulk.

At RT, molecular adsorption of ethylene was found to occur on the Si(111) surface with near sp^3 hybridization by Yoshinobu et al. [19]. However, with the irradiation of unmass-selected ethylene ions (see Chapters 2 and 5 for details of the generation of ethylene ions), adsorption hydrocarbon species was found to occur far more efficiently. The HREELS features of the adsorbed species were also different from that of molecularly adsorbed ethylene. Figure 7.7 shows the HREELS spectra of ethylene-ions-induced adsorption on Si(111)7×7 at RT. In particular, the C–H stretch observed at 2911 cm^{-1} is indicative of the adsorption of hydrocarbon fragments (Figure 7.7a), while the vibrations below 1500 cm^{-1}, including CC stretch, CH_2 vibrations (scissors, wag, twist, and rock) and SiC stretch, cannot be clearly resolved. In the case of ion irradiation in ethylene at 200 eV IE, Figure 7.7b shows, in addition to the generally more intense adsorption features, the presence of hydrogen adsorption as indicated by the strong features at 644 cm^{-1} (SiH bending mode), 893 cm^{-1} (SiH_2 scissoring mode), and 2075 cm^{-1} (SiH stretching mode) [20]. The weak peak at 1387 cm^{-1} can be assigned to a CH_2 scissoring mode [19]. After the sample was annealed to 1000 K, all hydrogen-related features disappeared and only the peak near 840 cm^{-1} corresponding to Si–C stretch remained (Figure 7.7c-d). Evidently, the production of surface carbon by ion-assisted reactions (Figure 7.7d) could be enhanced relative to that by thermal dissociation (Figure 7.7c).

Figure 7.8 shows the ELS spectra for surface carbon produced by ion irradiation in 10 kL of ethylene at 50 eV IE followed by annealing to different temperatures. The spectra for the as-deposited sample (Figure 7.8a) and the sample after the 800 K anneal are characterized by the broad plasmon peak near 20 eV, which is similar to that observed in the thermal deposition case (Figure 7.6). The carbonaceous layer so produced can therefore be assigned to a Si-C alloy layer as discussed earlier. In Figure 7.8a, specific contribution from hydrogen-related species is not observed, which may be due to the close proximity of the plasmon peaks for C:H and C (see Table 7.1). After the sample was annealed to 1270 K, restoration of the clean silicon surface was indicated by the shift in the position of the bulk plasmon peak to 18 eV, which in turn suggested that diffusion of surface carbon into the bulk might also occur. This observation is consistent with the corresponding AES results

Reproduced with permission of the copyright owner. Further reproduction prohibited without permission.

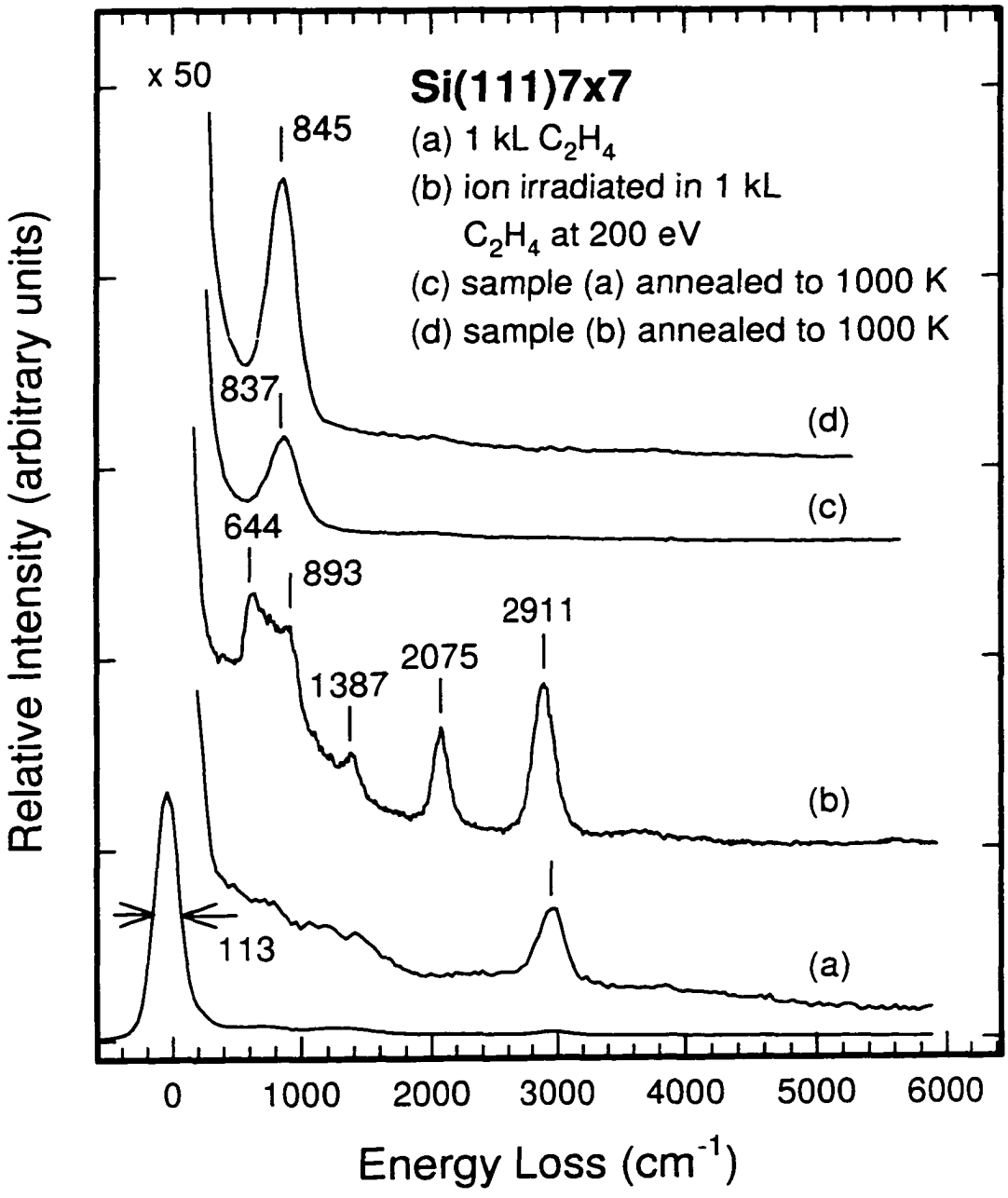

Figure 7.7 Vibrational electron energy loss spectra for Si(111)7×7 (a) exposed with 1 kL of C_2H_4, (b) ion-irradiated with 1 kL C_2H_4 at 200 eV impact energy, (c) sample (a) annealed to 1000 K, and (d) sample (b) annealed to 1000 K.

Reproduced with permission of the copyright owner. Further reproduction prohibited without permission.

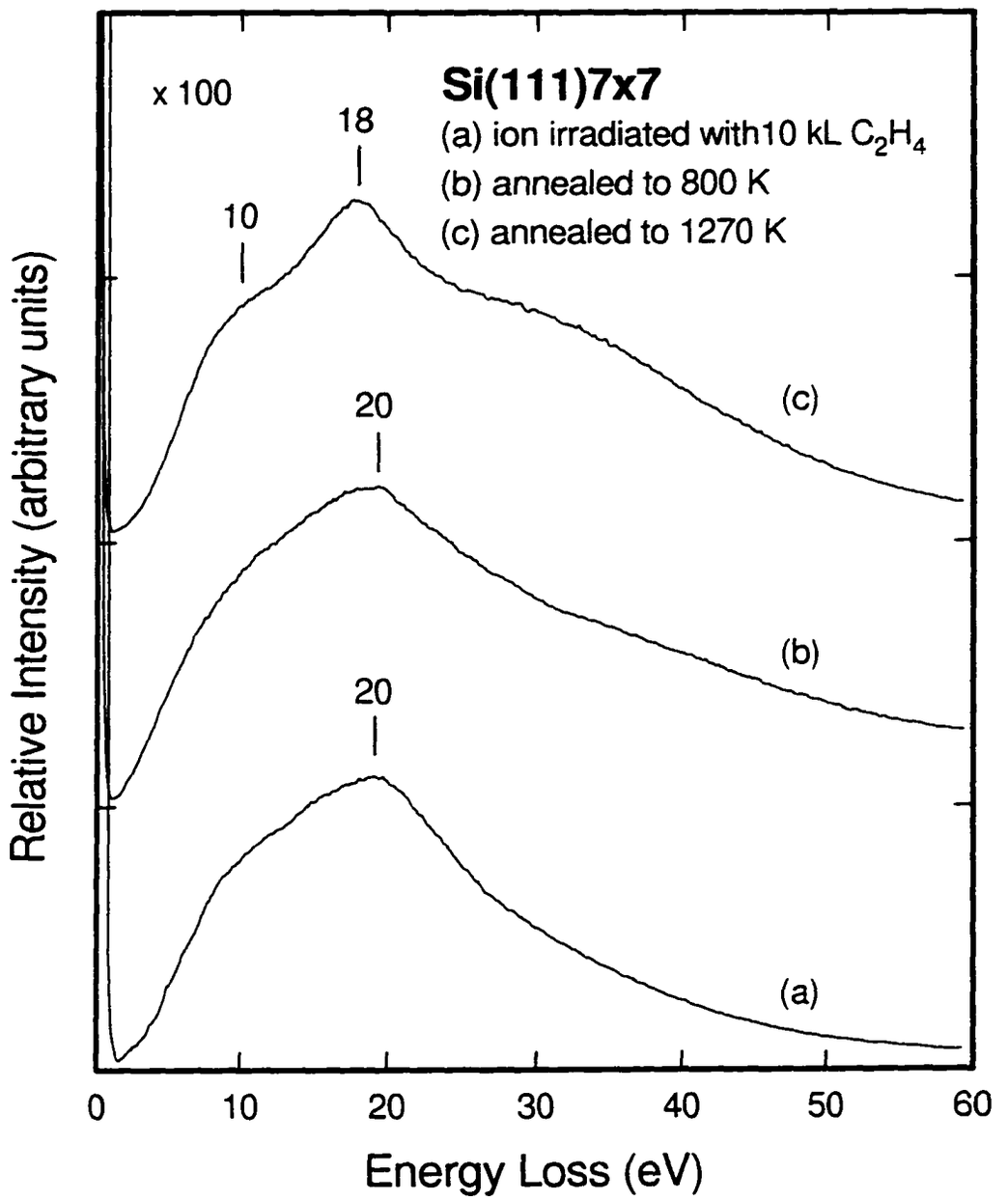

Figure 7.8 Electronic electron energy loss spectra for Si(111)7×7 (a) with ion-irradiated in 10 kL ethylene at 50 eV impact energy, followed by annealing to (b) 800 K, and (c) 1270 K.

Reproduced with permission of the copyright owner. Further reproduction prohibited without permission.

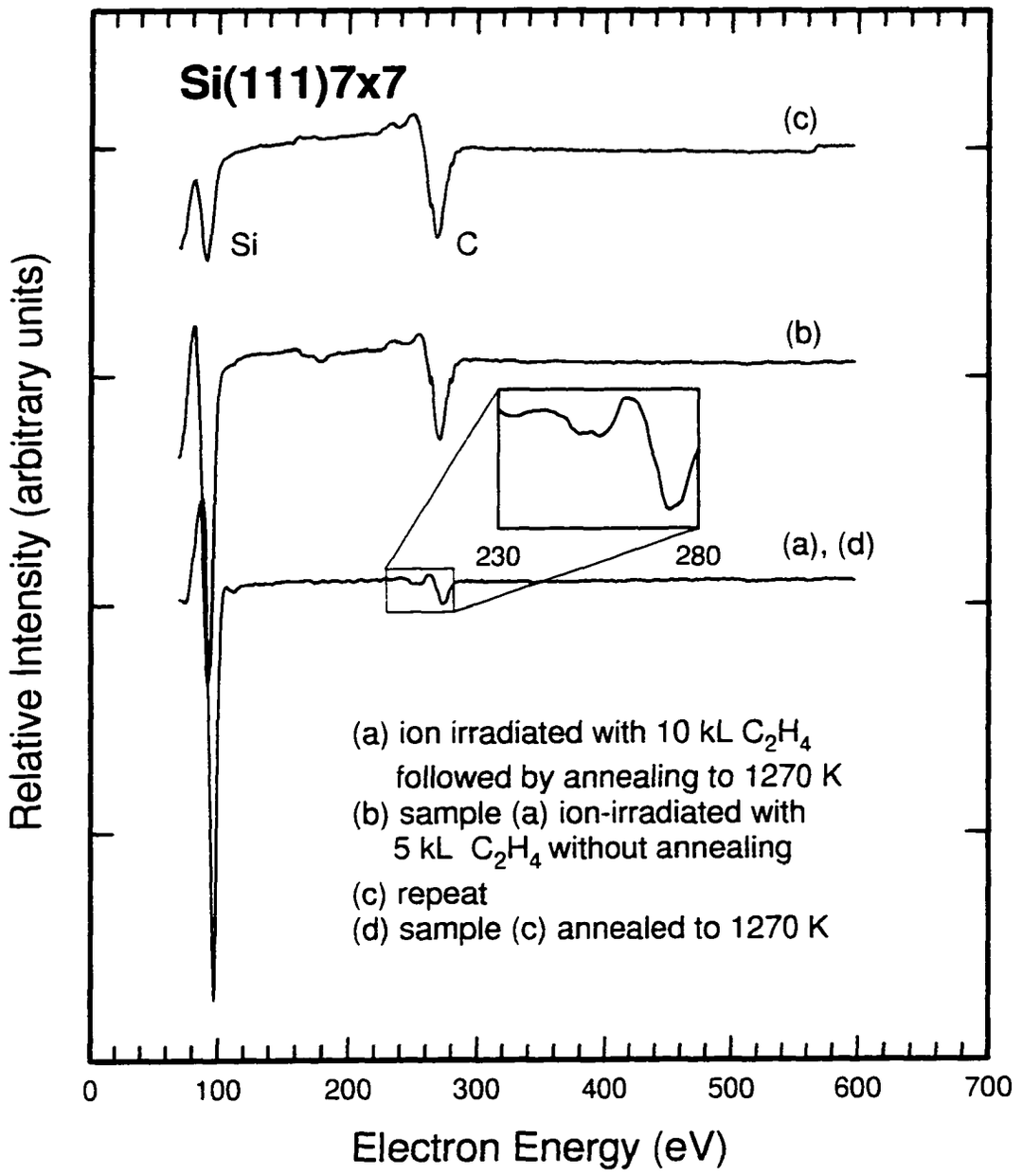

Figure 7.9 AES spectra for Si(111)7×7 (a) ion-irradiated in 10 kL ethylene at 50 eV impact energy and annealing to 1270 K, (b) followed by further ion irradiation with 5 kL, and with (c) additional 5 kL, and (d) sample (c) annealed to 1270 K.

Reproduced with permission of the copyright owner. Further reproduction prohibited without permission.

shown in Figure 7.9a, whereby carbon was clearly present on the surface along with a predominant signal due to Si. However, further sputtering without the anneal (Figure 7.9b-c) reduced the Si signal but enhanced the C signal substantially, which indicates that the relative carbon concentration continues to increase with increasing ethylene dosage. It is of interest to note that annealing the resulting sample shown in Figure 7.9c to 1270 K restored the previous sample condition shown in Figure 7.9a, which suggests that carbon did not remain at the top layer of the surface but diffused into the bulk. This diffusion process may provide an efficient way to produce a uniform SiC layer below the surface [13].

In the previous studies [21,22], the line shape of the carbon KLL Auger peak has been used to determine the bonding types of carbon (graphite sp^2, diamond sp^3, and SiC). Figure 7.10 shows the carbon KLL Auger spectra of graphite (sp^2), natural diamond (sp^3),

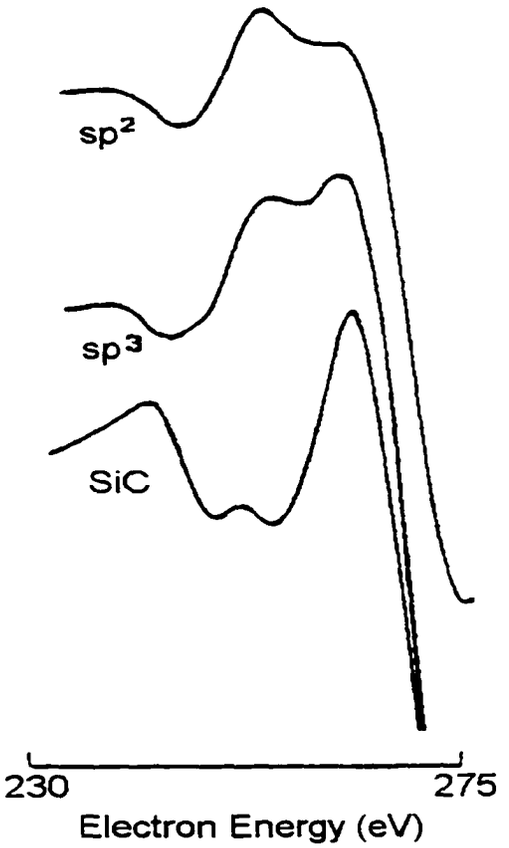

Figure 7.10 Typical carbon KLL Auger lines of graphite (sp^2), natural diamond (sp^3), and SiC (after Ref. 21).

Reproduced with permission of the copyright owner. Further reproduction prohibited without permission.

and SiC, reported in Ref. 21. In our spectrum (insert of Figure 7.9a-d), the line shape of the carbon KLL peak clearly supports the existence of SiC.

Although the diffusion of carbon into the bulk has been observed by using thermal and ion-assisted deposition methods, it has not been found to occur at very high dosage of ethylene ions. Figure 7.11 shows the ELS spectra of Si(111)7×7 ion-irradiated with 100 kL of ethylene at 50 eV IE at RT followed by annealing to different temperatures. In consideration of the typical energy positions of the plasmon peaks listed in Table 7.1, the broad shoulder at ~6.6 eV in Figure 7.11b corresponds to a surface carbon mixture of different bonding structures, which may include *a*-C, *a*-C:H, and graphite. The presence of the broad $\pi+\sigma$ plasmon peak at 25 eV suggests that the dominant species was graphite. Although the $\pi+\sigma$ plasmon for *a*-C:H also locates at 25 eV, it is unlikely that *a*-C:H could remain intact after annealing to 1270 K because hydrogen would desorb during the high temperature anneal. The sharpening of the π plasmon peak at 6.6 eV after annealing the sample to 800 K (Figure 7.11c) indicates hydrogen desorption from the surface and recombination of carbon atoms to form a graphite layer. Once the graphite was formed on the surface, however, further annealing the sample to a higher temperature (1270 K in Figure 7.11d) did not cause the carbon to undergo further diffusion into the bulk. A high exposure of ethylene ions at RT therefore appears to cause the formation of graphite, which in turn prevents the diffusion of carbon into the bulk, and hence the formation of SiC.

7.3 Summary

In this Chapter we investigated the initial processes involved in the formation of SiO_2 and SiC layers on Si(111)7×7 by using ELS, HREELS, and AES techniques. The formation of SiO_2 layer can be achieved by annealing the silicon sample in O_2 at 700 K, and is characterized by its electronic transitions near 5 and 7 eV. We also show that the formation of SiO_2 can also be obtained by ion irradiation in oxygen at RT. For the formation of a carbon layer, we verify that the formation of the so-called Si-C alloy on the surface can be achieved by annealing Si(111)7×7 in ethylene at 800 K while the diffusion of carbon atoms into the bulk occurs at a higher temperature (1270 K). Furthermore, we demonstrated that a higher efficiency in producing the carbon layer can be obtained by using ion-assisted

Reproduced with permission of the copyright owner. Further reproduction prohibited without permission.

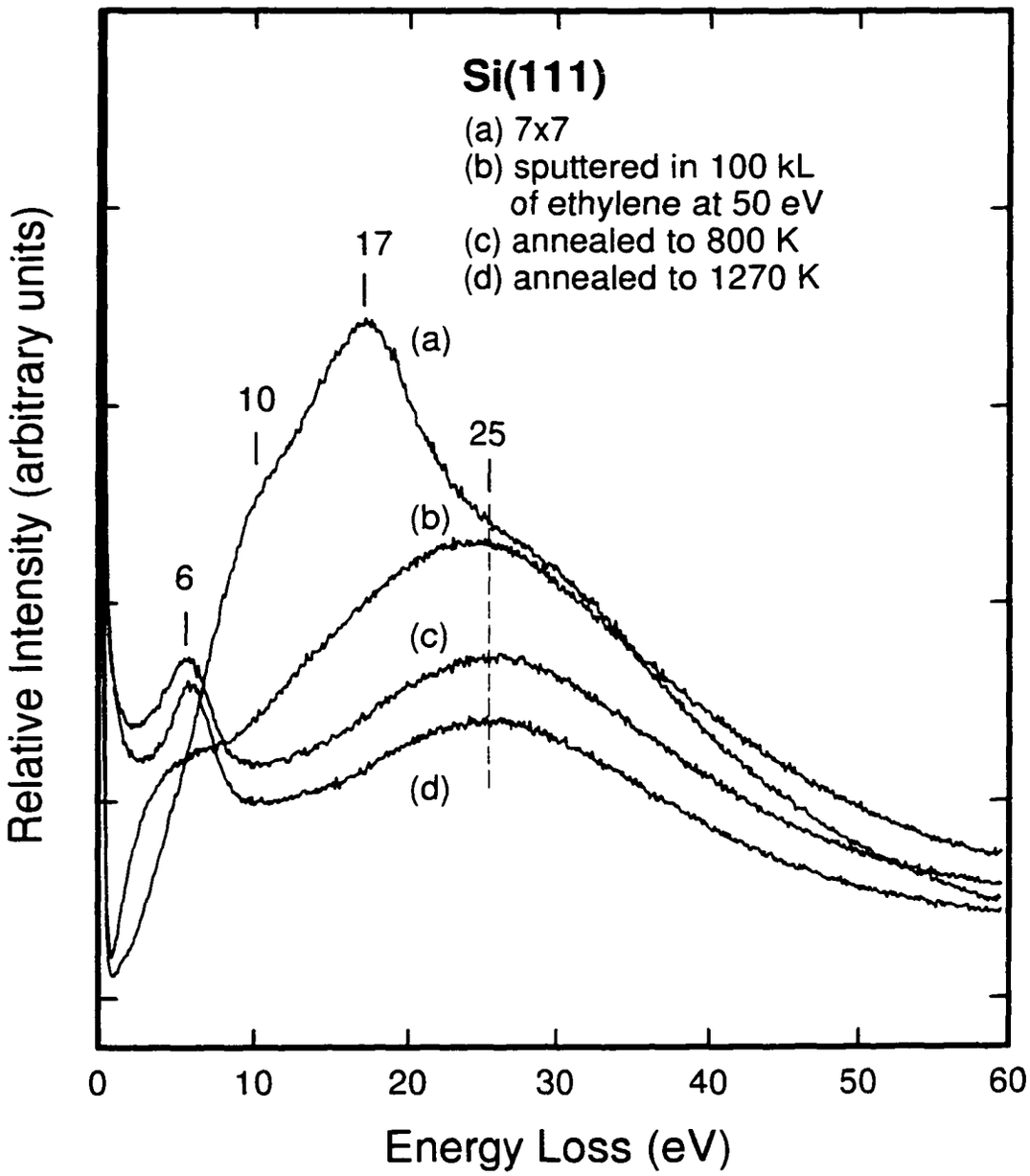

Figure 7.11 Electronic electron energy loss spectra for (a) clean Si(111)7×7, (b) sputtered in 100 kL of ethylene at 50 eV impact energy, followed by annealing to (c) 800 K and (d) 1270 K.

Reproduced with permission of the copyright owner. Further reproduction prohibited without permission.

deposition than thermal deposition. A very large dosage of ethylene ions (100 kL) at RT was found to cause the formation of a graphite layer, which prevented the diffusion of carbon into the bulk and hence the formation of the SiC layer.

In future studies, it would be of interest to further explore more efficient means of producing a uniform and better defined SiC layer. In order to determine the composition underneath the top surface layer, ELS experiments employing a higher incident energy are required to provide further insights into the mechanism of SiC layer formation. In addition, diluting hydrocarbons with a high proportion of hydrogen (99%) as the reactant gas has been proven to be a critical condition in producing diamond or diamond-like carbon films [23]. It would therefore also be of practical interest to investigate the formation processes of these films by using the electron energy loss techniques.

7.4 References

[1] G. Hollinger and F. J. Himpsel, Phys. Rev. B **28**, 3651 (1983).

[2] G. Comtet, L. Hellner, G. Dujardin, and M. J. Ramage, Surf., Sci. **352-354**, 315 (1996).

[3] R. Martel, Ph. Avouris, and I. W. Lyo, Science, **272**, 385 (1996).

[4] H. Ibach, N. D. Bruchmann and H. Wagner, Appl. Phys. A **29**, 113 (1982).

[5] M. Green, A. Liberman, J. Phys. Chem. Solids **23**, 1407 (1962).

[6] G. Hollinger, Y. Jugnet, and T. M. Duc, Solid State Commun. **22**, 277 (1977).

[7] H. Ibach and J. E. Rowe, Phys. Rev. B **9**, 1951 (1974).

[8] P. Kovarik, E. B. D. Bourdon, and R. H. Prince, Phys. Rev. B **48**, 12123 (1993).

[9] J. C. Augus, Thin Solid Films, **216**, 126 (1992).

[10] M. Ohring, "The Materials Science of Thin Films", Academic, Toronto (1992).

[11] "Electron Spectroscopy for Surface Analysis", H. Ibach (ed.), Springer, New York (1977).

[12] M. P. Seah, and W. A. Dench, Surf. Interface Anal. **1**, 2 (1979).

[13] F. Bozso and J. T. Yates, Jr., W. J. Choyke and L. Muehlhoof, J. Appl. Phys. **57**, 2771 (1985).

[14] H. Froitzheim, I. Ibach, and D. L. Mills, Phys. Rev. B **11**, 4980 (1975).

Reproduced with permission of the copyright owner. Further reproduction prohibited without permission.

[15] M. Tabe, T. T. Chiang, I. Lindau, and W. E. Spicer, Phys. Rev. B **34**, 2706 (1986).

[16] E. A. Taft and H. R. Phillip, Phys. Rev. A **138**, 197 (1965).

[17] Y. Ohno, Phys. Rev. B **39**, 8209 (1988).

[18] P. A. Taylor, M. Bozack, W. J. Choyke, and J. T. Yates, Jr., J. Appl. Phys. **65**, 1099 (1989).

[19] J. Yoshinobu, H. Tsuda, M. Onchi and M. Nishijinma, Solid State Commun. **60**, 801 (1986).

[20] H. Froitzheim, U. Kohler and H. Lammering, Surf. Sci. **149** 537 (1985).

[21] A. K. Green and V. Rehn, J. Vac. Sci. Technol. A **1**, 1877 (1983).

[22] Y. W. Ko and S. I. Kim, J. Vac. Sci. Technol. A **15**, 2750 (1997).

[23] J. C. Augus, Thin Solid Films **216**, 126 (1992).

Reproduced with permission of the copyright owner. Further reproduction prohibited without permission.

Chapter 8
OUTLOOK

The present work investigates the surface processes induced by low-energy electron and reactive ions on two "classic" surfaces in surface science: Cu(100) and Si(111)7×7 by using a custom-built multi-technique EELS spectrometer and other surface analysis techniques – AES, LEED, and TPD. We demonstrated the extraordinary properties of reactive ions for introducing new surface reactions and for enhancing adsorption that are different from the normal gas-surface reactions on both the unreactive Cu(100) and the relatively reactive Si(111)7×7 surfaces. In particular, new surface processes were observed on Cu(100), which include "stabilized" CO adsorption at and above RT, the co-existence of embedded nitrogen and surface-bonded nitrogen, and the adsorption of hydrocarbon species generated by low energy ion irradiation above RT. As a generic "unreactive" metal surface, Cu(100) is inert to CO, N_2, and C_2H_4 at RT. It is the reactive ions produced during ion irradiation that gave rise to these unique surface products. Although ion irradiation can also introduce other effects such as the creation of defect sites and sputtering on the surface, we showed that the observed surface reactions were not caused by defect sites but rather by reactive radicals produced during the ion irradiation process. The simple Cu(100) surface has therefore proven to be a useful model surface for investigating the complicated ion-induced surface reactions involving non-directional surface chemical bonds.

On Si(111)7×7, we investigated the effects of common surface contaminants (including ambient gas and carbon) on the adsorption of oxygen and water. We showed that HREELS is a surface-sensitive technique that could reveal even a minute amount of carbon or water contamination, which was not found to have any major effect on the surface reactivity to oxygen. However, a higher level of carbon contamination was found to poison the surface and to prevent the adsorption of water and hydrocarbons but not oxygen. Because contamination on a semiconductor surface is a common problem in the electronics industry, more quantitative studies extending the present work to other chemicals (such as the common plasma etchants and solvents, etc.) will be therefore of

Reproduced with permission of the copyright owner. Further reproduction prohibited without permission.

practical interest to controlling the initial deposition process in device fabrication. In addition, the formation of SiO_2 and SiC layers on Si(111)7×7 prepared by using both thermal and ion-assisted deposition methods was also studied and the as-formed layers were characterized by their HREELS, ELS and AES spectra. We showed that the use of ion-assisted reactions has the potential to produce these films at a lower temperature and with a higher efficiency. More detailed studies, involving ion-assisted deposition at different temperatures and ion impact energies and the use of different reactant gases for the deposition, will provide better understanding of the deposition mechanisms in ion-assisted film growth. Because the formation of other carbonaceous films, such as diamond-like carbon and diamond thin films, remains to be a technologically important subject, future investigation of the initial formation of these films will also be of practical interest.

In our present experimental setup, the ions produced by the ion gun were not mass-selected and the ion flux could only be crudely estimated by monitoring the total current on the sample, which in turn depended on the ion impact energy and the focusing conditions of the ion gun. These limitations prevented us from more quantitative studies of the ion-induced effects. A more sophisticated ion gun with a (quadrupole) mass selector will be very useful for better defining the composition of the incident ion beam. Furthermore, because the exposure of reactant gases was achieved by ambient dosing, which involved back-filling the UHV chamber with the gas of interest by means of a variable leak valve, a low dosing pressure (i.e., not exceeding ~4×10^{-5} Torr) was often used in order to achieve a quick vacuum recovery. This reaction pressure is far too low compared to that used for CVD-type reactions, which is usually at least several Torrs to one atmosphere. To solve this problem, a separate reaction chamber is required in order to properly simulate a typical CVD reaction. Moreover, the composition of reactant gases and their flow rates are important parameters for controlling the final products. An improved gas introduction system will therefore be important to achieve a better control.

In the present work, we demonstrate the capabilities of our home-built multi-technique EELS spectrometer for both HREELS and extended-range ELS experiments. An energy resolution of 10 meV FWHM in the HREELS mode and 30 meV FWHM in

Reproduced with permission of the copyright owner. Further reproduction prohibited without permission.

the ELS mode can now be routinely achieved. This performance is generally sufficient for most applications. However, the count rates, at 100 kC/s for HREELS and 300 kC/s for ELS experiments for the elastic peak, should be improved to shorten the nominal data acquisition time from the present 10 to 100 minutes required to obtain a spectrum with decent statistics. The long scanning time not only affects the productivity of the experiment, but also limits its applications to study more reactive adsorbates and surfaces [such as Si(100)]. A higher counting efficiency also would facilitate better quality angle-resolved experiments, which offer more information on the bonding geometry of adsorbates. A brighter electron source should be developed to improve the scattering efficiency of the spectrometer without sacrificing the energy resolution. In the ELS experiment, the calibration of the transmission function of the analyser over a wide energy range still was a problem. Although some workarounds have been suggested in Chapter 2, a better calibration method must be developed. In addition, the present scanning range of the spectrometer in ELS mode is limited by the existing power supply to 100 eV, preventing it from use in the applications that probe the electronic structure of the sub-surface layer. This problem can be easily alleviated by modifying the power supply, because the electron optics of the analyzer itself was designed to accommodate a lens retardation ratio as large as 1:1000. Although the ELS spectra in the second-derivative mode can provide better sensitivity to small changes in ELS features, the normal (non-derivative) mode ELS can provide spectra with more meaningful relative intensity. With the above improvements, better quality experimental results can be obtained in a shorter acquisition time than with the present spectrometer.

Reproduced with permission of the copyright owner. Further reproduction prohibited without permission.